A Deeper Understanding of Material Properties Through Computational Model Development.

A Deeper Understanding of Material Properties Through Computational Model Development.

by

Gil M. Repa

Presented to the Graduate and Research Committee

of Lehigh University

in Candidacy for the Degree of

Doctor of Philosophy

in

Chemistry

Lehigh University

May 2024

Dissertation is accepted and approved in partial fulfillment of the requirements for the degree of Doctor of Philosophy in Chemistry.

Gil M. Repa

Date Approved:

_____
Date

List of Committee Members:

_____
(Lisa A. Fredin)

_____
Elizabeth R. Young

_____
Greg Ferguson

_____
Srinivas Rangarajan

Acknowledgements

I cannot begin to express my gratitude to those who have helped me these past five years. Among those I am deeply indebted to are: my grandparents, Dr. George S. Smith and Kathleen Smith, who have graciously provided me with housing, support, and ice cream sandwiches; my mother, Kathleen Repa, who always had my back and whose contributions to my life are beyond what can be captured in a brief acknowledgements section; my father, Dean Repa, who provided consistent support throughout my educational career; my brother, Lee Repa, who provided many hours of therapeutic Mario Kart; my partner, Giavonna Picknally, whose visits were the best remedy to long weeks in the office; and Slater, Kimba, Flynne, Phantom, Dusty, and Galaxy. I would also like to extend my sincere thanks to those that I have come to know during my time here at Lehigh. Specifically: my co-worker, Zachary Knepp, who has been the best friend I could have shared this experience with; his wife, Kayla, for her contributions to the office foliage; my advisor, Lisa Fredin, whose support and belief in my work has kept me motivated to finish this degree; and the members of the Lehigh Photochemistry group for their constant feedback and support. It is these people who not only enabled me to complete this thesis, but who have also made my time at Lehigh enjoyable and memorable.

Contents

List of Tables

List of Figures

Abstract

The pace of materials development can be significantly increased by computational models that accurately capture the characteristics of experimental materials. While advances in computational architecture have enabled researchers to calculate the properties of pure materials with high fidelity, it is often disorder of the perfect crystal that gives rise to technologically relevant properties. This thesis aims to contribute a robust modeling framework for disordered materials by developing improved criteria to access metal oxide point defects, interfaces, and nanoparticles using theories that are efficient and easily generalizable. Insights into technologically relevant materials are developed, including discovery and assignment of spectroscopic signals to new defect geometries in doped $SrTiO_3$, identification of ring-like atomic motifs in amorphous Al_2O_3 responsible for experimentally observed electronic properties, and combination molecular dynamics and density functional theory approaches to produce more realistic amorphous TiO_2 nanoparticles and interfaces.

Part I

Introduction

Chapter 1

Background

Disorder represents one of the most critical determinants of materials properties. The term disorder refers to any atomic structural feature that increases the configurational entropy of a material relative to an unperturbed stoichiometric crystalline reference. These deviations from perfect periodic order include point defects or dopants, interfaces, and nanostructuring. Because all crystals are finite, all materials necessarily contain disorder. Furthermore, some amount of impurities are inherent in even the purest material samples. Whether intentionally created or not, the role of disorder in device performance has been probed for a wide range of applications stretching from the next generation of energy and catalytic materials in a climate-challenged society to the very quantum computers that such materials may one day be designed on.

Historically, the study of disorder has largely been phenomenological in nature, due in part to the large experimental difficulty in characterizing such systems. For example, the PN junction was discovered in 1941 [1], but a fundamental understanding of p- and n-type dopants was not provided until 1949 [2]. Despite advances in computational infrastructure and refinement of quantum theory to enable widespread calculations, a comprehensive understanding of how disorder gives rise to observed material properties often eludes researchers. Whether the goal is to modify the elastic, electric, or magnetic properties of a material, developing realistic and predictive computational models for such disordered systems means tackling the perfect storm

of large systems governed by complex quantum mechanical effects that lack experimental data against which to validate.

Of the two main computational approaches to studying matter, neither one is particularly well-suited for studying all aspects of disorder when taken individually. The primary method for calculating the electronic structure of materials, density functional theory (DFT, discussed further in section 2.1), is limited to calculations with approximately 1000 atoms even under the most aggressive approximations [3]. This is far below the number of atoms that is typically needed to define a disordered structure. Furthermore, many experimentally-relevant materials require even more accurate DFT methods to achieve a reasonable electronic structure description. Consequently, materials researchers are commonly faced with the decision whether to approximate electronic properties or structure.

In those instances where obtaining a structural model of disorder is most desired, classical molecular dynamics techniques (MD, discussed further in section 2.2) provide an alternative to access length and time scales that are too computationally expensive for DFT, including those surpassing thousands of atoms. Instead of relying on quantum mechanics to move atoms, MD propagates atom positions in time according to Newtonian mechanics parameterized by a pre-defined force field. While such an approach loses all electronic structure information, small MD-generated structures may be subjected to subsequent calculation with DFT to recover electronic structure insight in some cases. This combination workflow is discussed in section 2.2.1 and relied on heavily in Part III of this thesis for generating amorphous structures.

Overall, this thesis develops criteria to generate more realistic computational models of point defects, amorphicity, and nanostructuring in materials. Particular attention is paid to the archetypical oxides $SrTiO_3$ and TiO_2. These and related materials have formed the backbone of many of today's electronic devices. Focusing on such commonly used materials ensures that the approaches and results developed here are easily generizable to all related systems, obviating the need for system-specific considerations or semi-empirical corrections that largely prevent the use of DFT as a predictive tool for disordered systems. Additionally, fundamental insights

into the chemical physics of materials in a range of electronic, energy harvesting, and catalytic processes are provided.

This thesis is organized as follows: Chapter 2 reviews basic considerations for computational materials modeling and briefly introduces many of the points which are discussed in the following chapters. The remaining chapters are then divided into two additional parts. Part II (Chapters 3, 4, 5) presents results concerning doped $SrTiO_3$. The influence of model choice on predicted defect geometries and subsequent elimination of these geometries by comparison to experimental data is discussed. Part III is a triology concerning amorphous materials of decreasing dimensionality. Specifically, MD structure generation and subsequent electronic structure insights into bulk Al_2O_3 (Chapter 6), amorphous TiO_2 surfaces (Chapter 7), and amorphous TiO_2 nanoparticles (Chapter 8) are discussed.

Chapter 2

Computational Modeling of Materials

2.1 Density Functional Theory

The fundamental processes that underlie the functionality of devices in applications like photovoltaics, transistors, light-emitting diodes, photosynthesis, water-splitting, catalysis, and batteries can be understood in terms of fundamental excitation, oxidation, reduction, energy transfer, or charge carrier transport. Quantum chemistry provides an avenue to understand these processes in terms of geometric and electronic changes in a system. Density functional theory remains the workhorse for such quantum chemical calculations because it is computationally affordable enough to enable calculation of interesting systems, yet provides significant insights into the structural and electronic properties of materials.

The computational advantages of DFT largely arise from bypassing the N-electron wavefunction ψ that forms the basis of alternate so-called wavefunction methods. Instead, DFT utilizes the density of the system. Among the benefits obtained by exchanging the fundamental variable ψ for density n ($n = \psi^2$), gains in computational efficiency enable DFT to be used for large systems with hundreds of atoms, providing insight many technologically relevant systems today, including metal-centered complexes, nanoparticles, and materials.

The foundation of this approach was established by two Hohenberg-Kohn-Sham theorems. The first of which, termed the existence theorem [4], essentially provides assurance that the

Hamiltonian can be determined by the ground-state density when an external potential (i.e., atom coordinates and charges) is defined. The second Kohn-Sham theorem [5] provides a variational theorem to optimize n, similar to those that have been developed for wavefunction methods, that allows DFT calculations to be performed self-consistently [6].

The computational advantages of DFT are largely conferred by its fundamental approximation. Specifically, a system of N interacting electrons in DFT is represented by a fictitious system of N non-interacting electrons with overall ground-state density identical to the real system. The energy for such a system can be broken into components as

$$E[n(\mathbf{r})] = T_{ni}[n(\mathbf{r})] + V_{ne}[n(\mathbf{r})] + V_{ee}[n(\mathbf{r})] + \Delta T[n(\mathbf{r})] + \Delta V_{ee}[n(\mathbf{r})] \tag{2.1}$$

where the terms refer to the kinetic energy of the non-interacting electrons, the nuclear-electron interaction, the classical electron-electron repulsion, the correction to the kinetic energy deriving from the interacting nature of the electrons, and all non-classical corrections to the electron-electron repulsion energy, respectively. For the interacting system, $V_{ne}[n(\mathbf{r})]$ and $V_{ee}[n(\mathbf{r})]$ can be approximated classically by

$$V_{ne}[n(\mathbf{r})] = \sum_{k}^{nuclei} \int \frac{Z_k}{|\mathbf{r} - \mathbf{r}_k|} n(\mathbf{r}) d\mathbf{r} \tag{2.2}$$

and

$$V_{ee}[n(\mathbf{r})] = \frac{1}{2} \iint \frac{n(\mathbf{r}_1) n(\mathbf{r}_2)}{|\mathbf{r}_1 - \mathbf{r}_2|} d\mathbf{r}_1 d\mathbf{r}_2, \tag{2.3}$$

where Z is the atomic number of the nuclei, and $\mathbf{r}_1$ and $\mathbf{r}_2$ are integration variables running

over all space. With this approximation, eq. 2.1 for a non-interacting system can be written as

$$E[n(\mathbf{r})] = \sum_{i}^{N}(\langle\chi_i| - \frac{1}{2}\nabla_i^2|\chi_i\rangle - \langle\chi_i|\sum_{k}^{nuclei}\frac{Z_k}{|\mathbf{r}_i - \mathbf{r}_k|}|\chi_i\rangle) + \sum_{i}^{N}\langle\chi_i|\frac{1}{2}\int\frac{n(\mathbf{r}')}{|\mathbf{r}_i - \mathbf{r}'|}d\mathbf{r}'|\chi_i\rangle + E_{xc}[n(\mathbf{r})], \tag{2.4}$$

where the errors introduced by substitution of eqs. 2.2 and 2.3 are lumped into the so-called exchange-correlation term E_{xc}. The orbitals χ that minimize E in eq. 2.4 yield the Kohn-Sham equation

$$h_i^{ks}\chi_i = \epsilon_i\chi_i, \tag{2.5}$$

where the Kohn-Sham one-electron operator is defined as

$$h_i^{ks} = -\frac{1}{2}\nabla_i^2 - \sum_{k}^{nuclei}\frac{Z_k}{|\mathbf{r}_i - \mathbf{r}_k|} + \int\frac{n(\mathbf{r}')}{|\mathbf{r}_i - \mathbf{r}'|}d\mathbf{r}' + V_{xc}, \tag{2.6}$$

and the functional derivative

$$V_{xc} = \frac{\delta E_{xc}}{\delta n}. \tag{2.7}$$

Determination of the Kohn-Sham orbitals can be undertaken using the same approach of Hartree-Fock [6]. Specifically, they can be expressed within a set of basis functions $\{\phi\}$ and orbital coefficients determined by

$$k_\mu\nu = \langle\phi_\mu| - \frac{1}{2}\nabla^2 - \sum_{k}^{nuclei}\frac{Z_k}{|\mathbf{r} - \mathbf{r}_k|} + \int\frac{n(\mathbf{r'})}{|\mathbf{r} - \mathbf{r}'|}d\mathbf{r}' + V_{xc}|\phi_\nu\rangle. \tag{2.8}$$

To this point, DFT has been derived as an exact formalism provided that a functional form is known for E_{xc}. However, it remains unknown, and determining functionals that are improved

approximations have become a major area of interest for improving DFT. For most electronic structure insights in this thesis, results are derived from the hybrid HSE06 [7] functional which represents the highest quality functional in planewave DFT for material systems of this size and type.

2.1.1 Representation of Materials

Since the very first implementations of DFT, there have been two fundamental ways to represent matter. The first approach is as a discrete cluster with a finite number of atoms and each atomic position exactly specified. The second representation is as a unit cell which is then repeated by space group operations to create an infinite lattice. While there has been some success in using cluster models to represent extended solids, it is more suited for finite structures like molecules or nanoparticles, and thus material calculations have become dominated by the periodic supercell approach. An important consideration for the periodic approach in disordered systems is to select a supercell that is large enough to prevent artificial interactions among periodic defect images and contain the entire dopant wavefunction. While this problem is well-known [8], computational expense prohibits calculations on supercells with more than approximately 1000 atoms even for basic local density approximation (LDA) [6] approaches, which is far below typical experimental dopant loading levels [3]. Unless computational infrastructure increases to the point where large experimentally sized unit cells can be directly calculated, the influence of the periodic boundary conditions must be considered. These considerations are discussed further in Chapter 3.

2.1.2 Optimizing Atom Positions

The standard approach for obtaining structural models of disorder is introduce small amounts of targeted disorder to an idealized crystalline starting structure. For example, a dopant atom can be inserted or a desired lattice plane cut from the structure. The atom positions can then be optimized around the inserted disorder by using traditional steepest descent optimization

techniques [3]. The primary issue for such approaches is that these materials have many local minima due to the large number of atoms and high configurational entropy. Furthermore, starting from a fairly low energy bulk geometry with only slight defects does not provide large force on the atoms early in the optimization. Therefore, a common pitfall is optimizing to a local rather than global minimum. In a case of eight crystallographically distinct materials with different point defects, it has been shown that traditional geometry optimization predicts incomplete minimization of defect structures in all cases [9]. Alternative approaches that utilize an evolutionary algorithm to find low energy defect configurations [10] are appealing for in-depth studies of single defects, but because of their computational cost and poor generalizability, have not become a standard approach.

One possible way to mitigate the issues of incomplete optimization is to introduce random displacements of each atom in the unit cell prior to traditional geometry optimization. These "rattled" structures allow the optimizer to escape local minima and relax to a lower energy ground state structure. Such symmetry breaking has been shown to improve the optimization behavior of TiO_2 nanoparticles and is discussed in detail in Chapter 8.

2.1.3 Comparing to Experiment

One of the major appeals of computational materials chemistry is deconvolution of experimental spectra. Fortunately, much of the theory for translating between Kohn-Sham calculated densities and experimental observables has already been developed [3]. Therefore, progress is governed almost universally by the ability of a chosen basis set and functional to accurately capture the properties of the real material. Indeed, recent exemplary insights into experimental data by comparison to DFT are far too numerous to a capture in this brief introduction. However, scanning tunnelling microscopy and spectroscopy [11–13], vibrational properties [14], electron paramagnetic and nuclear magnetic resonance [15], Mössbauer spectroscopy [16, 17], and transport and optical properties [18] are amenable to comparison with experiment. Relevant to disorder, a comparison of DFT to experimental electron paramagnetic resonance spectra

is presented in Chapter 4.

2.2 Classical Molecular Dynamics

In cases where the time and length scales exceed that accessible to DFT, a surprisingly robust approximation to matter is to treat individual atoms as point charges. The interaction between these point charges can be described using a classical interaction known as a force field. In such a setup, the equations governing position x and velocity v for an atom with mass m can be derived from Newton's second law as

$$\frac{dx}{dt} = v \quad \text{and} \quad \frac{dv}{dt} = \frac{F(x)}{m}. \tag{2.9}$$

The system can be propagated in time through solution of the system of ordinary differential equations via

$$v_{i+1} = v_i + \delta_t F(x_i)/m \quad \text{and} \quad x_{i+1} = x_i + \delta_t v_i, \tag{2.10}$$

where δ_t is the time step. In practice, alternative integrators, such as the velocity Verlet algorithm, are more commonly used.

In MD simulations, the macroscopic thermodynamic properties of a system are derived from atom position and velocities via statistical ensembles. This concept is important for understanding the physicality of MD derived results, especially those in Part III of this thesis. The most basic is the microcanonical ensemble, which is often denoted NVE to indicate that the ensemble is comprised of a series of atomic configurations categorized by constant moles (N), volume (V), and energy (E). This simulation set up corresponds to a system in complete isolation that cannot exchange heat or matter with an outside environment. The other two most commonly encountered ensembles are the canonical (NVT) and isothermal-isobaric (NPT). The former corresponds to a system that is in contact with a heat bath to maintain constant

temperature. In practice, temperature in MD simulations is controlled by scaling the velocity of particles to achieve a velocity distribution consistent with a given temperature. The NPT ensemble is indeed the most physical of the three discussed here as it corresponds to a system that is in contact with a heat bath and also allowed to change volume to maintain constant pressure. These conditions represent most laboratory conditions.

One particular challenge when using the NPT ensemble in the context of the current work relates to the size of the systems considered here. Because such structures must be amenable to subsequent DFT calculation without modification, small system sizes must be considered. These small systems sizes typically suffer from large fluctuations of thermodynamic state variables during the MD simulation, which frequently lead to numerical instabilites or unphysical simulations. Therefore, greater care than normal must be taken when thermostatting or barostatting simulation cells similar to those presented in subsequent chapters.

2.2.1 Generating Atomistic Models

For cases where a targeted structure is far on the potential energy surface from a guess structure, the steepest descent optimizer described in section 2.1.2 may not be appropriate for obtaining the desired geometric result. For example, a disordered amorphous material may be far from the most thermodynamically favorable structure and will never optimize from a low-energy crystalline guess. Therefore, alternate methods are needed to generate amorphous surfaces and interfaces using MD techniques. The most widely used MD strategy involves starting from a crystalline structure that is then perturbed through repeated melting and quenching simulations. Specifically, the melting simulation introduces a high-energy disordered configuration which can be frozen in place during the quenching process. However, the structure obtained is highly dependent on the conditions of the quench. These parameters are examined in more detail in chapters 6 and 7.

Part II

Modeling Dopants and Disorder in Crystalline Materials

Chapter 3

Representation of point defects by supercells[†,‡]

3.1 Introduction

The perovskite $SrTiO_3$ receives significant scientific attention both as a candidate material for wide ranging applications in photocatalysis [19, 20], thermoelectric generation [21], and electronics [22], as well as a model system for understanding the fundamental structural and rich electronic properties of the wider perovskite family [23]. Whether intentional or not, $SrTiO_3$ in experiments is frequently used with defects which have the potential to significantly alter or improve measured properties. In addition to atomic vacancies, the introduction of foreign atoms into the native crystal lattice is a critical means to engineer functionality [24]. Interest in understanding the fundamental consequences of disorder in the perovskite lattice has sparked an explosion of experimental and first-principles studies [25–30].

The structure of $SrTiO_3$ lends itself well to computational study by the supercell method in periodic boundary density functional theory (DFT). The bulk form can be considered as a linked network of corner sharing TiO_6 octahedra forming a *ccp* array around higher coordination sites for Sr^{2+} cations. Two cubic unit cells can be written for this structure (Fig. S1[‡]) with one centered on Sr-sites coordinated ionically by 12 O^{2-} anions with corners of Ti atoms (A-cell), and one centered on Ti-sites, coordinated covalently by six O^{2-} anions with corners of Sr atoms (B-cell).

[†]Portions of this chapter have been published in Repa, G.M.; Fredin, L.A. Parameter space exploration reveals interesting Mn-doped $SrTiO_3$ structures. *Physical Chemistry Chemical Physics* **2021**, 23, 23486–23500.

[‡]Electronic supplementary information is available at https://doi.org/10.1039/D1CP02417E.

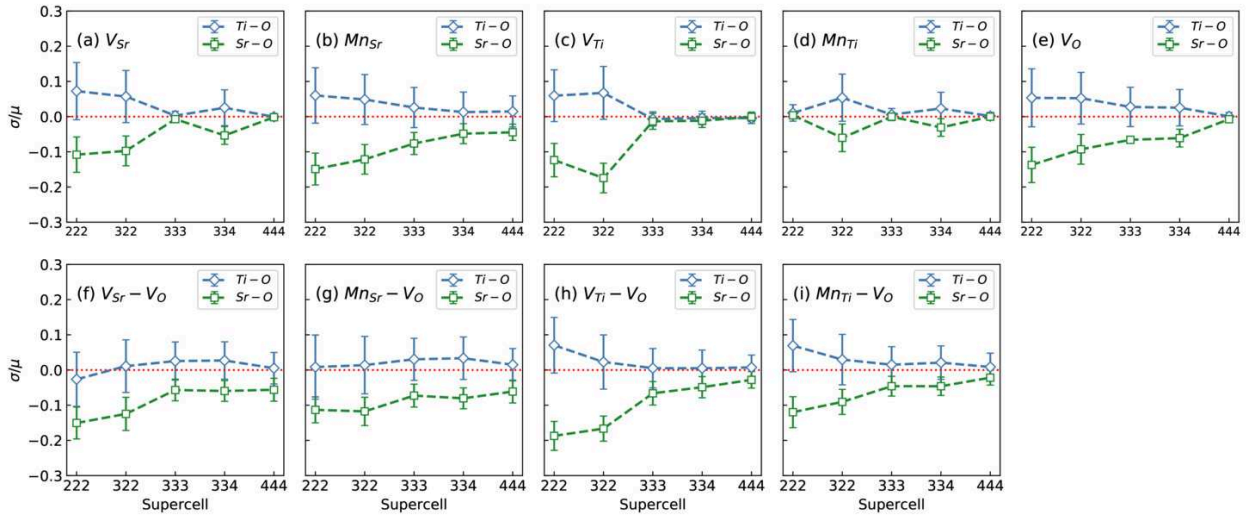

Figure 3.1: Deviation (σ) and variation (μ) of Ti—O (blue) and Sr—O (green) bond lengths from the pure crystal structure (red) for each unit cell and defect (a-i). A data point above the reference value should be interpreted as elongation of the average bond length, and is reported directly in Å. Error bars are reported with magnitude σ/μ to allow direct comparison of the magnitude of Sr—O and Ti—O variation. For asymmetric 3 x 2 x 2 and 3 x 3 x 4 supercells, only the x- oriented defect is plotted.

The former case is the intuitive building block for computational supercells. For example, a 2 x 2 x 2 $SrTiO_3$ supercell would imply two A-cells repeated along all three lattice vectors. Despite its relatively simple bulk structure, understanding the complex chemistry of disorder in $SrTiO_3$ continues to present a significant challenge to theoreticians. For example, oxygen vacancies (V_O) in nonstoichiometric $SrTiO_3$ have been associated with a shift in conductivity [31], blue-green light emission [32], and an antiferrodistortive phase transition [33] of the $SrTiO_3$ lattice, yet studies to probe the nature of these behaviors produce contradictory results.

It is well documented that in the case of the V_O, there is extreme sensitivity to supercell size that has confounded attempts to explain the origins of its unique properties. In 2004, Buban and coworkers [34] showed that a 40 atom 2 x 2 x 2 supercell predicted a deep defect state, while larger supercells through the 160 atom 2 x 2 x 4 and 320 atom 4 x 4 x 4 predicted a shallow defect state with primarily t_{2g} character. Similar results were observed with GGA + U methods, where occupied intra-bandgap defect states were observed until blue shifted above the conduction band minimum in even larger 625 and 1080 atom supercells [33]. Such dependence

on supercell size was recently confirmed with the extended Hubbard DFT + U + V approach of Ricca et al. [25], and persists even with the use of hybridized functionals HSE06 [35, 36] and B3PW [37]. Although the dependence on supercell size is well established in this case, the type of defect-defect interactions contributing calculation artifacts, whether quantum mechanical, electrostatic, elastic, or magnetic in nature is often near-impossible to resolve [3].

Despite comparable importance, the same systematic rigor probing the relation between supercell size and V_O defect chemistry is critically lacking for other defect types, including vacancies of Sr and Ti atoms (V_{Sr} and V_{Ti} respectively). Metal vacancies in $SrTiO_3$ are important for controlling both the mechanical and electronic properties of the material, such as grain boundary structure [38] and ionic conductivity [39]. Using 3 x 3 x 3 supercells and a finite size correction scheme, Baker et al. [40] showed that V_{Sr} is the majority defect in $SrTiO_3$, with a much higher formation energy for B-site defects [40]. However, V_{Ti} has been experimentally observed in bulk $SrTiO_3$ by positron annihilation spectroscopy [41, 42]. In addition to these two defects, a comprehensive model of realistic $SrTiO_3$ would need to consider two Schottky vacancies, specifically adjacent V_O and metal vacancies (V_{Sr}–V_O, V_{Ti}–V_O), both of which have important implications in applications involving ionic conductivity [39], and for the formation of dopant complexes [43, 44].

With regard to supercell size, the situation is further confounded when considering $SrTiO_3$ structures doped with non-native elements, such as Mn^{4+}. These dopants not only produce potentially more complicated defect geometries requiring reorganization of a larger number of atoms, but also have the possibility of magnetic interactions among periodic defect images further introducing artifacts into the calculation. The Mn dopant is of special interest because it is intermediate in size between the Sr and Ti, and its variable oxidation states allow it to substitute for both Sr and Ti atoms (Mn_{Sr} and Mn_{Ti} respectively) [45, 46]. Properties can be further tuned by controlling oxygen concentration and forming the analogous double defects (Mn_{Sr}–V_O, Mn_{Ti}–V_O) [47, 48]. Like metal vacancies, doped supercells require careful investigation to understand results that are simply an artifact of model choice and which provide much

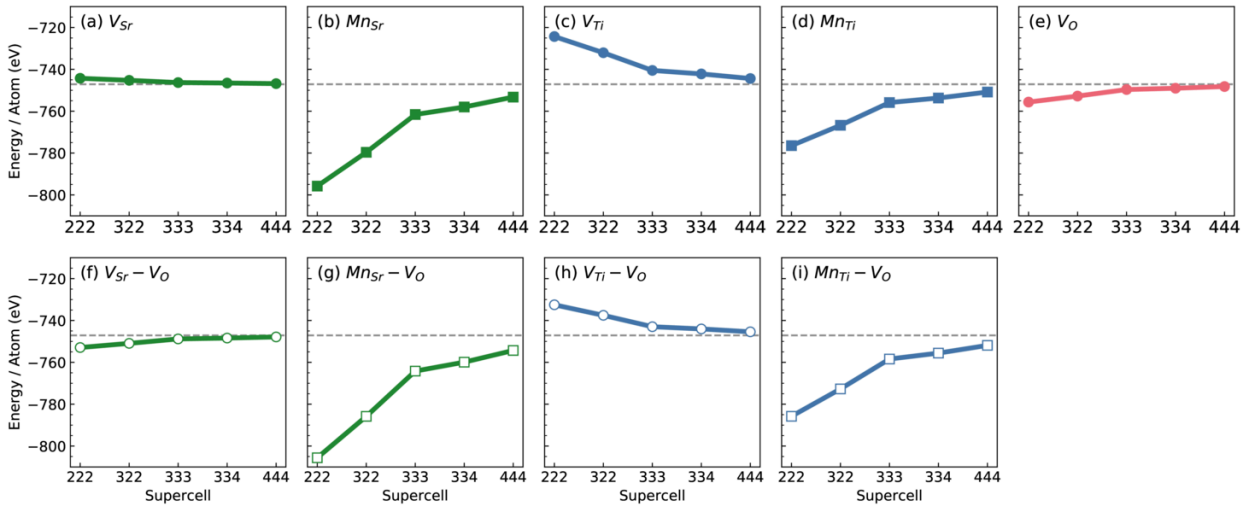

Figure 3.2: Normalized energy per atom for each defect and super cell (a-i). The gray line represents energy of the pure supercells which is relatively invariant.For asymmetric 3 x 2 x 2 and 3 x 3 x 4 supercells, only the x- oriented defect is plotted.

needed understanding of this important material.

Here the first systematic and comprehensive study of the relation between calculated properties of $SrTiO_3$ point defects and supercell size is presented. By focusing on a thorough analysis of both the geometric and electronic properties of each defect, the disappearance of defect-defect interactions and bulk behavior in the dilute range will emerge as supercell size increases. It should be noted that extrapolation of a supercell that is "big enough" for one defect type to another defect type is a hazardous approach as the types of interactions contributing artifacts may be highly variable. Furthermore, with computational studies providing a much higher resolution than current experimental techniques, there is no standard for comparison, and thus the only way to identify such computational artifacts is through thorough systematic benchmarking like the one presented here.

3.2 Computational Methods

In order to probe the relationship between model parameters and calculated properties, we performed DFT calculations on a systematic range of five differently sized supercells varying

from a small 40 atom supercell in which the perovskite A-cell is repeated two times along each lattice vector, to a large 320 atom supercell with four repeats of the A-cell. We refer to each of these supercells in increasing size as 2 x 2 x 2 (40 atoms), 3 x 2 x 2 (60 atoms), 3 x 3 x 3 (135 atoms), 3 x 3 x 4 (180 atoms), and 4 x 4 x 4 (320 atoms) to denote the number of A-cell repeats along the *x*-, *y*-, and *z*-axes respectively. For each supercell, we considered the following vacancies and Mn^{4+} dopants: $(V_{Sr})^{2-}$, $(V_{Ti})^{4-}$, $(V_O)^{2+}$, $(V_{Sr}-V_O)^0$, $(V_{Ti}-V_O)^{2-}$, $(Mn_{Sr})^{2+}$, $(Mn_{Ti})^0$, $(Mn_{Sr}-V_O)^{4+}$, and $(Mn_{Ti}-V_O)^{2+}$. Additionally, the asymmetric 3 x 2 x 2 and 3 x 3 x 4 supercells possess additional defects with two nonequivalent sites for V_O and different distances between periodic defect images, notated as $-V_{Ox}$ and $-V_{Oz}$ to indicate the orientation. We also tested the dependence on supercell net charge and dopant valence by considering the Mn-doped 3 x 3 x 3 supercells with an additional one or two electrons to simulate doping with Mn^{3+} and Mn^{2+} respectively. In total, we calculated energetics, optimized geometry, and electronic structure of 70 different supercells.

Fixed-volume geometry optimizations were carried out using the QuantumEspresso package [49, 50] and a 600 eV cutoff for the planewave basis set with Γ-point sampling of the Brillouin zone. Electron exchange and correlation were accounted for under the generalized gradient approximation (GGA) with the Becke-Lee-Yang-Parr (BLYP) functional [51, 52], which is comparable to literature investigations using PBE and PBEsol [53, 54]. Full band structures of each were calculated with the same conditions and an expanded k-point mesh (Table S1‡). Under this computational setup, calculation of full bands for the largest Mn-doped 3 x 3 x 4 and 4 x 4 x 4 supercells was prohibitively expensive. To confirm the quality of our BLYP-calculated electronic structures, we also performed band calculations of each supercell with the projector-augmented wave (PAW) method in the Vienna Ab Initio Simulation Package (VASP) [55–57] and the hybrid HSE06 functional [7, 58] with Γ-only sampling and same 600 eV energy cutoff. The following core/valence configurations were used for each element: Sr:[Ar]3d/4s4p5s, Ti:[Ne]3s/3p4s3d, O:[He]/2s2p, Mn:[Ne]3s/3p4s3d.

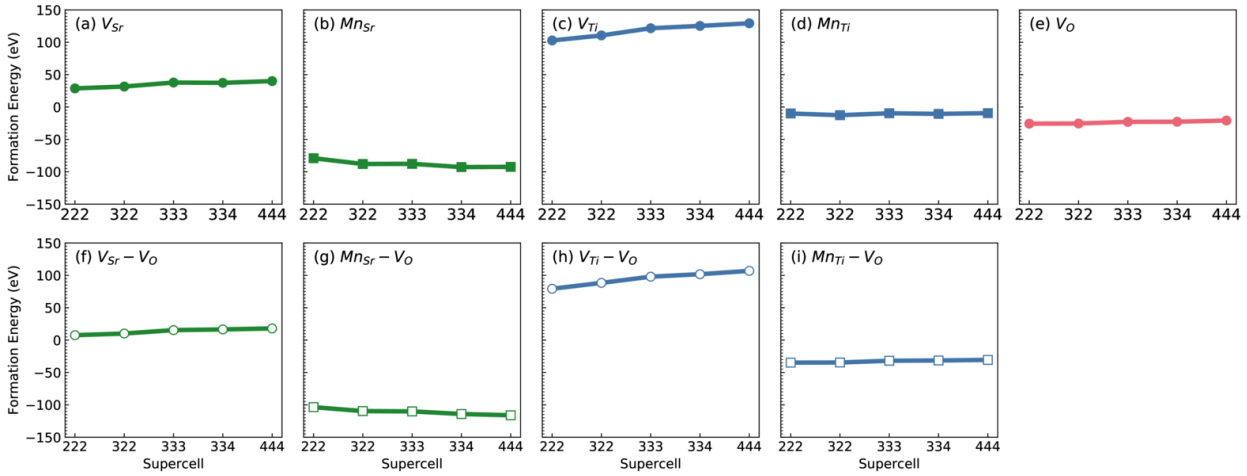

Figure 3.3: Formation energy for each defected supercell (a-i). For asymmetric 3 x 2 x 2 and 3 x 3 x 4 supercells, only the x- oriented defect is plotted.

3.3 Results and Discussion

A detailed analysis of geometry and energetics with respect to supercell size reveals that caution must be taken when designing computational models of defected materials. Different supercell sizes inherently represent different chemistries and defect densities, thus providing varying and potentially unphysical predictions. Computation is always a tradeoff between accuracy and cost. In particular, calculations involving supercells with hundreds of atoms are computationally demanding to optimize. The wall time, reported as total core-hours, for BLYP geometry optimizations (Fig. S2‡) and HSE06 single point calculations (Fig. S3‡) of each defected supercell demonstrates an exponential increase in computational cost when moving to larger cell sizes. Table S2‡ demonstrates this scaling on a per-atom basis for both calculations.

3.3.1 Supercells vs Bulk Geometric Structure

In perovskite oxides, the tuning of the dopant location based on changing synthetic parameters before dopant loading [45] indicates that doped structures are highly dependent on the locations of as synthesized vacancies in the material. To understand the formation of such vacancies, we optimized all possible single atom vacancies, V_{Ti}, V_{Sr}, and V_O.

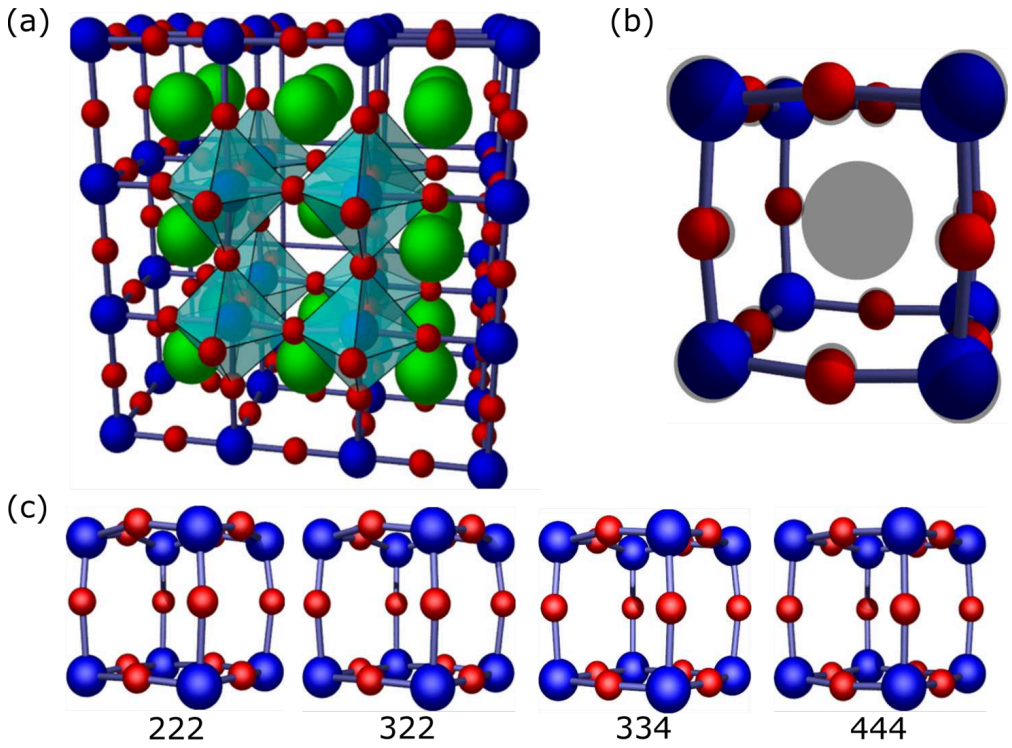

Figure 3.4: Cutaway of 3 x 3 x 3 V_{Sr} supercell with defect surrounding TiO_6 octahedra (a), and enlarged defected A-cell from 3 x 3 x 3 supercell with locations of atoms in the pure lattice shaded (b). Defected A-cells from each differently sized supercells (c). Color code: Sr = green, Ti = blue, O = red.

Generally, structural distortions are largest for the smaller supercells, and converge to the bulk $SrTiO_3$ structure as the number of atoms in the supercell increases. Structural deviation is quantified for each supercell and defect type by comparing the average adjusted mean Sr-O and Ti-O bond lengths (Fig. 3.1a-i). In almost all supercells, optimization decreases the average Sr–O bond length (μ) and increases the average Ti–O bond length. The nature of the convergence to bulk structure reveals three different patterns of cell-wide structural distortion: (i) asymmetric supercells can result in increased distortion, best illustrated by considering the Mn_{Ti} defect (Fig. 3.1d). (ii) A number of defects studied here are capable of inducing cell-wide antiferrodistortive-like rotations of Ti-O octahedra. We calculate these out-of-phase rotations to be $\theta \approx 1.0°$ around the b-axis in the 4 x 4 x 4 V_{Sr}–V_O supercell (Fig. S7‡). Such rotations are largely driven by geometric constraints [59] with experimental measurement of strained undoped $SrTiO_3$ at θ=2.01° at 50 K [60]. Further distortion of these octahedra occurs from off-centering of the central Ti atoms. This reduces the symmetry of each octahedra from O_h to C_{3v} and results in a bimodal distribution of Ti-O bondlengths around the pure value for a large number of supercells (Fig. S8-S11‡). This second symmetry-lowering effect likely arises from electronic instabilities of the Ti atom [61], and explains the unique shapes of Ti-O deviation for V_{Sr}–V_O and Mn_{Sr}–V_O (Fig. 3.1f & 3.1g). (iii) The periodic boundary conditions of 2 x 2 x 2 and 3 x 2 x 2 supercells can induce unusually high structural distortion. This is best illustrated in the case of V_{Ti} (Fig. 3.1c), where the bulk structure is dramatically achieved at the 3 x 3 x 3 supercell. The high distortion in the smallest supercells arises from the high density of defects, and boundary-spanning reorganizations that may introduce nonphysical artifacts into calculated geometries.

Analyzing the energy per atom for each supercell further shows exceptionally high deviation from the bulk value for defected supercells smaller than 3 x 3 x 3 (Fig. 3.2 & Table S3‡). In the undefected supercells, the energy per atom is invariant at 747 eV/atom (Table S3‡). Defected supercells converge towards this value nonlinearly as the size of the supercell increases. In the case of V_{Sr} and V_{Sr}–V_O (Fig. 3.2a & 3.2f), this effect is minimal as the energy slightly decreases

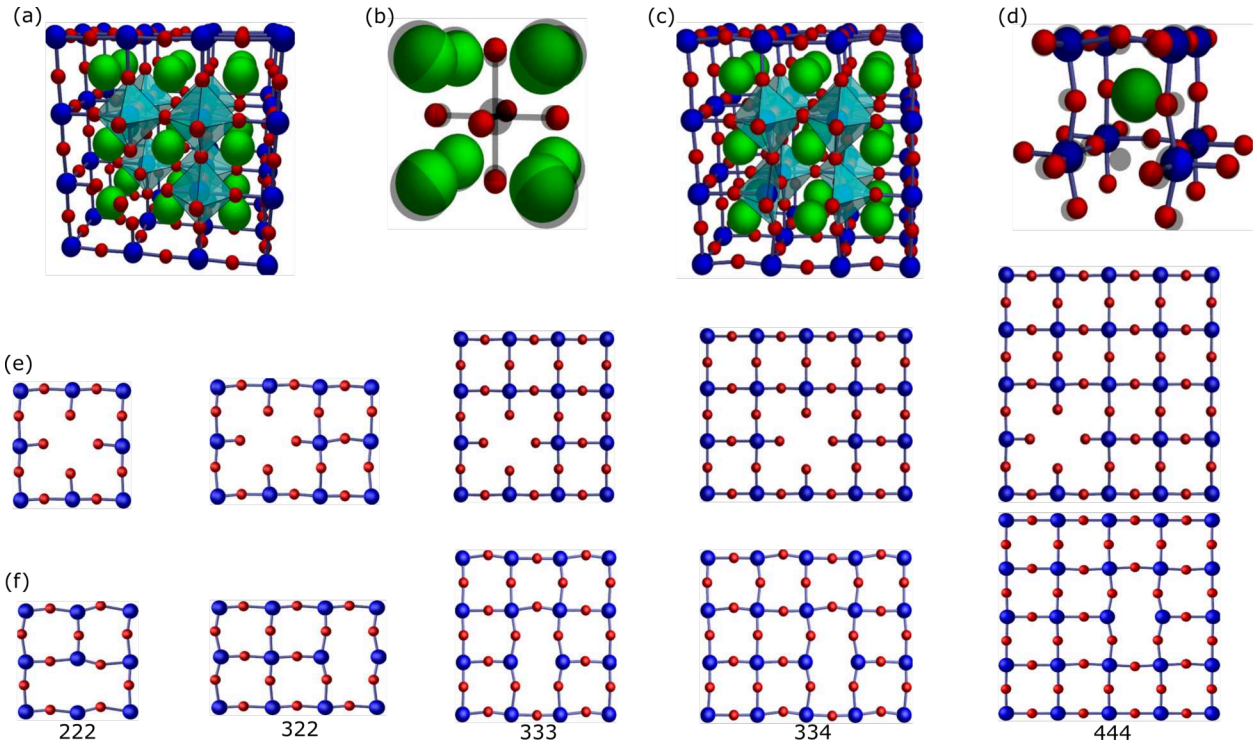

Figure 3.5: Cutaway of 3 x 3 x 3 V_{Ti} (a) and V_O (c) supercells with defect surrounding TiO_6 octahedra. Enlarged V_{Ti} B-cell (b) and enlarged V_O A-cell (d) from 3 x 3 x 3 supercell with locations of atoms in the pure lattice shaded. Cubic lattice in the defect plane from the V_{Ti} (e) and V_{Ti}-V_O (f) for each differently sized supercell. For asymmetric 3 x 2 x 2 and 3 x 3 x 4 supercells, only the x- oriented defect is shown. Color code: Sr = green, Ti = blue, O = red.

or increases to the reference value respectively. This small deviation is possibly attributed to the highly electropositive nature of Sr, whereas disruption of the covalent Ti-O cubic lattice results in much larger deviation from bulk value in V_{Ti} and V_{Ti}–V_O supercells (Fig. 3.2c & 3.2h). The largest deviation occurs for the Mn-doped supercells which always increase to the reference value (Fig. 3.2b, 3.2d, 3.2g & 3.2i).

The formation energy is less dependent on unit cell size than energy per atom, and generally shows a marginal increase with increasing cell size (Fig. 3.3 & Table S4‡). We calculate formation energy according to the formula:

$$E_{form} = E_{doped} - E_{pure} + E_x - E_{Mn}$$

Where E_{doped} and E_{pure} are the final BLYP energies of each optimized supercell, and E_x and

E_{Mn} are the energies of the defect and dopant atoms in an empty vacuum cell of respective size. Both single metal vacancies result in endothermic formation energies with the largest occurring for V_{Ti} in excess of 100 eV (Fig. 3.3c). Exclusion of an adjacent oxygen vacancy to form the V_{Ti}–V_O defect lowers this value slightly (Fig. 3.3h), and subsequent doping to Mn_{Ti}–V_O brings exothermic formation energy to approximately −10 eV in the 3 x 3 x 3 supercell (Fig. 3.3i). A similar trend occurs for A-site defects with formation energy greatest for the endothermic single atom vacancy V_{Sr} (Fig. 3.3a), and most favorable formation energies occurring for the highly exothermic Mn-doped double defect, Mn_{Sr}–V_O (Fig. 3.3g). Exothermic formation energies are predicted for the V_O defect (Fig. 3.3e), and there is no apparent dependence on orientation of the defect (Table S4‡). The lower formation energies of A-site defects than B-site defects have been seen previously[40]. Interestingly, vacancy of the nearest neighbor oxygen site stabilizes both metal site vacancies.

Based on the structure, energy per atom, and formation energies, the 3 x 3 x 3 supercell is ideal for modeling the chemistry of vacancies and Mn-dopants in $SrTiO_3$. By balancing computational expense with an accurate description of structure, the 3 x 3 x 3 supercell critically does not suffer from the ambiguous periodic boundary conditions of the 2 x 2 x 2 and 3 x 2 x 2 supercells. This hypothesis is tested by next considering the specific geometry of each defected cell.

3.3.2 Geometry of Single Defect Sites

Geometry of the V_{Sr} defect site (Fig. 3.4) indicates minimal reorganization of the defect-adjacent atoms with the surrounding TiO_6 octahedra remaining largely in their native orientation (Fig. 3.4a). Extracting the nearest neighbors to the vacancy from the 3 x 3 x 3 supercell in Fig. 3.4b (*i.e.* the defected A-cell) shows a slight movement of neighboring atoms around the vacancy, with each of the O atoms bowing slightly outwards and Ti atoms moving inwards toward the defect (gray atoms in Fig. 3.4b show the bulk atom locations). This same defect site geometry appears to be predicted by all supercells (defect separation from 7.89 – 15.78 Å, Fig. 3.4c),

similarly to the reported V_{Sr}^{2+} geometries [35]. Quantitative analysis of the defect geometry achieved by calculating the volume of a convex hull constructed from the defect adjacent atoms (Fig. 3.6a) and measuring displacement of nearest neighbor atoms (Fig. 3.6d) reveals slight deviation between each supercell. We calculate the nearest neighbor displacement [26] as:

$$\langle \delta_{\mathrm{NN_x}} \rangle = \frac{1}{N} \sum \delta_i$$

Where x and N are the type and number of atoms considered, and δ_i is the displacement of each atom from its starting position in the pure crystal lattice. Specifically in V_{Sr}, we observe an increase in the reorganization of the defect adjacent Ti atoms ($\langle \delta_{\mathrm{NN_{Ti}}} \rangle$, blue line in Fig. 3.6e) in the 2 x 2 x 2 and 3 x 2 x 2 supercells resulting in a slightly larger defect volume of approximately 4 $\mathrm{Å}^3$.

The 3 x 3 x 3 supercell predicts comparable results for V_{Ti} with the surrounding octahedra remaining intact (Fig. 3.5a) and the defected B-cell (Fig. 3.5b) showing neighboring Sr atoms shifting inward towards the vacancy site and O atoms moving directly towards their bonded Ti partners. Aside from this small reduction in Ti–O bond lengths, the cubic lattice remains free from significant distortion in the supercells 3 x 3 x 3 and larger (Fig. 3.5e), matching previously observed results [35]. Contrarily, the optimized 3 x 2 x 2 and 2 x 2 x 2 supercells predict significantly more out of plane restructuring. While Fig. 3.6e indicates Sr reorganization to be the primary contribution to nearest neighbor displacements, the large restructuring seen in the 2 x 2 x 2 and 3 x 2 x 2 is driven by periodic boundary condition-induced destabilization. In these supercells, a significant percentage of Ti atoms are bound two negative charged O atoms directly adjacent to the defect, which causes significant strain to the TiO_6 octahedra. During optimization, defect adjacent O atoms no longer migrate exclusively along one lattice vector directly towards their bonding partner as in Fig. 3.5b, but rather in multiple dimensions causing the observed distortions. Because the nearest neighbors plot (Fig. 3.6e) only accounts for displacement and not directionality, this effect is not readily apparent. These differences in

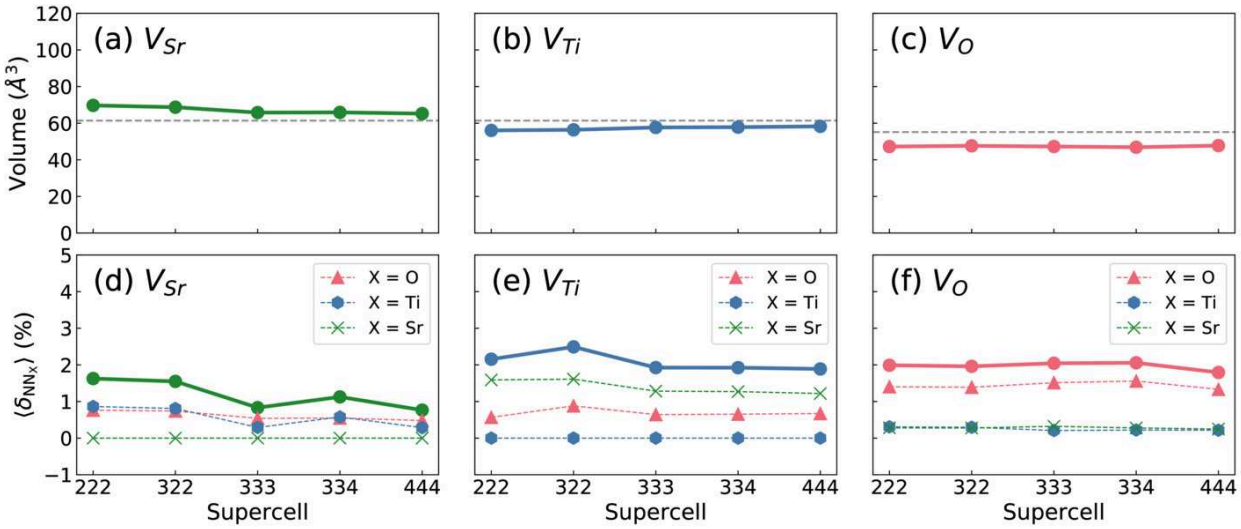

Figure 3.6: Defect volumes (a-c) and nearest neighbor (d-f) displacements for single vacancies. Defect volumes are approximated by a convex hull constructed from the nearest 20 lattice atoms for V_{Sr} defects and nearest 14 lattice atoms for V_{Ti} and V_O defects. Nearest neighbor migrations are calculated as displacement of these same lattice atoms from the pure crystal structure. The solid line in nearest neighbor plots represents total displacement, while the green, blue, and red dashed lines represent the atom-resolved displacements. For asymmetric supercells, only the x-oriented defect structure is plotted.

calculated geometry underscore the necessity of selecting a large enough supercell for simulation of defects in cubic perovskites.

Analysis of V_O (Fig. 3.5c) shows that each of the four nearest neighboring O atoms bonded to the undercoordinated Ti atom move inwards towards the defect (Fig. 3.5d & 3.5f), whereas the remaining O atoms comprising the rest of the defected A-cell and bonded parallel to the vacancy bend outward. Similarly, the undercoordinated Ti atoms move slightly outward away from the defect while the neighboring Sr remains in its native position (Fig. 3.5d). The tetrahedral geometry of the undercoordinated Ti atom results in significant octahedral tilt (Fig. 3.5c). This geometry is generally well-captured by each of the supercells (Fig. 3.5f), and matches the geometries calculated by Zhang et al [31]. Interestingly, the outward motion of parallel bonded O atoms is repressed in supercells 2 x 2 x 2 and 3 x 2 x 2, due to the opposing forces arising from periodic boundary conditions. This fact is well reflected in defect volume and nearest neighbor displacements (Fig. 3.6c & 3.6f), which are fairly constant.

3.3.3 Geometry of Double Defects

Experimental structures of Mn-dopants next to oxygen vacancies have been observed [44, 45]. If these structures arise from filling a metal vacancy site that is already next to an oxygen vacancy, then the energetics and geometries of the double defects consisting of a vacancy of both a metal atom and adjacent oxygen are critical. Here, we consider only the nearest neighbor double defect, which results in a defect separation of $\approx$ 6 - 14 Å.

The 3 x 3 x 3 V_{Sr}–V_O defect cell displays the characteristics of the two corresponding single defects. Those O atoms bonded to the undercoordinated Ti atoms and comprising the neighboring Sr-occupied A-cells are pulled inward (Fig. 3.7b & 3.7e), just as before in the V_O defect geometry (Fig. 3.5). Similarly, the undercoordinated Ti atoms also move away from the defect site. The remaining defect adjacent Ti and O atoms comprising the vacant A-cell are characteristic of the V_{Sr} defect geometry with oxygen atoms buckling outward from the defect site, and slight migration of Ti atoms inward. Analysis of supercells smaller than 3 x 3 x 3 is confounded by the large structural distortion caused by the high defect density and periodic boundary condition induced reorganization. Notably, the 3 x 2 x 2 V_{Sr}–V_O supercell fails to capture the V_{Sr} defect geometry component (Fig. 3.7e), instead predicting the geometry of a single V_O defect where all O atoms adjacent to the defect and bonding with the undercoordinated Ti move inwards, losing the outward buckling observed in V_{Sr} defected cells. The high degree of reorganization and unique geometries predicted by the 2 x 2 x 2 and 3 x 2 x 2 supercell account for an unusually high nearest neighbor displacement contributed by large reorganization of O atoms (Fig. 3.8b).

The V_{Ti}–V_O defect is also best viewed as a composition of two single-defect geometries. The five singly bonded oxygens neighboring the Ti vacancy in the defected B-cell (Fig. 3.7c) migrate towards their sole bonding partners, as in the singly defected V_{Ti} cells. Four of these O atoms closest to double vacancy move additionally towards the vacant O site. The four Sr atoms nearest the vacant B site migrate significantly inwards towards the vacancy, while the Sr atoms adjacent to the oxygen vacancy are relatively fixed in their native lattice positions. Those

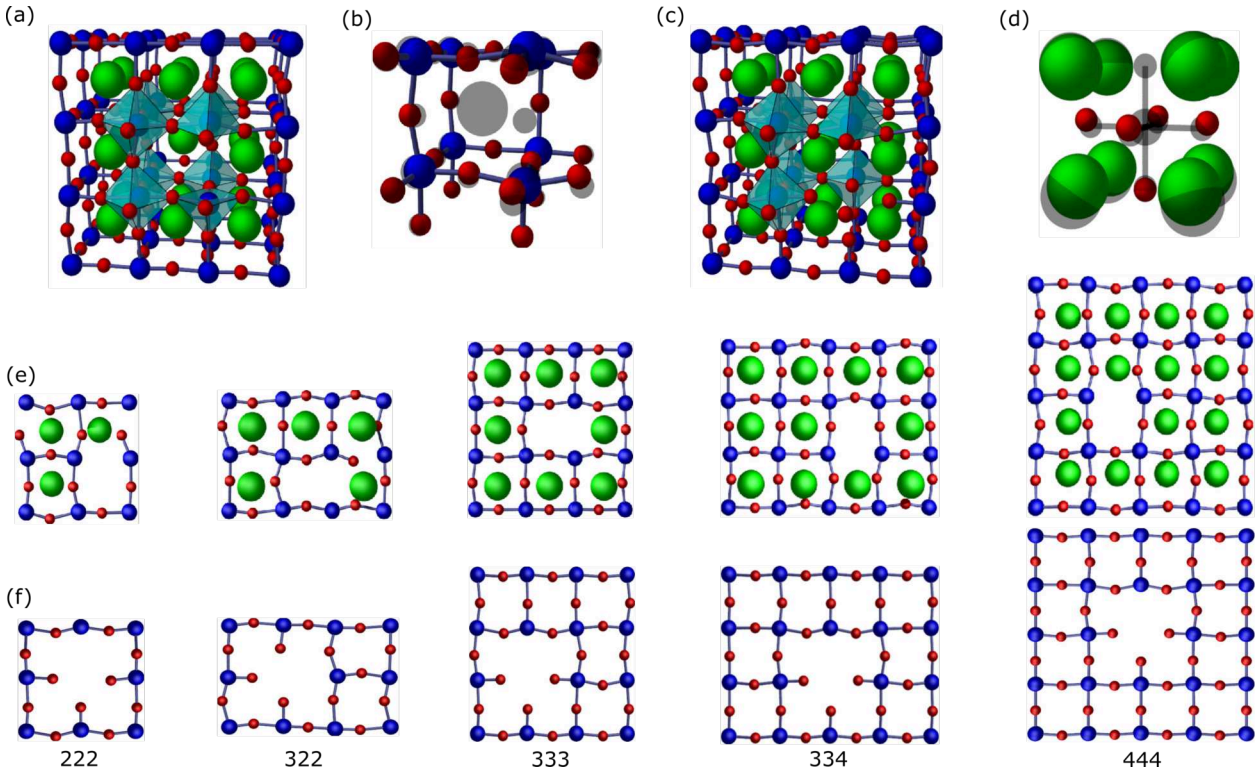

Figure 3.7: Cutaway of 3 x 3 x 3 V_{Sr}–V_O (a) and V_{Ti}–V_O (c) supercells with defect surrounding TiO_6 octahedra. Enlarged V_{Sr}–V_O A-cell (b) and enlarged V_{Ti}–V_O B-cell (d) from 3 x 3 x 3 supercell with locations of atoms in the pure lattice shaded. Cubic lattice in the defect plane from the V_{Sr}–V_O (e) and V_{Ti}–V_O (f) for each differently sized supercell. For asymmetric 3 x 2 x 2 and 3 x 3 x 4 supercells, only the x- oriented defect is shown. Color code: Sr = green, Ti = blue, O = red.

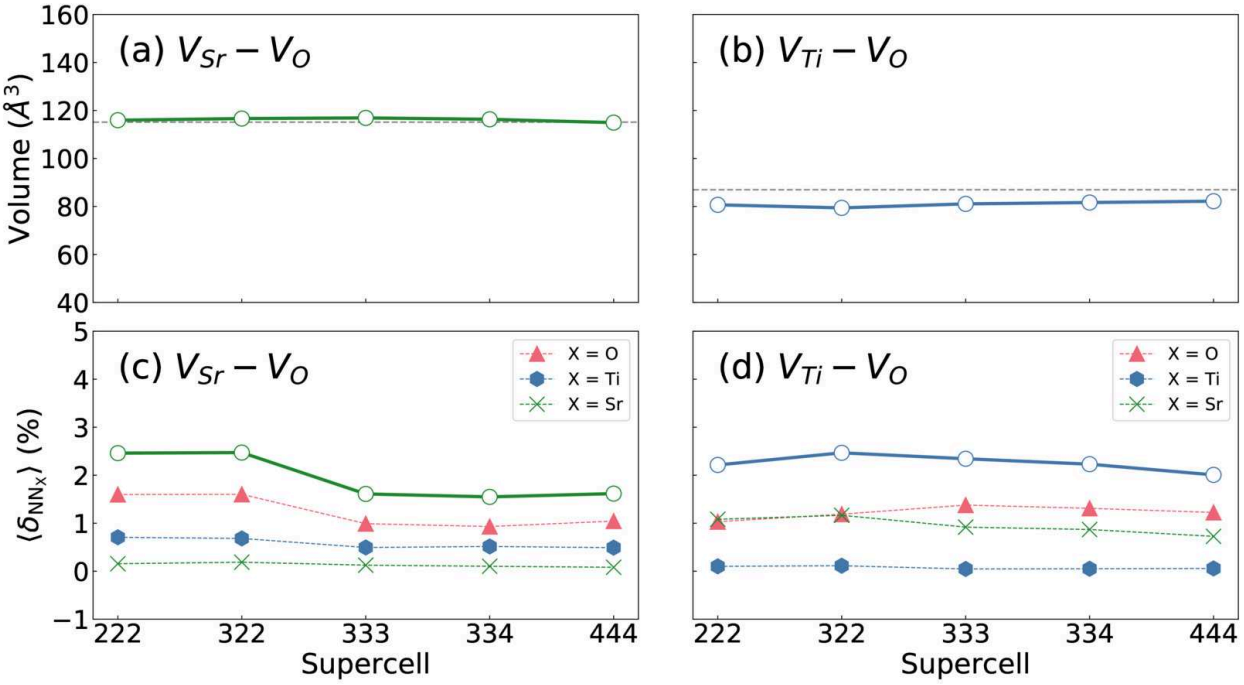

Figure 3.8: Defect Volumes (a-c) and Nearest Neighbor (d-f) displacements for double vacancies. Defect volumes are approximated by a convex hull constructed from the nearest 26 lattice atoms for V_{Sr}–V_O defects and nearest 18 lattice atoms for V_{Ti}–V_O defects. Nearest neighbor migrations are calculated as displacement of these same lattice atoms. For asymmetric supercells, only the x-oriented defected structure is plotted.

O atoms opposite the Ti vacancy and bound to the undercoordinated Ti move inward forming a tetrahedral geometry (Fig. 3.7f) as in the V_O supercells. In supercells 3 x 3 x 3 and larger, this inward movement results in tilting the adjacent TiO_6 octahedra with O atoms bonded parallel to the vacant O site moving outwards away from the defect (Fig. 3.7c & 3.7f). However, in 2 x 2 x 2 and 3 x 2 x 2 V_{Ti}–V_{Ox}, this octahedral tilt is largely repressed. To achieve the same geometry of the optimized 3 x 3 x 3 supercell under the equivalence of atoms imposed by the periodic boundary conditions of these smaller cells, a single TiO_6 octahedra would have to simultaneously rotate clockwise and counter-clockwise. These two opposing forces result in very little net movement, and a subsequent failure to describe the bonding of these atoms and their relaxation around the vacancy. Notably, the 3 x 2 x 2 V_{Ti}–V_{Oz} (Fig. S8‡) defect is successful in capturing this reorganization as tilt occurs along its lattice vector with period 3, eliminating equivalence restrictions.

The effect of periodic boundary conditions on the optimized geometry is also clearly visible in the nearest neighbor displacements (Fig. 3.8d). For the two smallest supercells, the reorganization of Sr and O atoms are the major contributors to nearest neighbor displacements with the contribution of Ti atoms negligible. At the 3 x 3 x 3 supercell, Sr displacement is reduced and O displacement is increased to become the major contributor. In the two smallest supercells, the Ti–O cubic lattice is more rigid due the opposing forces created by periodic boundary conditions as previously discussed, justifying the increase in O reorganization at the 3 x 3 x 3 supercell. Similarly, O vacancies in the cubic lattice are stabilized by increased interactions with the Sr atoms evidenced by migration of oxygens around a vacancy towards the Sr atoms in V_O defects. With the periodic boundary-imposed rigidity in the cubic lattice, the Sr–O stabilization interaction is able to overcome the mass difference between Sr and O atoms, and subsequently the Sr atom is pulled, justifying the increased Sr displacement (Fig. 3.8d).

3.3.4 Geometry of Dopants

Optimized geometries of an Mn^{4+} ion substituting for Sr show occupation of an off-center lattice position in agreement with previous studies [46, 48, 62, 63]. In the cubic supercells, the Mn ion migrates along all three lattice vectors to a corner of the defected A-cell (Fig. 3.9b). Here, the nearest Ti atom is displaced from the center of its octahedra (Fig. 3.9a), leaving three O atoms to triply coordinate the Mn ion. Those Ti atoms sharing bonding partners with the Mn ion are displaced away, while the remaining four Ti atoms are pulled inwards. With the exception of those lattice ions directly interacting with dopant, the geometry predicted by the cubic supercells is similar to that of V_{Sr}. Notably, the Mn_{Sr} defect is sensitive to the symmetry of the supercell, with a critically different defect geometry predicted for the asymmetric super cells (Fig. 3.9c). In each case, the Mn ion continues to occupy an off-center lattice position, yet reorganization of the dopant ion only occurs in the lattice vector for which the supercell has the greatest period. In the case of the 3 x 2 x 2 and 3 x 3 x 4 supercells, there is minimal change in the yz- and xy-coordinates of the Mn ion respectively. Consequently, a 4-coordinate face-centered

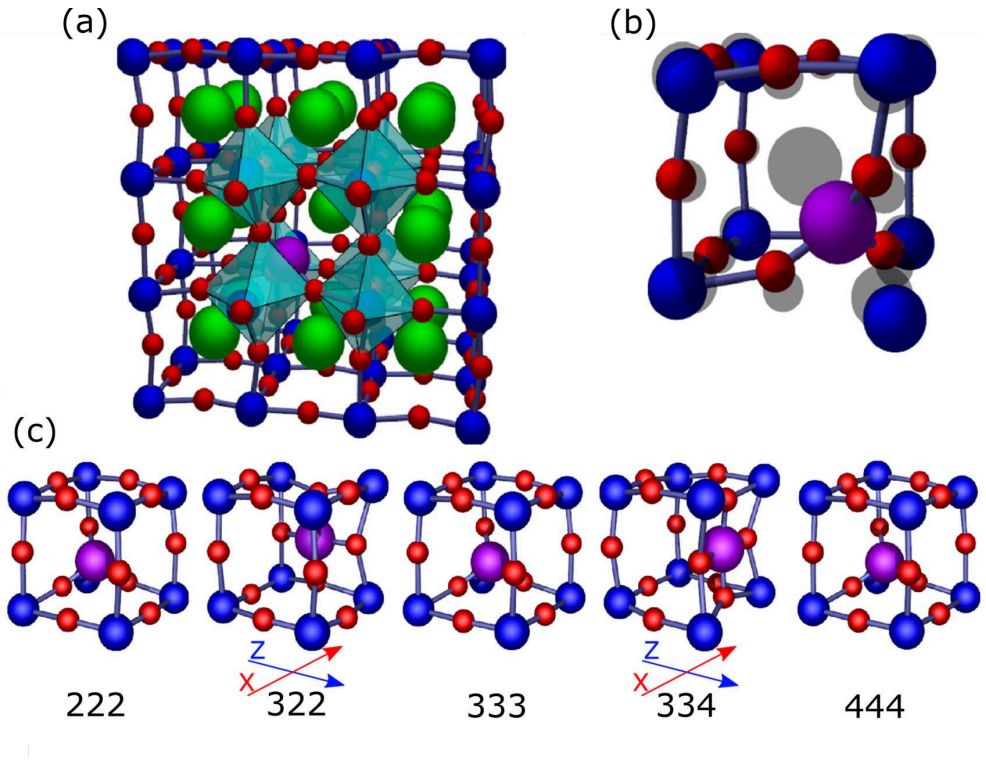

Figure 3.9: Cutaway of 3 x 3 x 3 Mn_{Sr} supercell with defect surrounding TiO_6 octahedra (a), and enlarged defected A-cell with locations of atoms in the pure lattice shaded (b). Defected A-cells from each differently sized supercells (c). Color code: Sr = green, Ti = blue, O = red, Mn = purple.

defect complex is formed (coordination number [64] approximately 4.6 (Table S6‡). Because the dopant no longer approaches a B-site ion in this defect geometry, all Ti atoms remain centered in their octahedra, as indicated by the reduced nearest neighbor displacement for Ti in asymmetric supercells (Fig. 3.12e). However, the implication of four O atoms in formation of the face-centered complex contribute to an increase in the total nearest neighbor displacements for asymmetric supercells. Doping the 3 x 3 x 3 supercell with aliovalent Mn^{2+} and Mn^{3+} ions each predict a distinct 5-coordinate Mn complex (coordination numbers approximately 4.8 and 4.4 respectively, Table S6 and Fig. S13‡) where the dopant moves along two lattice vectors to the edge of a supercell, to produce a square pyramidal dopant complex not captured by any of the $Mn^{4+}{}_{Sr}$ supercells.

Importantly, while the Mn location in the supercells varies widely, the coordination numbers (Table S6‡) are all in the 4.4–4.8 range. It would be interesting to see if X-ray absorption

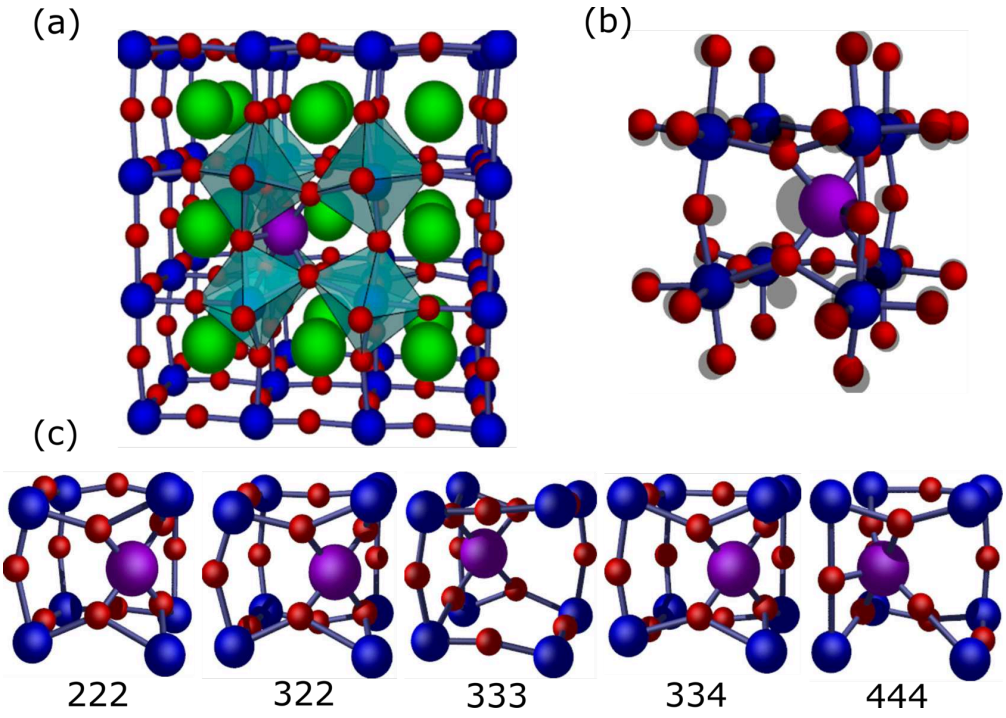

Figure 3.10: Cutaway of 3 x 3 x 3 Mn_{Sr}–V_O supercell with defect surrounding TiO_6 octahedra (a), and enlarged defected A-cell with locations of atoms in the pure lattice shaded (b). Defected A-cells from each differently sized supercells (c). For asymmetric supercells, only the x-orientated defect is shown. Color code: Sr = green, Ti = blue, O = red, Mn = purple.

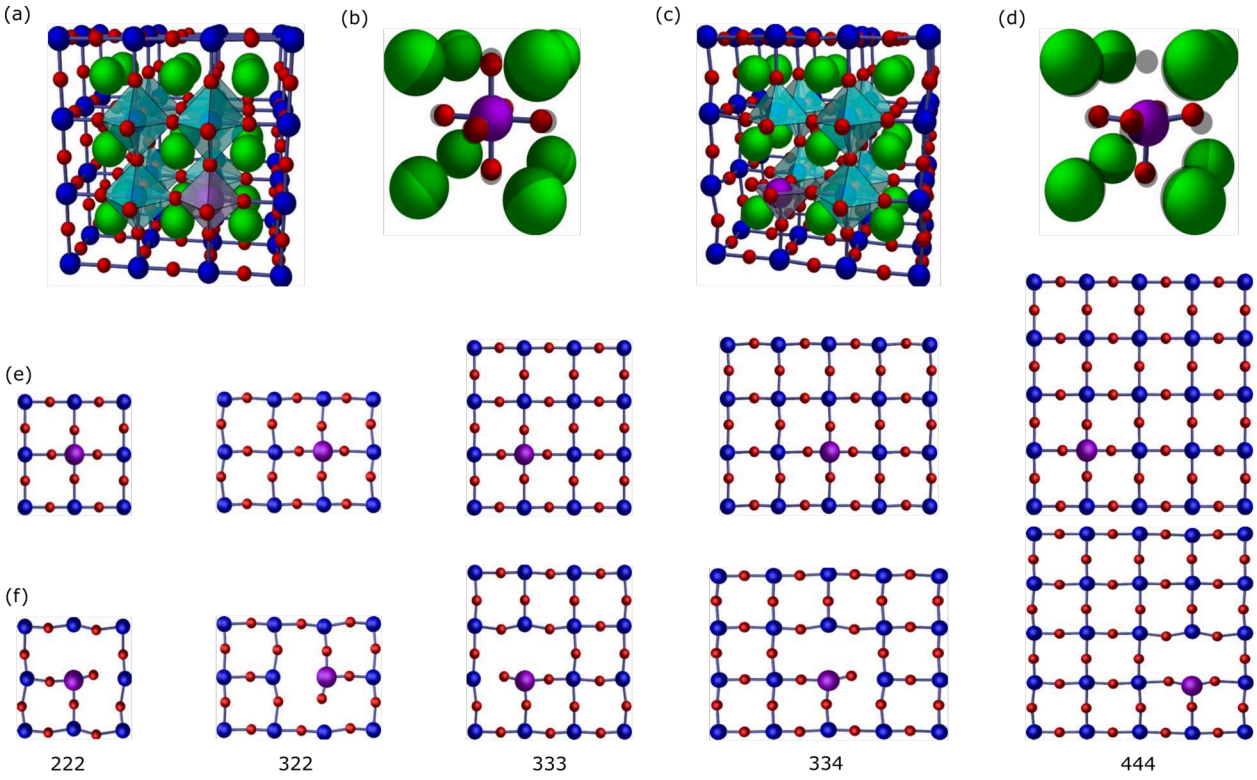

Figure 3.11: Cutaway of 3 x 3 x 3 Mn_{Ti} (a) and Mn_{Ti}–V_O (c) supercells with defect surrounding TiO_6 octahedra. Enlarged Mn_{Ti} B-cell (b) and enlarged Mn_{Ti}–V_O B-cell (d) from 3 x 3 x 3 supercell with locations of atoms in the pure lattice shaded. Cubic lattice in the defect plane from the Mn_{Ti} (e) and Mn_{Ti}–V_O (f) for each differently sized supercell. For asymmetric 3 x 2 x 2 and 3 x 3 x 4 supercells, only the x- oriented defect is shown. Color code: Sr = green, Ti = blue, O = red, Mn = purple.

spectroscopy (XAS) pre-edge features, which indicate the degree of disorder within polyhedra, could be used to determine if there is one clear Mn structure. While measurements like high energy x-ray scattering pair distribution function (PDF) might have this level of resolution for bulk samples, it would be interesting to see if anything can be determined experimentally about dopant geometries. Without such evidence, one must assume that a range of Mn structures exist in real materials and thus must be modeled to capture the range of possible electronic effects.

The geometry of the Mn_{Sr}–V_O defect is also sensitive to the supercell size varying with the location of the off-center Mn ion (Fig. 3.10c). In each case, the Mn dopant reorganizes along 2 lattice vectors causing significant octahedral tilt as it coordinates with O atoms (Fig. 3.10a). For the 2 x 2 x 2, 3 x 2 x 2, and 3 x 3 x 4 supercells (Fig. 3.10c), the Mn is positioned directly towards

the oxygen vacancy and forms a 4-coordinate Mn complex, distinct from the face-centered Mn complex calculated for the asymmetric Mn_{Sr} defected cells. The 4-coordinate Mn complex is not sensitive to the orientation of the oxygen vacancy in the asymmetric supercells with similar structures predicted for both orientations. A significantly different defect geometry is calculated for the 3 x 3 x 3 and 4 x 4 x 4 supercells, both forming a 5-coordinate Mn complex. However, these supercells differ from each other with the Mn ion moving directly away from (Fig. 3.10b) or parallel to (Fig. 3.10c) the O vacancy respectively. Doping the 3 x 3 x 3 supercell with aliovalent Mn^{2+} or Mn^{3+} removes this effect (Fig. S9‡) and reveals the 4-coordinate Mn complex like those predicted by the 2 x 2 x 2, 3 x 2 x 2, and 3 x 3 x 4 $Mn_{Sr}{}^{4+}$–V_O structures. Despite the dramatic difference between the different Mn_{Sr}–V_O defect geometries, the nearest neighbor displacement is relatively constant (Fig. 3.12f). In each case, reorganization of adjacent O atoms is the major contributor, with marginal contributions by Sr and Ti atoms. However, the different defect geometries are detectable by volume (Fig. 3.12b), with the five coordinate Mn complex formed in 3 x 3 x 3 and 4 x 4 x 4 supercells approximately 10 $Å^3$ smaller than the 2 x 2 x 2 and 3 x 2 x 2 supercells.

Unlike the dramatic variation and distortion of the Mn_{Sr}–V_O, Mn_{Ti} defected supercells show minimum disruption of the native crystal structure (Fig. 3.11a), probably as the Mn^{4+} ion is similar in size to the substituted Ti. In all supercells, defect adjacent O atoms are pulled towards the substituting Mn ion (Fig. 3.11e), reducing the neighboring bond lengths in the cubic lattice from 1.97 Å to approximately 1.82 Å. Unlike in the singly defected V_{Ti} supercells, the Sr atoms comprising the B-cell are relatively fixed in cubic supercells (Fig. 3.11b). Notably, there is increased reorganization of the Sr atoms for the asymmetric supercells indicated by the nearest neighbor displacements (Fig. 3.12g), a phenomenon which may coincide with the cell-wide folding previously discussed. Geometry optimizations of 3 x 3 x 3 supercells with Mn^{2+} and Mn^{3+} as dopant ions optimize to a similar geometry as their Mn^{4+} doped counterparts (Fig. S9‡) to a comparable Mn–O bond length of 1.83 Å in both oxidation states.

Like the Mn_{Sr}–V_O defect, optimization of Mn_{Ti}–V_O defected supercells also reveals varying

defect geometries dependent on supercell size. In all supercells, those O atoms adjacent to the vacancy move inward (Fig. 3.11f), similar to the reorganization of the V_O defect (Fig. 3.5), and those bonded to the dopant ion experience the bond length shortening characteristic of the Mn_{Ti} defect (Fig. 3.11). However, in some of the supercells, reorganization of certain O atoms adjacent to the vacancy and bound to the dopant ion (henceforth referred to as neighboring O atoms) is much greater resulting two inequivalent Mn–O bond lengths of 1.67 Å and 1.89 Å as measured in the 3 x 3 x 3 supercell. As a consequence, O atoms closer to the Mn ion are no longer equivalent to the remaining neighboring O atoms, and are out of bonding distance with their Ti partners, whose subsequent reorganization further increases the distance between the two atoms to 2.48 Å. Of the 4 neighboring O atoms, inequivalence of this type arises for two (one shown in Fig. 3.11f) and is only observed in supercells 2 x 2 x 2, 3 x 2 x 2, 3 x 3 x 3, and 3 x 3 x 4 ($-V_{Ox}$ direction only)). This subtle difference in geometry is not detectable by the nearest neighbor displacement or volume measures (Fig. 3.12d & 3.12h). The fact that this effect is diminished for the long 3 x 3 x 4 V_{Oz} and 4 x 4 x 4 supercells indicates that the appearance of these inequivalent neighboring O atoms might just be an artifact of close packing of the defects or defect-defect interactions in the periodic structure. Interestingly, doping with Mn^{2+} reduces the inequivalence of Mn—O bond lengths to 1.76 and 1.84 Å, and inequivalence is completely diminished with Mn^{3+} where all vacancy adjacent Mn–O bond lengths at 1.78 Å.

3.3.5 Electronic Structure of Undefected and V_O Supercells

The effect of supercell size on calculated electronic properties is readily apparent even in the undefected supercells. Generally, the Γ-only HSE06 calculated bands (Fig. 3.13a) align well with the full band structures and density of states (DOS) calculated with the BLYP functional (Fig. S10‡). Both functionals confirm the valence band (VB) to have mainly oxygen *2p* character, and the conduction band (CB) primarily contributed by Ti t_{2g} orbitals. The full band structures show conduction band minima (CBM) occuring at points Γ and X, while location of the valence band maximum (VBM) varies for each supercell. This variation is due in part to differing atomic

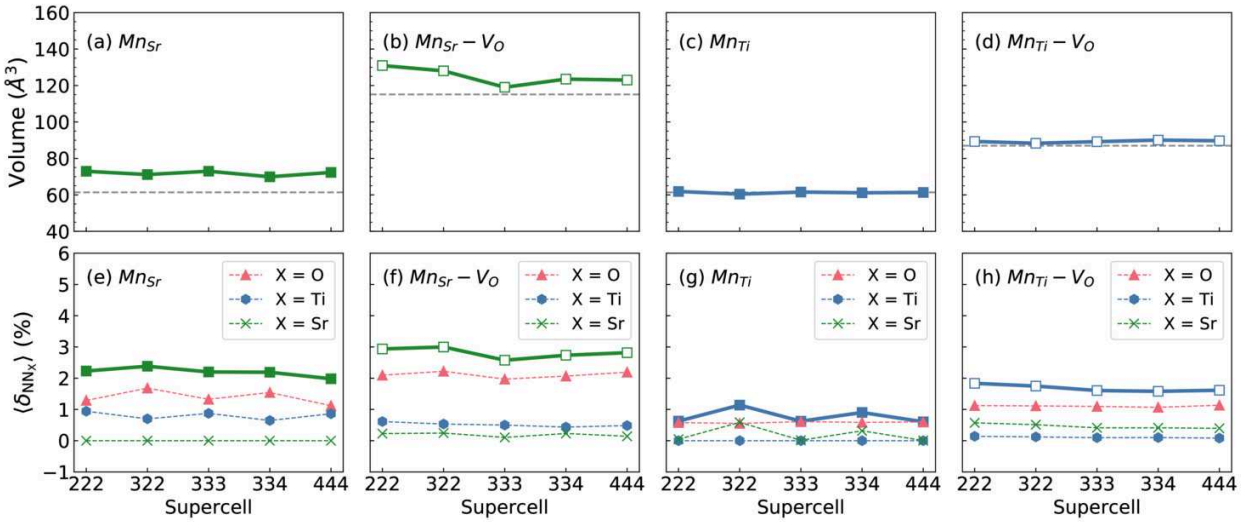

Figure 3.12: Defect Volumes (a-c) and Nearest Neighbor (d-f) displacements for doped supercells.

species at the same high symmetry point in different supercell sizes (Table S7‡). In supercells with an even period in all three lattice vectors, each high symmetry point is centered on a Ti atom, contributing VBM at points X and Γ. In the 3 x 3 x 3 supercell, X and Γ correspond to minima of the valence band, and coincide with an A-cell face center and Sr atom respectively, whereas VBM in these supercells correspond to Ti and O atoms at points M and R. In the BLYP predicted band structures, the magnitude of the band gap (E_g) in pure supercells very consistent at approximately 1.85 eV. However, the hybrid HSE06 functional predicts a much larger E_g with higher variation ranging from a minimum of 2.92 eV in the 2 x 2 x 2 supercell to a maximum of 3.51 eV in the 3 x 3 x 3 supercell. The larger supercells are within computational error of the experimental E_g (3.2 eV, direct 3.7 eV) [65]. We suspect the maximum E_g occurs in the 3 x 3 x 3 supercell as a result of the Γ point sampling, which is centered on a Sr-atom for only the 3 x 3 x 3 supercell.

V_O leads to a large increase in the magnitude of E_g predicted by both the HSE06 (Fig. 3.13b) and BLYP (Fig. S10‡) functional. In the full BLYP band structures, E_g is increased to a maximum of about 2.70 eV in the 2 x 2 x 2 supercell, gradually converging to bulk value in the large 4 x 4 x 4 supercell. The HSE06 predicted E_g also decreases as supercell size is increased. Other reports have shown a narrowing of E_g [35, 36]. There is limited dependence

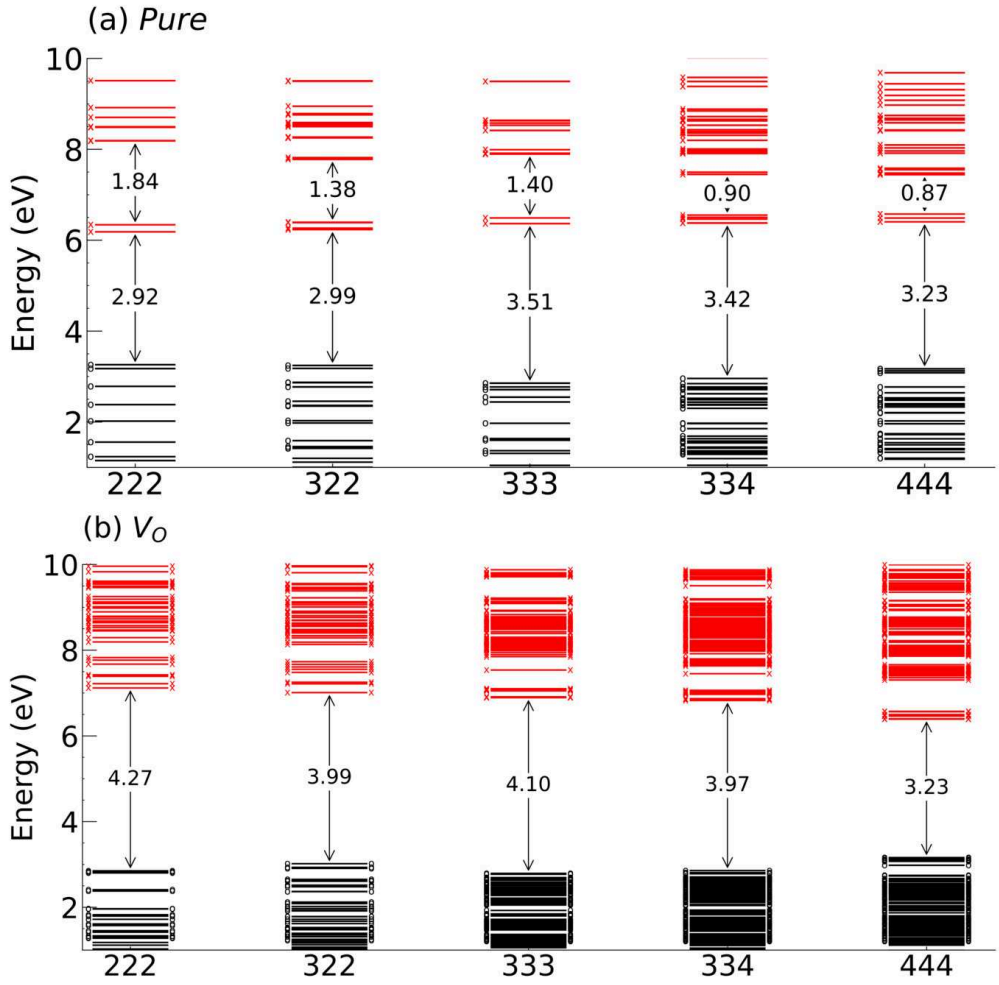

Figure 3.13: HSE06 predicted bands and charge densities at Γ for undefected (a) and V_O (b). Unoccupied orbitals are marked with red and with x. Occupied orbitals are marked in black and with o. Only the x-orientation is plotted for asymmetric supercells.

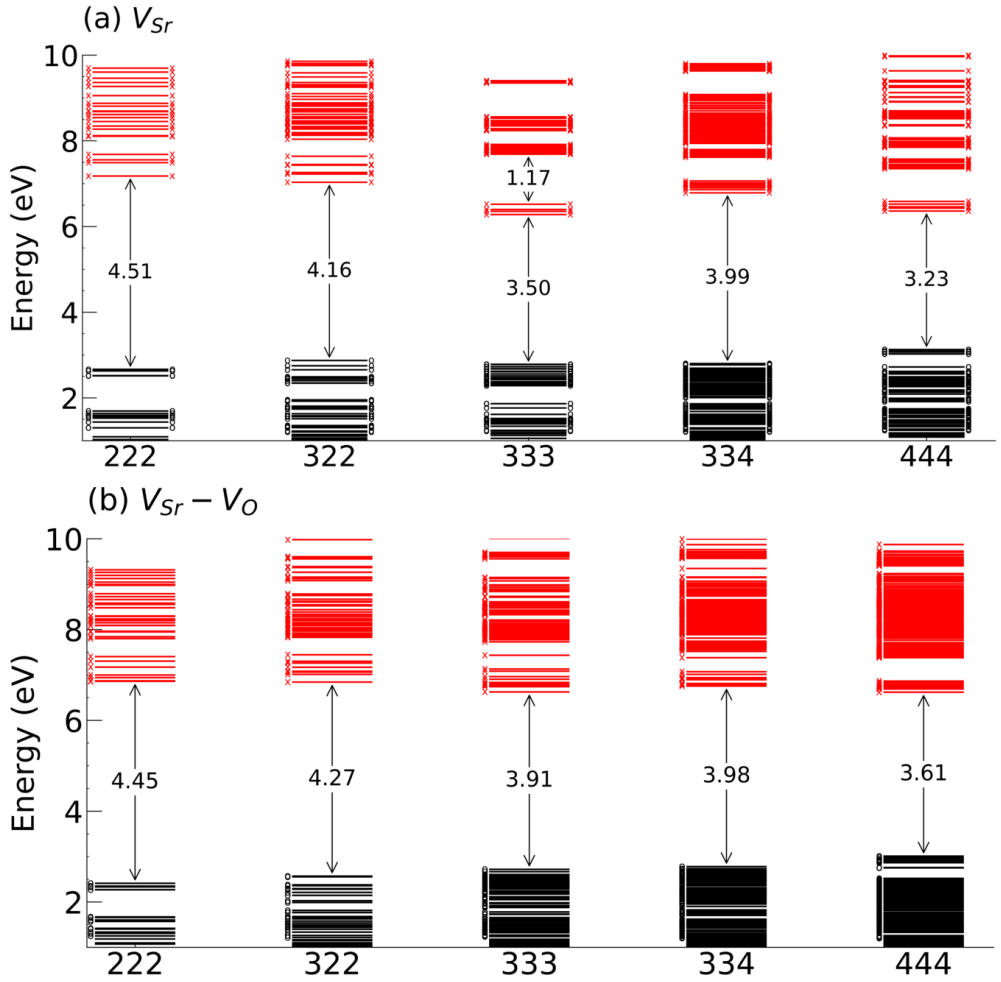

Figure 3.14: HSE06 predicted bands and charge densities at Γ for V_{Sr} (a) and V_{Sr}–V_O (b). Unoccupied orbitals are marked with red and with x. Occupied orbitals are marked in black and with o. Only the x-orientation is plotted for asymmetric supercells.

on the orientation of the vacancy in the x- or z- direction for asymmetric supercells, with E_g for 3 x 2 x 2 V_{Ox} predicted to be 0.03 eV narrower than V_{Oz} (Fig. S12‡). Notably, we do not observe any intra-bandgap states for V_O in any supercell that was reported by previous researchers.

3.3.6 Electronic Structure of A-Site defects

V_{Sr} also reveals large E_g widening that converges towards the bulk value in the largest supercells from 4.51 eV in 2 x 2 x 2 to 3.23 eV in 4 x 4 x 4. In both the HSE06 (Fig. 3.14a) calculated energy levels and full BLYP (Fig. S13‡) band structures, the 3 x 3 x 4 supercell predicts and unusually

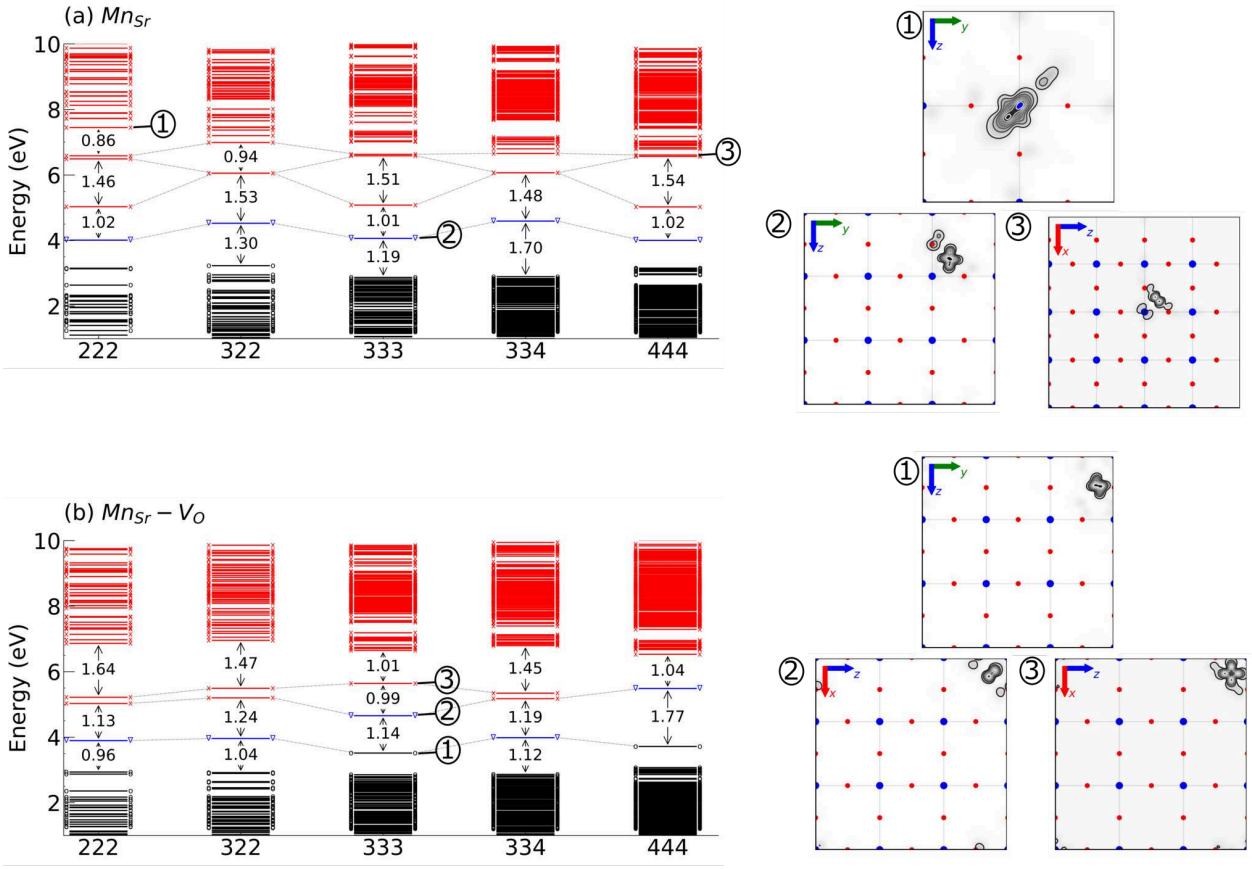

Figure 3.15: HSE06 predicted bands and charge densities at Γ for Mn_{Sr} (a) and $Mn_{Sr}-V_O$ (b). Unoccupied orbitals are marked with red and with x. Singly occupied orbitals are marked with blue and with ∇. Occupied orbitals are marked in black and with o. Gray lines trace the locations of localized orbitals with similar character. Only the x-orientation is plotted for asymmetric supercells. Charge density is summed along the perpendicular axis and indicated by shading and contour lines. The blue and red dots are a visual guide to indicate Ti and O lattice positions in the undefected supercell and do not represent the exact locations of atoms in the relaxed supercell.

large E_g, indicating that supercell symmetry is just as important in predicting electronic structure as size.

The corresponding double defect V_{Sr}–V_O causes little perturbation to the electronic structure, with the exception of 3 x 3 x 3 and 4 x 4 x 4 supercells. E_g in these supercells no longer approaches bulk value in both the BLYP (Fig. S13‡) and HSE06 (Fig. 3.14b) calculations. Interestingly, E_g in the asymmetric 3 x 2 x 2 supercells is sensitive to orientation of the defect with a difference in E_g of approximately 0.35 eV between V_{Sr}–V_{Ox} and V_{Sr}–V_{Oz} in the HSE06 predicted energy levels. This also may be a consequence of the Γ-only sampling in these calculations, in which Γ differs between an occupied and vacant O site depending on the x- or z- orientation of the defect. The significant loss of curvature in the 2 x 2 x 2 and 3 x 2 x 2 full BLYP band structures is indicative of the high structural distortion in these supercells, indicating a greater contribution from localized orbitals, opposed to the highly delocalized bands of supercells 3 x 3 x 3 and larger. The reduced atomic density in the small doubly-defected supercells may also help justify E_g widening.

Doping with the Mn ion has potential to create intra-bandgap defect states localized on the dopant atom, indicated in the full BLYP band structures as very flat bands, and confirmed by analysis of the HSE06 charge densities. In addition to potentially narrowing E_g, these localized orbitals can potentially act as trap states for excited charge carriers, as well as recombination centers. Considering the two different defect site geometries calculated for Mn_{Sr} (Fig. 3.9), it is intuitive to expect two different electronic structures that correspond to the 4-coordinate face-centered Mn complex of the asymmetric 3 x 2 x 2 and 3 x 3 x 4 supercells, and the 3-coordinate Mn complex of the cubic supercells. In the BLYP calculated band structures (Fig. S17‡), this is the case with the 3-coordinate complex resulting in an occupied defect band located in the middle of the band gap, and the 4-coordinate face centered Mn-complex predicted by the asymmetric supercells showing as a deeper defect state just above VB edge, with possible additional defect states comprising the edge of the CB coinciding with the fermi level (E_F).

The presence of these defect states is confirmed in the HSE06 calculations. In both defect

geometries, VBM is a singly occupied band located approximately 1 eV over the other occupied bands, and is localized on the dopant atom with t_{2g} character (② in Fig. 3.15a). In each geometry, there are three additional unoccupied Mn-localized orbitals, however with differing degeneracies. In the 3-coordinate Mn geometries, there is a non-degenerate deep defect state located approximately 1.5 eV below CBM. CBM in these geometries consist of two degenerate orbitals with charge density shared between Mn atom and nearby atoms (③ in Fig. 3.15a). Furthermore, exclusively the 2 x 2 x 2 supercell predicts an additional defect state with primarily d_{z^2} character (① in Fig. 3.15a), centered on the Ti atom nearest the dopant. In the face-centered 4-coordinate geometries, the two degenerate localized orbitals comprise a shallower defect state, approximately 0.94 eV or less below CBM. CBM in these geometries is a single localized orbital.

Considering the similar square planar geometry between the face-centered Mn_{Sr} geometries, and the 4-coordinate square planar Mn_{Sr}–V_O defect complexes predicted by 2 x 2 x 2, 3 x 2 x 2, and 3 x 3 x 4, it is unsurprising that the latter also predicts 3 total localized orbitals in the vicinity of the bandgap (Fig. 3.15b). However, all mid-gap states are much further (> 1 eV) below CB. There is little dependence on the orientation of the defect in asymmetric 3 x 2 x 2 and 3 x 3 x 4 supercells. The 5-coordinate Mn_{Sr}–V_O geometries of 3 x 3 x 3 and 4 x 4 x 4 predict critically different electronic structures. 3 x 3 x 3 continues to predict three localized orbitals, but the lowest of these is occupied in the VB (① in Fig. 3.15b). The 4 x 4 x 4 supercell also possess an occupied localized orbital, and the singly occupied Mn-localized VBM 1.77 eV above the remainder of the VB, and 1.04 eV below the CBM. Notably, 4 x 4 x 4 only predicts these two localized orbitals in the vicinity of the band gap, opposed to three localized states predicted by all other supercells. Combined ultraviolet photoelectron spectroscopy (UPS), inverse photoemission spectroscopy (IPES), and XPS spectra could provide relative energies of VB, CB, and Mn states that would allow some of these electronic structure to be ruled-out (or favored).

Doping with $Mn^{2+/3+}$ creates additional electronic structures (Fig. 3.16a & S14‡). In the five coordinate Mn complex predicted by both by $Mn_{Sr}{}^{2+}$ and $Mn_{Sr}{}^{3+}$ (Fig. S9‡), there are two

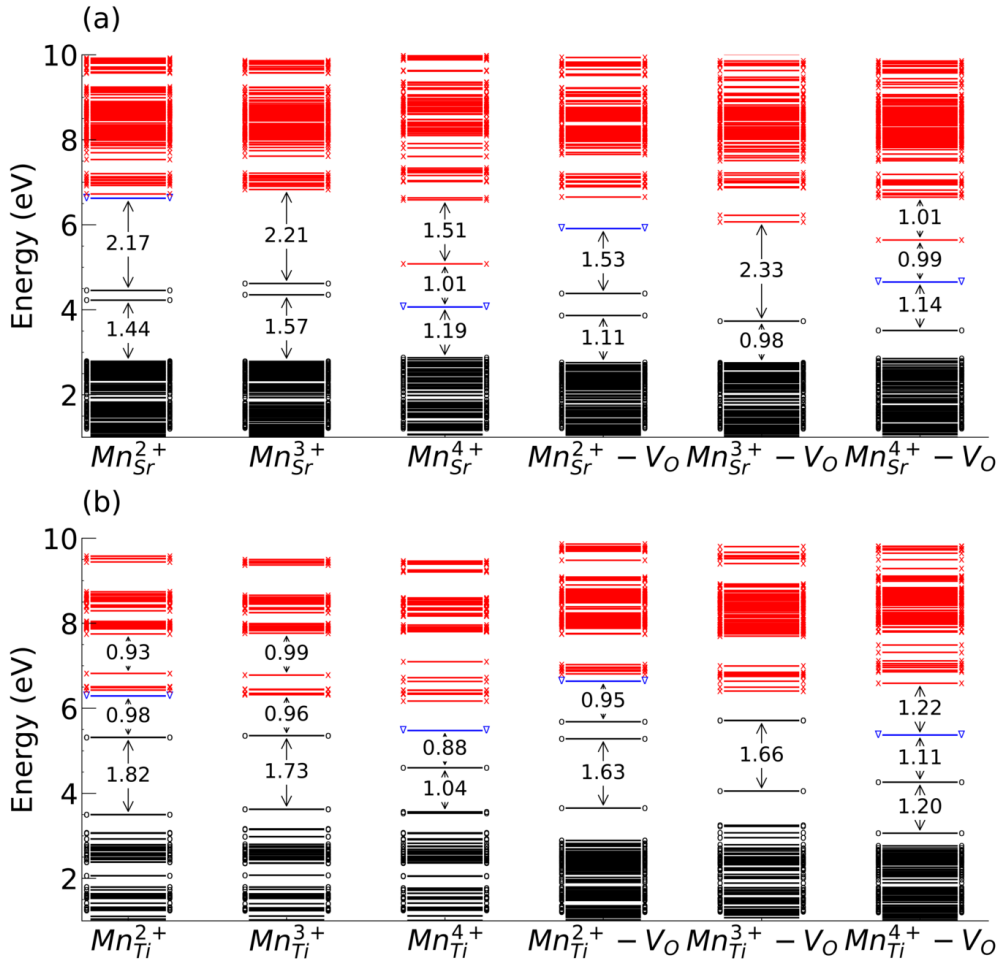

Figure 3.16: HSE06 predicted bands and charge densities at Γ in 3 x 3 x 3 supercell for $Mn^{2+/3+/4+}$ at the a-site (a) and b-site(b). Unoccupied orbitals are marked with red and with x. Singly occupied orbitals are marked with blue and with ∇. Occupied orbitals are marked in black and with o.

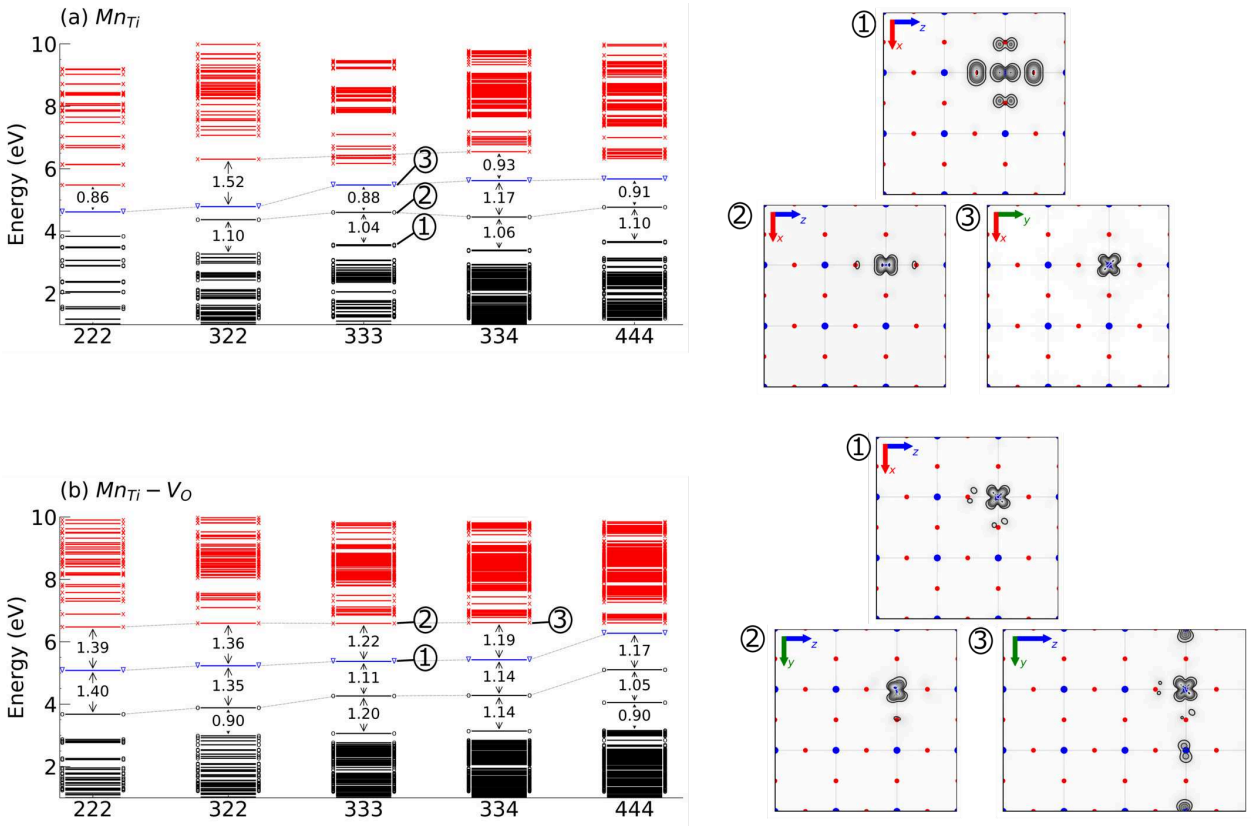

Figure 3.17: HSE06 predicted bands and charge densities at Γ for Mn_{Ti} (a) and Mn_{Ti}–V_O (b). Unoccupied orbitals are marked with red and with x. Singly occupied orbitals are marked with blue and with ∇. Occupied orbitals are marked in black and with o. Gray lines trace the locations of localized orbitals with similar character. Only the x-orientation is plotted for asymmetric supercells. Charge density is summed along the perpendicular axis and indicated by shading and contour lines. The blue and red dots are a visual guide to indicate Ti and O lattice positions in the undefected supercell and do not represent the exact locations of atoms in the relaxed supercell.

electronic states located approximately 1.5 eV above the remainder of the VB with splitting of approximately 0.1 eV. The higher of these orbitals is localized on the dopant, and constitutes VBM in Mn_{Sr}^{3+}, whereas the additional electron of Mn_{Sr}^{2+} singly occupies a delocalized orbital with Ti t_{2g} character, which is isoelectronic with the bottom of CB. The Mn_{Sr}^{3+}–V_O predicts a similar 5-coordinate geometry as the 2 x 2 x 2, 3 x 2 x 2, and 3 x 3 x 4 Mn_{Sr}^{4+}–V_O supercells, and the electronic structure is generally the same with the extra electron contributed by Mn^{3+} filling the previously singly occupied VB. Mn_{Sr}^{2+}–V_O also predicts a similar geometry, however the electronic structure is significantly different. In contrast to the other A-site defects, 4 localized states are predicted. In addition to those three with Mn t_{2g} character common in the other defects, the lowest of these occupied intrabandgap states located 1.11 eV above the rest of the VB has significant hybridization with with the nearby Ti d_{z^2} orbitals forming an F-center between the two adjacent Ti atoms.

3.3.7 Electronic Structure of B-Site defects

Single and double vacancies on the B-site generally also lead to large E_g (Fig. S15‡), like the A-site vacancies. Specifically, the V_{Ti} results in maximum E_g widening to 4.61 eV in the 2 x 2 x 2 and converges to the bulk value by the 4 x 4 x 4 supercell, with the biggest jump in convergence between 3 x 2 x 2 and 3 x 3 x 3 of approximately 0.78 eV in the HSE06 predicted structures. Full BLYP band structures (Fig. S16‡) also predict E_g widening in smallest supercells to 2.88 eV and 2.51 eV in 2 x 2 x 2 and 3 x 2 x 2 supercells, but full convergence to bulk value by the 3 x 3 x 3 supercell. The larger V_{Ti}–V_O defect results in smaller E_g widening to a HSE06 predicted maximum of 4.14 eV in the 2 x 2 x 2 supercell. However, this value is slower to converge, remaining fairly constant between 3.9 and 4.0 eV in all supercells, until only reaching the bulk value at the 4 x 4 x 4 in both BLYP and HSE06 calculations (Fig. S15‡). Unexpectedly, both functionals calculate the 3 x 3 x 3 supercell to have a larger E_g than its asymmetric neighbors.

The Mn_{Ti} defect shows high sensitivity to supercell size. The smallest E_g occurs for the 2 x 2 x 2 supercell, predicting metallic behavior with ΔE = 0.86 eV between the between the singly

occupied VBM and CBM. This feature is unique to the HSE06 predicted bands with the full BLYP band structures (Fig. S16‡) indicating E_g=1.53 eV, yet E_F is localized in the CB. Analysis of the charge density indicates that the singly occupied VBM and next highest band are located entirely on the Mn ion (② and ③ in Fig. 3.17a). The CBM largely retains this character, albeit with significant O *2p* contributions. Only in the asymmetric supercells is CBM is completely localized on Mn with t_{2g} character. In supercells 3 x 3 x 3 and larger, there is the appearance of an additional localized state not centered on the Mn ion, but rather on the O *2p* orbitals surrounding the dopant (① in Fig. 3.17a). This state occurs for several bands immediately below the singly occupied VBM, and cannot occur in supercells 3 x 3 x 3 or smaller due to the majority of atoms in small supercells being defect adjacent. The 3 x 2 x 2 and 3 x 3 x 4 supercells both predict larger E_g, consistent with the increased Ti-O bond lengths for asymmetric supercells (Fig. 3.1d) and thus poorer orbital overlap. The full BLYP bandstructures also produce highly variable results. In each case, E_g is decreased from the bulk value, and E_F is localized in the CB.

Doping with $Mn^{2+/3+}$ causes minimal change in the predicted geometry of each Mn_{Ti} supercell, however varying electronic structures are predicted (Fig. 3.16b). The HSE06 calculations predict that VBM in Mn_{Ti}^{3+} becomes two doubly occupied bands degenerate at Γ. Both of these states have Mn t_{2g}-like character, and one of them shares significant charge density with the surrounding O *2p* orbitals. These are approximately 1.73 eV higher than the remainder of VB, and 0.96 eV below the conduction band edge. This band alignment is nearly identical in the Mn_{Ti}^{2+} defect, with the extra electron residing in the delocalized CBM with Ti t_{2g} character. The BLYP predicted band structures do not capture these subtle changes, and deviation from the 3 x 3 x 3 Mn_{Ti}^{4+} band structure is marginal (Fig. S14‡).

In Mn_{Ti}–V_O supercells, most supercells retain three localized Mn orbitals (① and ② in Fig. 3.15b), comprising VBM, CBM, and a singly occupied mid-gap state. However, as supercell size is increased, the localized orbital comprising CBM begins to delocalize among the nearby Ti atoms in plane with the dopant (③ in Fig. 3.17b), and is completely delocalized by the 4 x 4 x 4

supercell. Surprisingly, there is a significant difference in the electronic structures between the 3 x 3 x 4 Mn_{Ti}-V_{Ox} and 3 x 3 x 4 Mn_{Ti}-V_{Oz} supercells (Fig. S17‡) with the location of the singly-occupied VBM. Although the same character is retained in both cases, the singly occpuied VBM of Mn_{Ti}-V_{Oz} is blueshifted to the CBM compared to the mid-gap location of Mn_{Ti}-V_{Ox}.

The full BLYP bandstructures (Fig. S16‡) are generally consistent across all supercells, and align well with the HSE06 structures. Notably, both methods predict a significantly large E_g compared with Mn_{Ti}. Doping with Mn^{3+} produces two degenerate doubly occupied VBM (Fig. 3.16b) approximately 1.66 eV above the remainder of the valence band and 0.6 eV below CBM. Both of these states are localized on the Mn dopant. In the Mn_{Ti}^{2+}-V_O, the degeneracy of these two states is broken and they are separated by approximately 0.2 eV. The extra electron resides at the bottom of CB in a singly occupied localized Mn orbital. For the $Mn^{2+/3+}$ defects, the full BLYP bandstructures do not produce significant differences (Fig. S14‡), other than slightly different E_g of 1.84 eV and 2.01 eV for Mn^{3+} and Mn^{2+} respectively.

3.4 Conclusion

We performed the first comprehensive study of the profound impact of supercell size and model parameters on calculated properties of $SrTiO_3$ point defects. Our analysis of cell-wide geometry and energetics suggest that the 3 x 3 x 3 supercell represents the greatest compromise between computational cost and minimization of computational artifacts. In general, all single and double vacancies widen the band gap and Mn dopants result in narrower band gaps or singly occupied defect states in the undoped gap.

However, a more detailed exploration of defect site geometries and electronic structure reveals high variability and differing properties even among the largest supercells studied here, demonstrating the importance of such benchmarking studies or exploration of a variety of structures for each defect. While targeted experiments to determine the structure (PDF) and electronic structure (XPS, UPS, IEPS) of a typical Mn dopant would help add to the understand-

ing of Mn-doped $SrTiO_3$, methods that can identify the lowest energy geometries irrespective of supercell size would limit the computational cost to such studies. Ultimately, our results indicate that both supercell size and shape should be explored to capture the range of substitution dopants and vacancies when the atoms have more degrees of freedom (like the V_{Sr}, Mn_{Sr}, $Mn_{Sr}-V_O$).

Furthermore, our calculations using Mn^{2+} and Mn^{3+} suggest the need to explore model parameter space in additional dimensions in order to gain a complete understand of the complex chemistry of Mn-doped $SrTiO_3$. Importantly the interesting gap states predicted for the $Mn_{Sr}{}^{4+}$ and $Mn_{Sr}{}^{4+}-V_O$ suggest that $Mn_{Sr}{}^{4+}$ as opposed to $Mn_{Sr}{}^{2+}$ doped structure should have interesting functionality.

Chapter 4

Hyperfine models for the Mn dopant in $SrTiO_3$[†,‡]

Perovskites with the general composition ABO_3 are some of the most promising materials for a new generation of semiconductor devices. Much of this technological interest is due to their high dielectric constant and large charge storage capacity [66, 67]. Importantly, the properties of these materials are tunable as a function of simple geometric changes of the crystal lattice [68, 69]. Accordingly, ***ab initio*** methods have recently provided much insight into the structure-property relationship of a variety of perovskite structural modifications, including vacancies [35, 70], dopants [48, 71], and surfaces [72, 73]. Continuing to catalogue the wide ensemble of possible defect structures and their consequence on material properties is important to both untangle measured experimental properties, which are often an average of multiple structures, as well as to predict what material geometries are desirable for particular applications.

Among perovskites, $SrTiO_3$ is highly studied because similar size of the A- and B-site cations allows for the inclusion of redox active dopants, such as $Mn^{2+/3+/4+}$, at either cationic site [44]. Furthermore, doping with paramagnetic species introduces additional functionalities that further extend the scientific interest in $SrTiO_3$ for a variety of new applications, such as spin-based quantum information systems [74, 75]. Due to these exciting possibilities, significant research efforts have focused on characterizing the nature of Mn-doping in $SrTiO_3$ [27, 66, 76]. For such studies, electron paramagnetic resonance (EPR) spectroscopy has proven a powerful

[†]Reproduced from Repa, G.M.; Fredin, L.A. Mn environment in doped $SrTiO_3$ revealed by first-principles calculation of hyperfine splittings. *Applied Physics Letters* **2022**, 121(2), 022401., with the permission of AIP Publishing.

[‡]Electronic supplementary information is available at https://doi.org/10.1063/5.0096788.

tool to provide information on the location, spin-state, and coordination number of the dopant [47, 63, 77–79]. The relevant parameter derived from EPR spectra is the termed hyperfine splitting (**A**) of otherwise degenerate electronic levels, which arises from interaction between the nuclear magnetic moment of the Mn atom, and magnetic moment of the electrons. The magnitude of such splitting is directly influenced by distortions of the charge distribution around the dopant induced by varying ligand fields. Thus, the magnitude of the hyperfine splitting can can be indicative of specific doping sites.

Following Kröger-Vink notation, we denote these different doping sites as Mn_x where X = Ti or Sr depending on the substituted ion. The superscripts x , ', and • denote a net neutral (e.g., $Ti^{4+} \rightarrow Mn^{4+}$, $Sr^{2+} \rightarrow Mn^{2+}$), negative ($Ti^{4+} \rightarrow Mn^{2+}$), and positive charge ($Sr^{2+} \rightarrow Mn^{4+}$) when compared to the defect-free host respectively. While the EPR signals for Mn_{Ti}", Mn_{Ti}^{x}, and Mn_{Sr}^{x} have been well-established, it is unlikely that these complexes represent the entire range of Mn dopants that exist in the real material. With this study, we aim to demonstrate the feasibility of calculating transition metal dopant EPR parameters in a complex oxide material to not only assign previously observed EPR peaks to exact geometries, but to also predict the EPR parameters of defects that may exist, but have not yet been assigned peaks in experimental spectra.

To accomplish this, we calculate **A** of the Mn dopant in various potential defect geometries and locations (Fig. 4.1) [8]. The only stable nucleus of Mn is Mn-55 with nuclear spin I=5/2. These calculated values can be directly compared with those obtained from experimental reports. Therefore, the hyperfine splitting of each of the candidate dopant geometries can be used to identify the frequency that structure has been observed in experiment. Similar first-principles calculation of the hyperfine splitting has been used to gain insight into main group elements [80–82], but its success for transition metals has only been demonstrated more recently [83]. All calculations in the present study were performed using density functional theory (DFT) and the electron projector-augmented wave (PAW) scheme [84] as implemented in the Vienna Ab Initio Simulation Package (VASP) [57] with a 600 eV planewave cutoff and Γ-point sam-

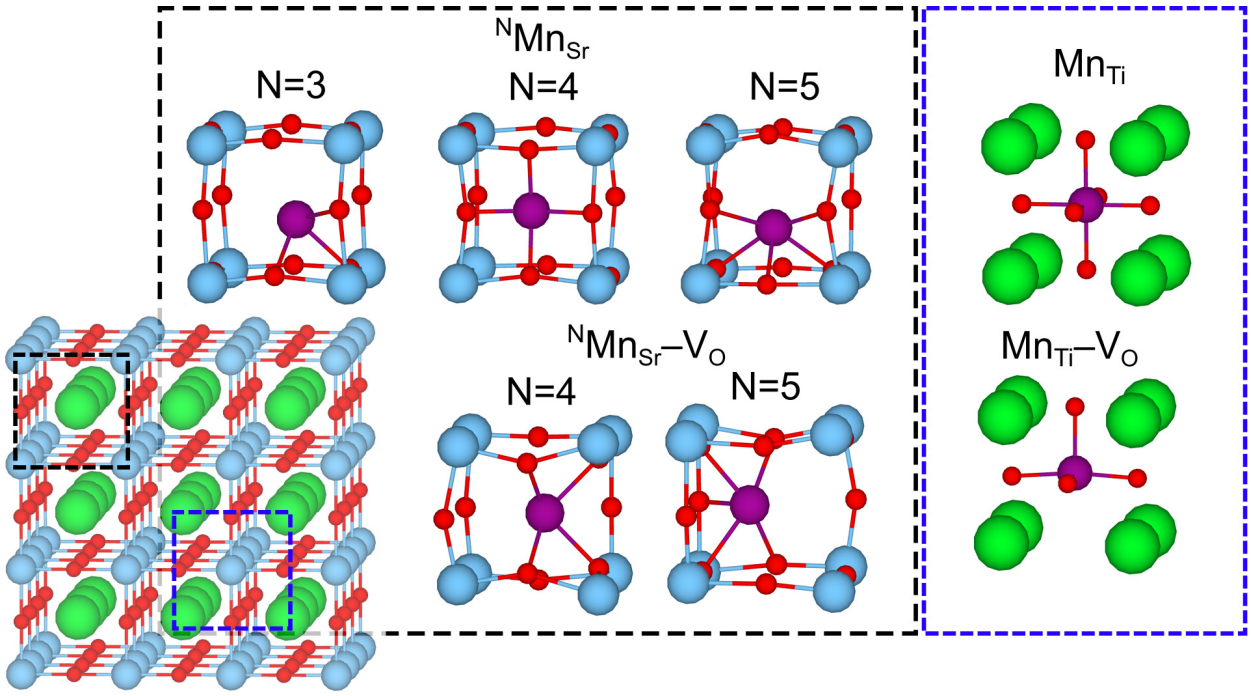

Figure 4.1: Representative geometries of the different dopants studied here and the 3 x 3 x 3 supercell used for all calculations. The following color code is adopted for this and proceeding figures: Mn = purple, Sr = green, Ti = blue, O = red.

pling. The following core/valence configurations were used for each element: Sr:[Ar]3d/4s4p5s, Ti:[Ne]/3s3p4s3d, O:[He]/2s2p,Mn:[Ne]/3s3p4s3d.

Each geometry was fully optimized in a 135-atom 3 x 3 x 3 supercell (Fig. 4.1) using the PBE functional [85] with no on-site Coulomb corrections, while calculation of electronic properties and hyperfine parameters used HSE06 [7] (with modified Fock exchange ratio and screening parameter where noted). It is important to note that simple GGA functionals underestimate the band gap in perovskite materials. However, the use of hybrid exchange-correlation functionals like B3PW, B3LYP, or HSE06 have been shown to improve agreement with experimental values [48, 73, 86]. Each optimization was performed with collinear spin-polarization neglecting the effects of spin-orbit coupling, with the magnetic moment of Mn initialized to 3 or 5 μ_B for Mn^{4+} and Mn^{2+} respectively, which corresponds to the experimentally observed spin state of the dopant. In general, the HSE06 calculations were initialized from the charge density of the preceding PBE optimization, but we found no change in the results if the charge density is

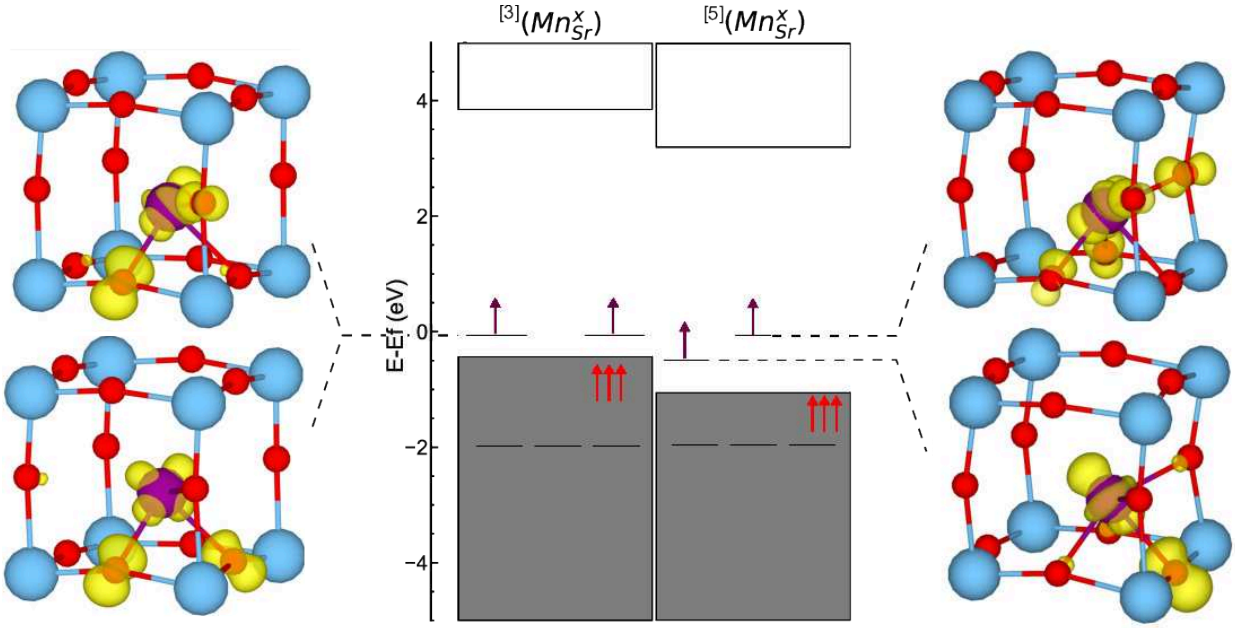

Figure 4.2: Orbital structures and localized orbital densities for most favorable $Mn_{Sr}{}^{x}$defects. Purple arrows represent occupied electronic states with significant metal-mixing. Red arrows in the valence band correspond to delocalized unpaired electrons.

initialized from scratch with the magnetic moment for Mn = 3 or 5 μ_B. The effects of core polarization on the hyperfine parameter were included through the method proposed in refs [87] and [88], and the nuclear gyromagnetic ratio for Mn was set to γ = 10.500 MHz.

Of the previously identified dopant geometries, Sr-site dopants have shown the greatest geometric variation. Among these, $Mn_{Sr}{}^{x}$ has been the most well-studied, and thus represents an ideal test case for calculation of the hyperfine splitting. Each of the three candidate $Mn_{Sr}{}^{x}$ geometries is distinguishable by the coordination number of the dopant, and are henceforth referred to as $^{[N]}Mn_{Sr}{}^{x}$, where N = 3-, 4-, 5-coordinated. Calculated energies show that $^{[3]}Mn_{Sr}{}^{x}$ and $^{[5]}Mn_{Sr}{}^{x}$ are the most thermodynamically favored geometries (Fig. S1‡). These each are separated by ≈ 0.2 eV, with $^{[5]}Mn_{Sr}{}^{x}$ the lowest energy structure. $^{[4]}Mn_{Sr}{}^{x}$ is less favored by ≈ 1.3 eV. While it is well-established that the size mismatch between Sr and Mn allows for fast ionic motion of the dopant atom between lattice positions [63], the energetics indicate that Mn hopping on the A-site may primarily occur between the 3- and 5-coordinate geometries. Further insight into which geometries have been most commonly measured in experiment is obtained

Table 4.1: Structural parameters of calculated and experimental Mn_{Sr}^{x}defects. Parenthesis represents the number of atoms fit in the coordination sphere, followed by the averaged distance among those atoms.

	Ref [48]	Ref [78]	Ref [76]	$^{[3]}Mn_{Sr}^{x}$	$^{[4]}Mn_{Sr}^{x}$	$^{[5]}Mn_{Sr}^{x}$
	(N)Å					
Mn–O	(4)2.12	(2)1.90	(6)2.17	(3)2.10	(4)1.91	(5)2.18
	(4)2.75	(3)2.18		(6)2.92	(4)3.24	(2)3.14
	(4)3.35	(6)3.04		(3) 3.49	(4)3.73	(4)3.39
Mn–Ti	(4)3.1	(4)3.06	(4)3.005	(1)2.89	(4)2.97	(2)2.92
Mn–Ti	(4)3.57	(4)3.06	(4)3.875	(3)3.28	(4)4.16	(4)3.45
Mn–Ti				(3)3.61		
Mn–Sr	(2)3.54	(1)3.02	(1)3.16	(3)3.65	(1)3.04	(2)3.5
Mn–Sr	(4)4.3		(4)3.69	(3)4.29	(4)4.12	(4)4.23

by comparing our calculated structures to available EXAFS data.

Table 4.1 shows that both $^{[3]}Mn_{Sr}^{x}$ and $^{[5]}Mn_{Sr}^{x}$ produce particularly good agreement with experimental reports. Specifically, the first Mn–O coordination sphere of $^{[3]}Mn_{Sr}^{x}$ aligns well with the experimental structure reported by reference [48], while the same coordination sphere of $^{[5]}Mn_{Sr}^{x}$ is congruent to that reported by reference [76]. Interestingly, the structure reported by reference [78] agrees best with the high-energy $^{[4]}Mn_{Sr}^{x}$ geometry, including the first Mn–O coordination sphere at ≈ 1.90 Å, as well as single Mn–Sr distance of ≈ 3.02 Å. While the number of atoms included in each coordination sphere for the DFT values of Table 4.1 were determined by natural grouping of calculated distances, better or worse agreement with experimental data can be obtained by alternate fits or exactly matching those utilized in the experimental data. This indicates that EXAFS measurements alone are insufficient for commenting on the quality of a DFT-derived structure.

While the EXAFS data indicate all three Mn_{Sr}^{x} geometries have occurred in experimental studies, it is notable that the same degree of variance is not reflected in the experimental hyperfine splittings (Table 4.2). This indicates that calculation of these values can be used to fingerprint each candidate Mn_{Sr}^{x} geometry, and allow us to hone in on the most probable defect geometries. Considering the aforementioned ionic hopping of the dopant atom, any anisotropic

contributions to the hyperfine splitting are averaged when reporting **A** for Sr-site defects.

Table 4.2 confirms that experimental values for Mn_{Sr}^{x} show little variation ranging from **A** = 246 to 249 MHz. Interestingly, HSE06 predicts values of **A** = 266, 159, and 244 MHz for $^{[3]}Mn_{Sr}^{x}$, $^{[4]}Mn_{Sr}^{x}$ and $^{[5]}Mn_{Sr}^{x}$ respectively. The excellent agreement of two of these three values, as well as the thermodynamics discussed above, further suggests that the outlying $^{[4]}Mn_{Sr}^{x}$ is likely not the dominant defect geometry that has been studied in experiment thus far. The agreement of the hyperfine splitting for the remaining two Mn_{Sr}^{x} geometries can be further improved by considering the multiple energetic minima on the potential energy surface. For each Sr substitution, there are 12 equivalent Mn positions that result in $^{[5]}Mn_{Sr}^{x}$ and 8 equivalent positions that result in $^{[3]}Mn_{Sr}^{x}$. The weighted hyperfine splitting with this consideration is **A** $\approx$ 253 MHz, and if factoring in the previously discussed 0.2 eV difference between the two structures, excellent agreement with experimental results would be achieved. Importantly, the accuracy of these results allow this model to be extended to predict structure and splitting for defects that have yet to be directly measured in experiment.

Mn^{4+} dopants in $SrTiO_3$ have previously been exclusively associated with Ti site substitution, and to our knowledge $Mn_{Sr}^{\bullet\bullet}$ has yet be observed by any experimental method. However, it is well-established that reversible control of the Mn dopant oxidation state is possible [47], and thus aliovalent A-site substitution of Mn dopants cannot be ruled out. The $Mn_{Sr}^{\bullet\bullet}$ energy of each of the previously discussed 3- to 5-coordinated geometries were also calculated, and it was found that $^{[5]}Mn_{Sr}^{\bullet\bullet}$ is the most energetically favorable at 0.82 and 1.28 eV below $^{[4]}Mn_{Sr}^{\bullet\bullet}$ and $^{[3]}Mn_{Sr}^{\bullet\bullet}$ respectively (Fig. S1‡). The preference for higher coordination is expected from an electron-deficient dopant, and if $Mn_{Sr}^{\bullet\bullet}$ does in fact occur in $SrTiO_3$, it likely does so in the 5-coordinate geometry. The hyperfine splitting for such a structure is predicted to be **A**=228 MHz.

In addition to Mn_{Sr} defects, we considered A-site substitution with $Mn^{2+/4+}$ and adjacent oxygen vacancy (Mn_{Sr}–V_O), which have been reported for other metal-dopants in $SrTiO_3$ [44]. We considered two different geometries where the dopant ion either fills the O atom vacancy

Table 4.2: **A**from experimental references. (MHz)

Ref	Mn_{Sr}^{x}	Mn_{Ti}^{x}	Mn_{Ti}"	$(Mn_{Ti}"-V_O)^x$
[45]	246	210	237	
[48]	247	214	237	203
[89]		208		
[90]			247	
[63]	248	214		
[91]	247	217		
[92]			248	228
[79]	247	214		

to form a 4-coordinate defect complex ($^{[4]}(Mn_{Sr}^{x}-V_O)^{\bullet\bullet}$), or is positioned directly away from the vacancy creating a 5-coordinate defect complex ($^{[5]}(Mn_{Sr}^{x}-V_O)^{\bullet\bullet}$). In the case of Mn^{2+}, these two structures are approximately energetically equivalent (separated by 0.2 eV). Hyperfine splitting for each of these geometries are **A** = 231 and 249 MHz for $^{[4]}(Mn_{Sr}^{x}-V_O)^{\bullet\bullet}$ and $^{[5]}(Mn_{Sr}^{x}-V_O)^{\bullet\bullet}$ respectively. For $(Mn_{Sr}^{\bullet\bullet}-V_O)^{\bullet\bullet\bullet\bullet}$, we find that the 5-coordinate configuration is the most stable by 1.04 eV with **A** = 230 MHz.

Each of these most favorable Sr-site dopants display similar electronic structures, with representative band structures for Mn_{Sr}^{x} shown in Fig. 4.2 (band structures for each defect are available in the SI‡). In each case, the three lower lying Mn *d* orbitals are located deep in the valence band. Three unpaired electrons of d^3 Mn^{4+} and d^5 Mn^{2+} are thus liberated from the dopant and float to the top of the valence band in delocalized O *p* orbitals. In the case of Mn^{2+} dopants, the remaining two unpaired electrons reside in localized deep defect states in the bandgap contributed by the hybridization of the Mn *d* and O *p* orbitals (Fig. 4.2).

Such transfer of dopant electrons to or from the host lattice may be critical for the conductive properties of the material. To probe the nature of donor/acceptor behavior of the Mn dopant, we performed a Bader charge analysis [93] of each defect. Table SI‡presents these charges tabulated as the number of electrons gained or lost by the dopant or lattice compared to the pure material. For Sr-site defects, doping with isovalent Mn^{2+} should result in nominal net change in the lattice, and is indeed confirmed by the calculated Bader charges. $Mn_{Sr}^{\bullet\bullet}$ displays significant acceptor-like behavior withdrawing two electrons from the lattice. This behavior

confirms that Sr-site doping of Mn^{4+} may be an effective way to increase the n-type character of $SrTiO_3$. For Mn_{Sr}–V_O defects, the charge analysis shows electron transfer nature of Mn^{2+} and Mn^{4+} are unaffected by the adjacent oxygen vacancy compared to Mn_{Sr} defects.

In the case of Mn_{Ti} defects, Ti-substitution with isovalent Mn^{4+} should result in the charge-neutral complex. However, the Bader charge calculations indicate that Mn_{Ti}^{x} continues to withdraw ≈ 2 electrons from the lattice to satisfy the highly stable d^5 configuration. This withdrawing behavior is a critical observation that even isovalent doping of Mn^{4+} displays acceptor behavior, while Mn_{Ti}" is the non-charge transfer defect.

Although these B-site dopants are geometrically simpler, highly covalent bonding with the host lattice means these structures are critical for the electronic properties of the material. It is widely believed that Mn^{4+} and Mn^{2+} load into the Ti-site with high-spin electron configurations S = 3/2 and 5/2, respectively [45, 89, 91, 92]. For Mn_{Ti}^{x}, the calculated EXAFS parameters (Table S2‡) indicate no significant lattice distortion around the dopant, in agreement with experimentally obtained values. In fact, our calculations indicate only the high-spin Mn_{Ti}" results in expansion of the surrounding Mn–O bonds, consistent with the larger atomic radii of the dopant. However, experimental observation of this lattice distortion has been sparse, and the majority of structural data reported is for Mn_{Ti}^{x}. Prior to discussing the geometry and hyperfine parameters for these dopants, it is necessary to comment on the accuracy of HSE06 in capturing the chemistry of these complex defects. Due to the high sensitivity of the hyperfine splitting to the charge density, all subsequent calculations of **A** were performed on a very dense FFT grid.

In an unconstrained optimization of Mn_{Ti}", HSE06 predicts large splitting of the Mn *d* orbitals to above the conduction band edge (Fig. 4.3). This releases the unpaired electron into the delocalized Ti t_{2g} orbitals where it is polarized against the Mn *d* orbitals. The resulting Jahn-Teller distortion shifts each TiO_6 octahedral center in the [111] direction. Such a configuration is predicted to be 1.46 eV more stable than the low-spin S = 1/2, and 2.88 eV more stable than the high-spin S = 5/2 Mn^{2+}, which is regarded to be the majority Mn_{Ti}" dopant. For S = 5/2 Mn_{Ti}",

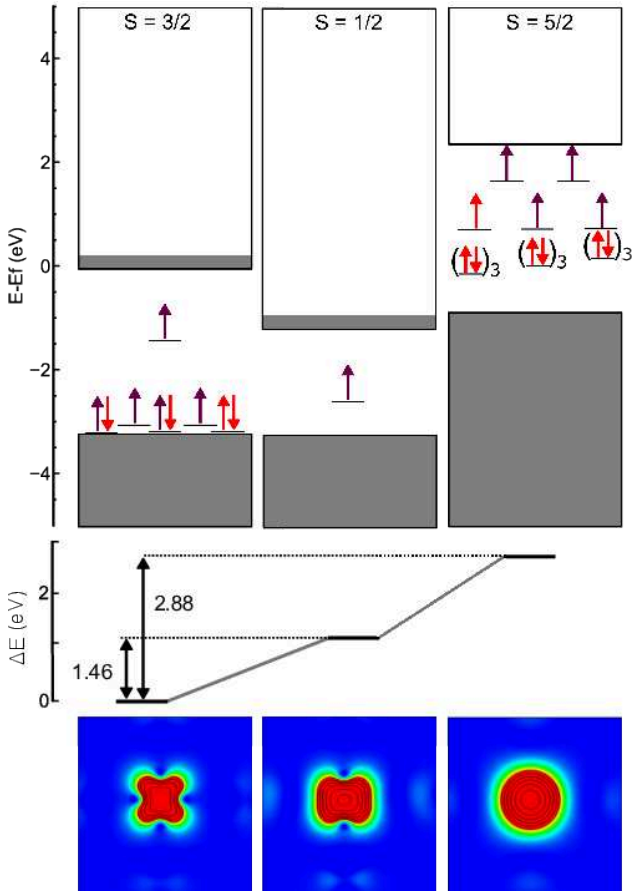

Figure 4.3: Top Panel: Band structures and localized defect states for Mn_{Ti}" defects. Metal mixed orbitals are shown with a purple arrow, while a red arrow indicates ligand centered orbital. Gray shading corresponds to electron occupation. Middle Panel: Difference in thermodynamic stability for various dopant spin states. Bottom Panel: Spin density of dopant ion and adjacent oxygen atoms

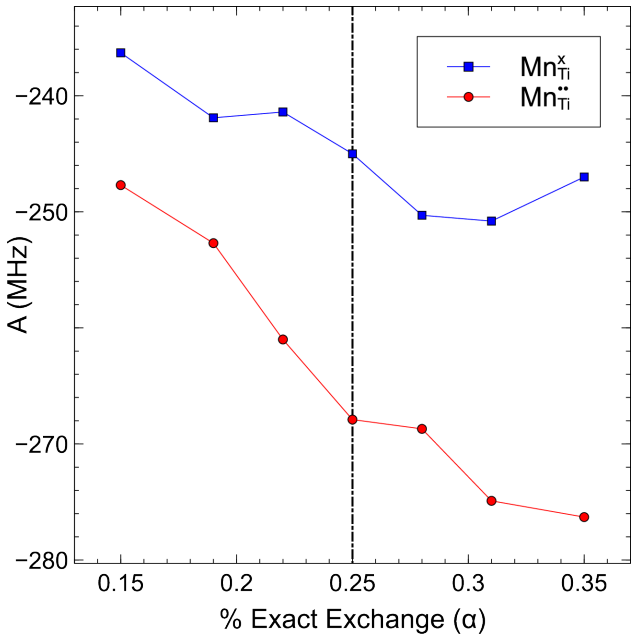

Figure 4.4: Hyperfine splittings of high-spin Mn_{Ti} defects as a function of exact exchange percent. The black vertical line represents α for HSE06.

there are a number of ligand-centered bonding orbitals in the band gap in addition to the five Mn *d* orbitals. The unexpected energetic ordering of these electron configurations is attributed to short comings of the HSE06 functional for studying dopants in perovskites [94].

It has been well-documented that range-separated hybrid functionals, such as HSE06, can produce spurious results when there is a coexistence of localized atomic orbitals and delocalized bands [94]. Such artifacts arise from equal screening and mixing of the two different electronic states, which can result in an incomplete cancellation of the self-interaction error of the dopant orbitals [95]. Indeed, there are indications of such issues in the S = 3/2 Mn_{Ti}" calculation, where an unusually large contribution from the Hartree (electron-electron) Energy results in a lower predicted energy compared to the experimentally favorable S = 5/2 Mn_{Ti}". Furthermore, similar erroneous electronic structures of transition metal dopants in other oxides have been identified [96]. Such issues are not to be expected for Sr-substituting dopants, as electrons are less likely highly-correlated due to the ionic nature of the A-site.

Despite being able to obtain the correct spin state of the Mn ion through constraint of the net magnetic moment of the supercell, issues related to an unphysical representation of the

Table 4.3: Calculated hyperfine parameters for selected defects. The hyperfine parameters for all defects studied here can be found in the Supplemental Information.

Sr-Site	**A**(MHz)	Ti-Site	**A**(MHz)	
$^{[5]}Mn_{Sr}^{x}$	244	Mn_{Ti}"	248	α=0.15
$^{[5]}Mn_{Sr}^{\bullet\bullet}$	228	Mn_{Ti}^{x}	236	α=0.15
$^{[5]}(Mn_{Sr}^{x}-V_O)^{\bullet\bullet}$	249			
$^{[5]}(Mn_{Sr}^{\bullet\bullet}-V_O)^{\bullet\bullet\bullet\bullet}$	230			

electronic structure also show up in the calculation of the hyperfine splitting. For the high-spin Mn_{Ti}" and Mn_{Ti}^{x}, hyperfine splittings are calculated to be **A** = 268 and 245 MHz respectively. While these values capture the experimental trend reasonably well, they also overshoot the experimental values by ≈20-30 MHz each. Several strategies have been proposed to circumvent the issues relating to use of a range separated hybrid functional to study localized dopant orbitals in materials [94–96]. Here, we opt to simply vary the ratio of Fock exchange (α) and screening parameter (μ) to gain insight into which changes lead to an improved hyperfine splitting. In the case of the latter, we find little to no effect on the calculated hyperfine splittings (Fig. S2) and thus focus the remainder of the discussion on the former.

Generally, as the α is decreased from the HSE06 standard of α = 0.25, greater agreement with the experimental hyperfine splitting is achieved, varying from **A** = 248 MHz for Mn_{Ti}" with α = 0.15 to **A** = 276 MHz with α = 0.35. At these reduced α values, the high-spin Mn is correctly predicted as the lowest energy configuration, confirming that the unique electronic structure predicted by standard HSE06 is purely a consequence of functional design. While systematic optimization of these parameters are beyond the scope this work, future studies could benchmark different functionals or optimize the parameters of HSE06 to provide more reliable ***ab initio*** calculation of B-site substitution of Mn, and likely most transition metal dopants, in perovskites.

However, the results presented here demonstrate that when the electronic properties of a dopant are accurately captured, such as the case of Mn_{Sr} defects, further calculation of the hyperfine splitting can lead to deeper insights than those afforded by traditional DFT analysis. We demonstrated this for Mn_{Sr}^{x} substitutions where energetic and structural comparisons alone

were unable to unambiguously identify $^{[5]}Mn_{Sr}^{x}$ as the most frequently observed Mn_{Sr} geometry in experiment. In addition to serving as a geometric fingerprint, the hyperfine parameter can yield important insights into the spin density around a particular dopant, and provide an alternative or supplement to traditional charge partitioning schemes. Perhaps most critically, the feasibility of ***ab initio*** calculation of EPR parameters for defects that have yet to be assigned peaks can aid interpretation of experimental spectra, which has traditionally relied on fitting to phenomenological models. While prediction of hyperfine splittings for $(Mn_{Ti}''–V_O)^{x}$ and $(Mn_{Ti}^{x}–V_O)^{\bullet\bullet}$ weren't possible in the current work due to functional limitations, our reported hyperfine splittings for $Mn_{Sr}^{\bullet\bullet}$ and $Mn_{Sr}–V_O$ defects provide signatures to look for in future EPR studies.

Chapter 5

Oxygen diffusion in doped $SrTiO_3$

5.1 Introduction

The perovskite family of ceramic oxides represents some of the most widely used oxide materials today. Comprising the chemical formula ABO_3 and characterized by a network of corner-sharing BO_6 octahedra around A-site cations, perovskite oxides are being targeted for the next generation of solid state batteries [97], fuel cells [98], thermoelectrics [99], photovoltaics [100], and capacitors [101]. A large portion of this technological interest stems from the tolerance of the perovskite structure to accommodate a variety of different elements, allowing high tunabilty through elemental composition [102] or doping [100]. $SrTiO_3$ is an archetype perovskite oxide, serving as an ideal model system for understanding the properties of the larger family. Furthermore, $SrTiO_3$ has wide commercial use as a substrate for epitaxial growth, and thus serves as the bottom electrode for many oxide thin-film electronic devices [103]. In other applications, the high dielectric constant of $SrTiO_3$ makes it a valuable material for transistors and capacitors [101], and its electrical properties make it an appealing electrode for ionic conductors [104].

The emergence of $SrTiO_3$ in a variety of device architectures has resulted in increased attention to underlying defects of the crystal lattice, which often are the critical determinants of performance [100]. Arguably, the most important of these defects that arise during material processing are oxygen vacancies (V_O) and their subsequent long range diffusion [105]. Indeed, this

ionic diffusion may be the source of electronic device aging, giving rise to fatigue [106] and resistance degradation [107], ultimately acting as a source of failure. Conversely, some applications may actually seek to maximize the rate of diffusion of charged vacancies, resulting in improved energy fuel cells [104]. Thus, significant research effort has been focused on understanding the distribution and kinetics of V_O migration in perovskites under working conditions.

The migration path for V_O diffusion is well-established, and involves an oxygen atom traveling along a TiO_6 octahedral edge [105] (Fig. S1[‡]). However, the energetic barrier (E_a) reported for this process experimentally has ranged widely from 0.3 [108] to 2.1 eV [109], with some consensus that the barrier is around 0.6 eV [110]. Computer simulations of the event have also produced varying results with density functional theory (DFT) producing barriers ranging from 0.27 [31] to 0.7 eV [111], and classical inter-atomic potential models (MD) predicting barriers from 0.42 [112] to 1.35 eV [113].

While the exact energetics of the V_O migration mechanism in undoped $SrTiO_3$ remains to be established, it has been widely believed that the ionic diffusion rate (D) can be altered by dopants [114], such as Cr, Mn, and Fe. Indeed, these acceptor dopants are a source of oxygen vacancies during the synthesis process through the maintenance of charge neutrality [115]. Therefore, intentional doping can be seen as a design strategy to increase V_O and such approaches have been utilized to improve the performance of fuel cells [98]. However, doping may also raise E_a for V_O diffusion. For example, in Ni-doped $SrTiO_3$, E_a was measured to be $\sim$ 1 eV, an increase of 0.4 eV from undoped $SrTiO_3$ [114]. Electron paramagnetic resonance (EPR) spectroscopy also shows that long range diffusion can be inhibited through mobile V_O trapping through association with dopants [116, 117]. Such processes may represent an additional failure mechanism for electrodes [118], but may be useful to prevent oxidative degradation when $SrTiO_3$ is used as a coating. Compared with the large number of studies focused on probing V_O diffusion in undoped $SrTiO_3$, an atomistic picture of the interaction between V_O and dopant is still lacking. Indeed, MD simulations of dopant-V_O association in acceptor doped $SrTiO_3$ have shown that such events are complicated processes spanning several neighbor shells [112].

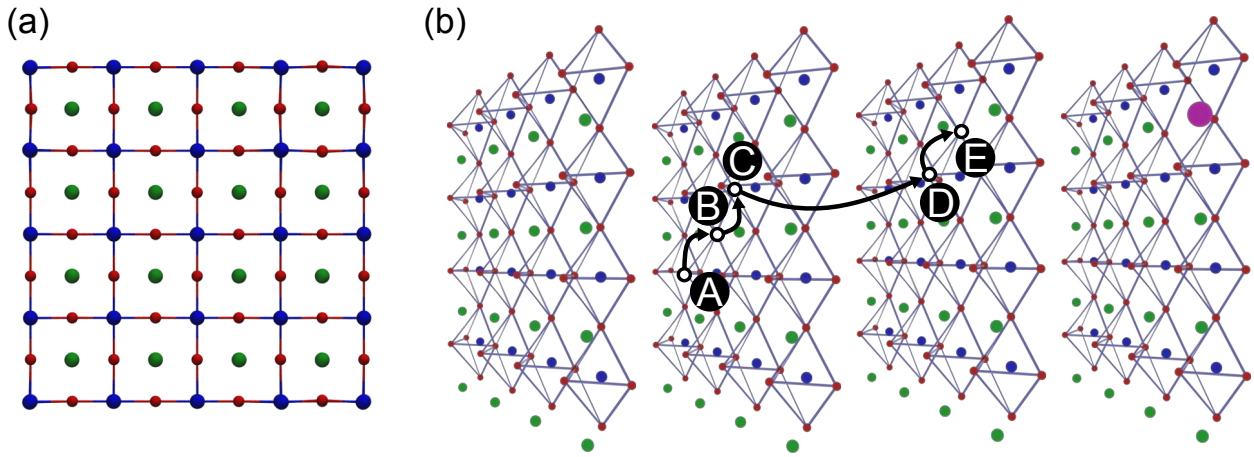

Figure 5.1: $SrTiO_3$ structure where the green, blue, red, and magenta spheres correspond to Sr, Ti, O and dopant atoms, respectively. (a) A single layer in 2D and (b) the simulated diffusion pathway for V_O in a four layer perovskite crystal. Each site is labeled by the letters in black circles. V_O starts at the farthest possible site from the dopant (**A**), and diffuses directly towards the dopant, ending at the nearest possible non-bonding site (**E**).

This study tackles the problem of V_O diffusion in doped $SrTiO_3$ by combining DFT and the nudged elastic band (NEB) method to calculate the energetics of both neutral ($V_O{}^{+2e}$) and ionized ($V_O{}^{0}$) migration in the presence of common A-site transition metal dopants: $Mn^{2+/4+}$, $Fe^{2+/3+}$, and Cr^{3+}. By utilizing large supercells, a quantum mechanical description along a realistic long-range diffusion pathway is developed. The results show that even at locations far from the defect, E_a of V_O migration is increased through doping. The magnitude of this increase can be predicted by the degree of covalent interaction between the dopant and bonding oxygens, or more rigorously by the amount of charge transferred to the perovskite lattice. Furthermore, trapping of V_O at dopant sites is a non-local event, with the energetically favorable complexation spanning several neighbor shells, and specific spatial extent for dopant association changing based on the amount of n-type character of the lattice ($V_O{}^{0}$ vs $V_O{}^{+2e}$).

5.2 Methods

To obtain a quantum mechanical description of V_O diffusion in $SrTiO_3$, the electron projector-augmented (PAW) scheme of DFT as implemented in the Vienna Ab Initio Simulation Package

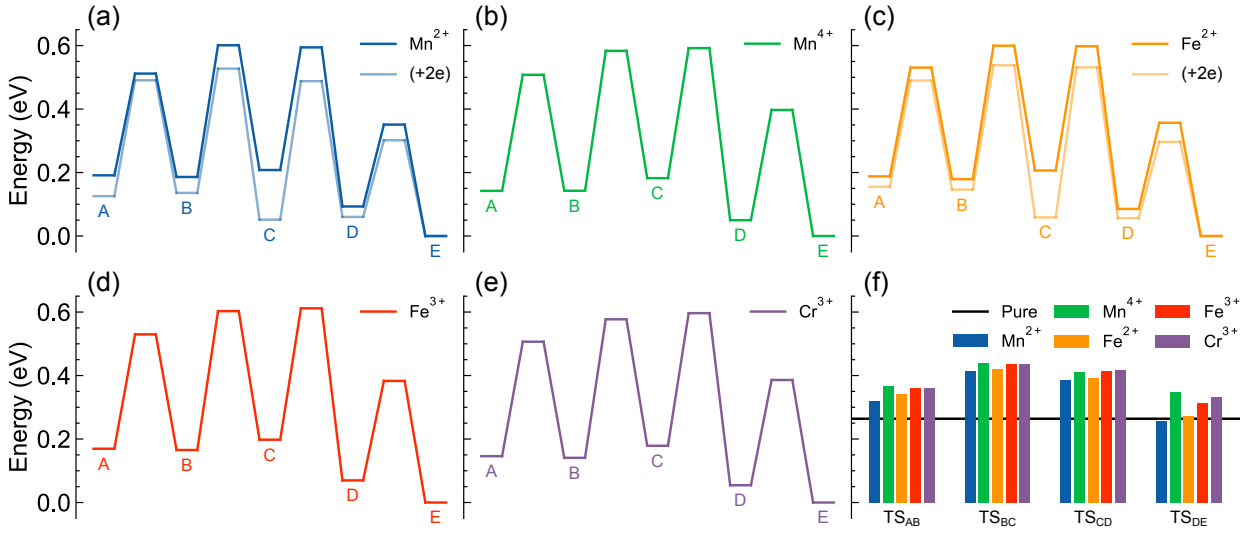

Figure 5.2: Energy barriers for $V_O{}^0$ and $V_O{}^{+2e}$ (+2e), lighter lines in (a) and (c), along the simulated diffusion path (Fig. 5.1). $V_O{}^0$ becomes associated with the dopant at **D** due to a large reversion barrier (TS_{DC}), while $V_O{}^{+2e}$ becomes associated with the dopant at **C** (large TS_{CB} barrier). (f) The activation energies for the forward path are plotted as bars for easy comparison. Activation energies for the reverse path are plotted as bars in Fig S4.

(VASP) [57] was used. PBEsol [119], a 600 eV cutoff for the planewave basis set, and pseudopotentials with core/valence configuration: Sr:[Ar]3d/4s4p5s, Ti:Ne/3s3p4s3d, O:He/2s2p, Cr:Ne3s/3p4s3d, Mn:Ne/3s3p4s3d, Fe:Ar/4s3d were used. All calculations were performed with spin polarization, where each element was initialized in its high-spin configuration, and an electronic convergence of 10^{-6} eV. Only the atom positions were relaxed, and calculations were carried out until the maximum force on any atom was less than 0.05 eV $Å^{-1}$ in any direction. Nudged elastic band calculations (NEBs) with 3 images along the path between the optimized initial and final V_O locations were carried out to calculate the activation energy (E_a) of each hop of the vacancy. Because of the high computational expense of performing calculations on such large unit cells, all calculations were performed at the Γ-point only.

PBEsol enabled the use of a large 325 atom 4 x 4 x 4 repeat of the primitive $SrTiO_3$ unit cell, allowing direct quantum mechanical examination of V_O diffusion at distances far from the defect, as well as at a lower defect concentration of approximately 0.5 weight %. Previous calculations of V_O diffusion in $SrTiO_3$ have introduced the Hubbard U correction to account

for the shortcomings of using a simple GGA functional to describe a highly correlated material [31]. To understand the ability of the PBEsol functional to reproduce the results of higher level methods, calculated E_a were compared with single-point energies at the PBEsol-optimized geometries using a more accurate hybrid functional, HSEsol [7]. For over 20 different transition states in a 3 x 3 x 3 Mn^{2+}–$V_O{}^0$ defected super cell, PBEsol only slightly over estimated the predicted E_a with maximum deviation between the two methods at approximately 0.05 eV (Fig. S2‡).

Dopant structures were created by inserting the respective metal atom onto a Sr site, followed by optimization to a 5-coordinate square pyramidal geometry that was previously shown to best reproduce the experimental hyperfine values for A-site doping of Mn^{2+}[15]. A V_O was then created and optimized at varying distances from the dopant to simulate a realistic diffusion path in the crystal (Fig. 5.1). The path was selected such that V_O began at the oxygen site furthest from the dopant (**A**), and over 3 intermediates (**B**,**C**,**D**) diffuses directly towards the dopant, terminating at one of the oxygens in the defected perovskite A-cell (but not bonded to the dopant, **E**). Dopant atoms were tested at multiple valences by altering the total number of electrons in the supercell. Furthermore, both ionized ($V_O{}^0$, vacancy of O^{2-}) and neutral ($V_O{}^{+2e}$, vacancy of O^0) vacancies were examined in the case of Mn^{2+} and Fe^{2+} dopants, with the latter possessing an additional 2 electrons in the supercell. In the more commonly used Kröger-Vink notation, these defects correspond to $V_O{}^{"}$ and $V_O{}^{x}$, respectively. Considering both defects is important as creation of $V_O{}^{+2e}$ drives complex dopant redox processes [115].

5.3 Results & Discussion

Under these calculation parameters, vacancy migration E_a for undoped $SrTiO_3$ in $V_O{}^0$ super-cells was approximately 0.2 eV. This E_a slightly underestimates most previous experimental and theoretical results, however reproduces those previously obtained using the same uncorrected GGA functional [31]. $V_O{}^{+2e}$ defected super cells predict E_a of approximately 0.4 eV, which agrees

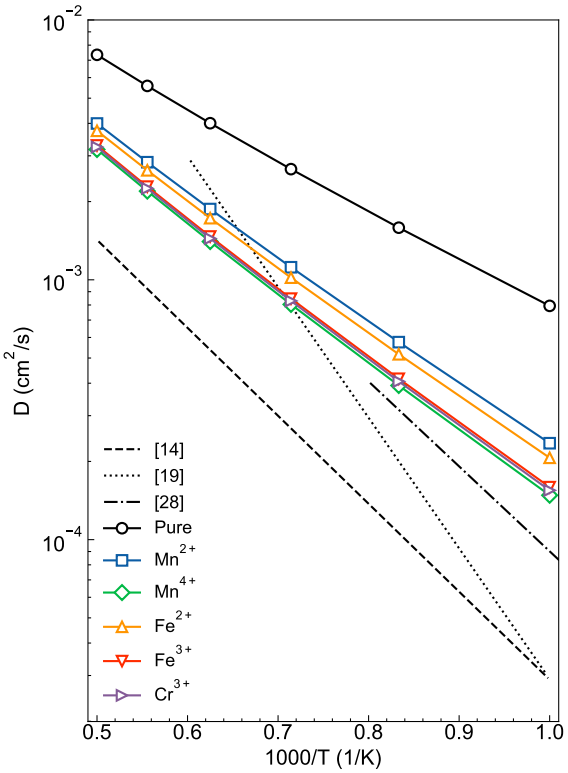

Figure 5.3: Temperature-dependent diffusion constant (D) calculated from transition state theory for dopant-$V_O{}^0$ supercells compared to experimental results from tracer diffusion [110, 120] and conductivity [114] measurements.

with previous DFT results [111]. E_a for both dopant–$V_O{}^0$ and dopant–$V_O{}^{+2e}$ defects were larger than that of the undoped crystal at nearly all transition states and dopants studied here (Fig. 5.1). In general, activation energy of the V_O hopping ranged from $\sim$ 0.30 to 0.45 eV (Table S1‡), with the largest E_a for the forward path towards the dopant occurring at TS_{BC} for all dopants. Both the Mn^{2+}–$V_O{}^{+2e}$ and Fe^{2+}–$V_O{}^{+2e}$ defected cells predict lower vacancy migration E_a than the respective $V_O{}^0$ supercells.

Despite small differences in V_O migration E_a there was no difference in geometry at any of the transition states for all hops and dopants. Furthermore, each geometry corresponds to those previously calculated for the undoped structure using DFT and DFT+U methods [31]. Additional attempts were made to relate the magnitude of E_a to structural parameters on the basis on Sr–Sr separation at the diffusion site, however no correlation was found (Fig. S3‡). Therefore, the small differences in both migration E_a and total energy when V_O is far from the defect may be due to subtle long-range reconstructions of the unit cell.

The experimentally observed trapping of mobile V_O through defect association appears in the reaction profiles (Fig. 5.2) as stabilization of those intermediates with V_O nearer the dopant. Notably, the spatial extent of trapping differs between $V_O{}^0$ and $V_O{}^{+2e}$ defect structures. Specifically, the energy-stabilization of vacancy-dopant associated complex occurs at the second neighbor shell (**D**) in $V_O{}^0$ cells (Fig. 5.2). This stabilization results in a large barrier for migration away from the dopant (TS_{DC}), effectively trapping the vacancy approximately 6 Å from the dopant. The dissociation barriers range from 0.50 to 0.54 eV for Mn^{2+} and Mn^{4+} dopants. Interestingly, trapping of $V_O{}^{+2e}$ occurs as far out as the third neighbor shell at **C** (Fig. 5.2), corresponding to a trapping radius of approximately 8 Å. The barriers for dissociation are $\sim 2k_BT$ lower in energy, 0.43 and 0.48 for Fe^{2+} and Mn^{2+}, respectively. Each of these values are in the range of experimentally reported dissociation barriers of 0.26 eV [117] to 0.7 eV [116].

To computationally predict macroscopic properties of diffusion, the average diffusion constant (D) for the forward and reverse diffusion paths were calculated for each dopant using rates

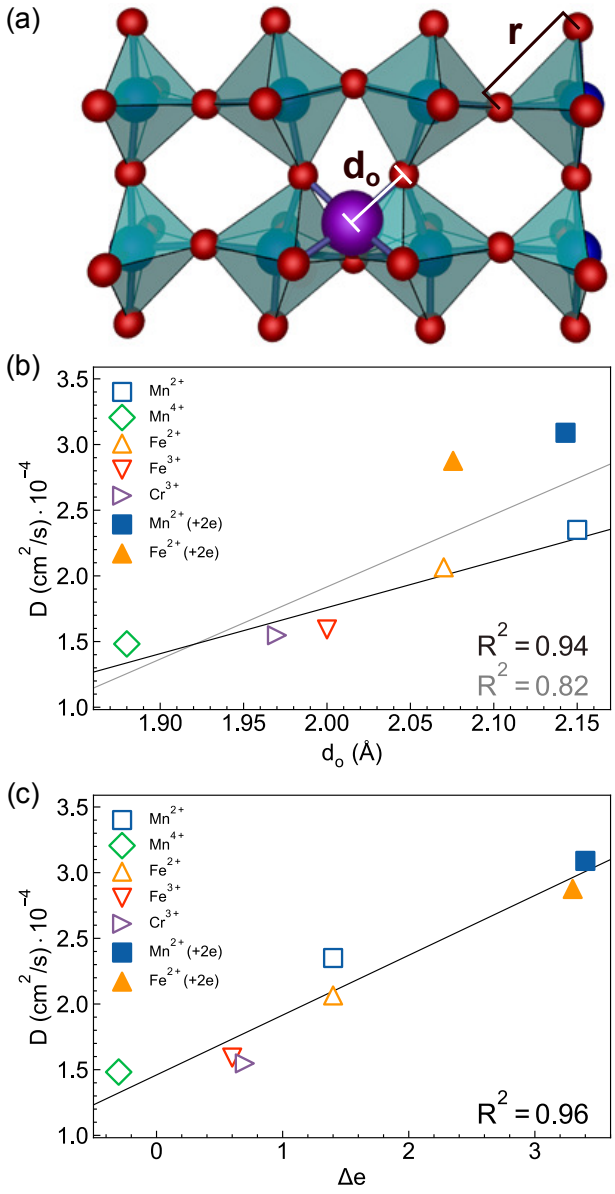

Figure 5.4: /
(a) Dopant induced strain with dopant oxygen bond length (d_O) and O–O distance (r) labeled. (b) Correlation between D at 1000 K and average dopant-oxygen bond lengths for dopant-V_O^0 (black line) and all supercells (gray line). (c) Change in the number of electrons in the $SrTiO_3$ lattice upon doping relative to the pure structure (Δe).

from transition state theory

$$D = \frac{1}{6} r^2 k \tag{5.1}$$

where r is the distance between adjacent O atoms in the pure crystal structure (2.789 Å Fig. 5.4A), k is the rate of the reaction determined from the average calculated E_a via the Arrhenius relation

$$k = \frac{k_B T}{h} e^{-\frac{E_a}{k_B T}}, \tag{5.2}$$

where h is Plank's constant, k_B is Boltzmann's constant, and T is the temperature. Using such an approach neglects effects like the ionic trapping discussed above, which would require considerably more advanced models that necessitate many more expensive calculations of accurate vacancy migration E_a, like Kinetic Monte Carlo (KMC). However, trapping effects are only critical determinants of D at low temperatures [112], far below typical operating temperatures for perovskite oxide devices.

D for dopant–V_O^0 systems is reduced versus the pure structure, as shown in (Fig. 5.3). Specifically, average diffusivity decreases $Mn^{2+} > Fe^{2+} > Fe^{3+} > Cr^{3+} > Mn^{4+}$ (Table S2‡). This represents a range of D of approximately 28–22 x 10^{-4} cm^2/s at 1000 K. Two possible mechanisms for this reduction are changes to the electronic structure induced by the p- or n-type doping of the dopant ion or structural strain of the crystal lattice. Indeed, both effects are capable of modulating E_a in undoped samples, evidenced by the change in E_a from 0.2 eV to 0.4 eV in the V_O^0 vs V_O^{+2e} defected structures, as well as previous results showing that compressive and tensile structural strain can raise or lower vacancy E_a[121], respectively.

To resolve the extent to which structure and electronic properties drive reduction of ionic diffusion, a structural description of strain that correlates with the migration E_a was found. The average dopant-oxygen bond lengths (d_O) (Fig. 5.4A) show that shorter d_O results in lower rates of vacancy diffusion. Attempting to fit this relationship for all supercells yields only marginal correlation (R^2=0.82, Fig. 5.4B). However, excluding the Mn^{2+}–V_O^{+2e} and Fe^{2+}–V_O^{+2e} data points from the fit improves the correlation significantly (R^2=0.94). The reason that V_O^{+2e} are

outliers can be understood by the changes in electronic structure via by Bader charge analysis (Table S3‡) [93].

As the number of electrons in the supercell increases, the $SrTiO_3$ lattice is increasingly reduced from Mn^{4+}–$V_O{}^0$ to Mn^{2+}–$V_O{}^0$ to Mn^{2+}–$V_O{}^{+2e}$. The 0.2 Å increase of d_O between Mn^{4+}–$V_O{}^0$ to Mn^{2+}–$V_O{}^0$ is driven by approximately 0.3 electron localized around the dopant. The rest of the two electrons added to the unit cell (1.7 electrons) delocalize in the crystal lattice (Table S3‡, Fig. 5.4C) coinciding with a 24% increase in the rate of diffusion. The additional two electron reduction of Mn^{2+}–$V_O{}^0$ to Mn^{2+}–$V_O{}^{+2e}$ results in no further reduction of the dopant and thus no significant change to d_O (2.15 Å and 2.16 Å). However, the even more highly reduced lattice increases the ionic diffusion by an additional 25 %. Therefore, the n-type character of the lattice, is likely the most important factor in determining the rate of ionic diffusion for doped semiconductors. The linear relationship between change in lattice charge and D (R^2=0.96, Fig. 5.4C) is consistent with the fundamental formula for ionic conductivity ($\sigma = nZ_{eff}\mu$) where Δe (Fig. 5.4C) alters the screening charge of the lattice (Z_{eff}).

Overall, this study provides the first quantum mechanical insight into long range V_O diffusion in doped $SrTiO_3$. The results capture the experimental observation that dopants raise the barriers of V_O diffusion and show that this largely arises as an electronic effect, opposed to an elastic one. Furthermore, the nature of V_O trapping through dopant association has been shown to be dependent on the number of electrons in the lattice, with more reduced structures able to trap V_O at longer vacancy-dopant distances. This provides two different approaches to tuning the V_O diffusion properties of $SrTiO_3$ based on the n-type character of the dopant. Such information will be critical to either enhancing or reducing ionic conductivity in targeted amounts, thus increasing the promise of $SrTiO_3$ in a number of technological applications.

Part III

Preparing Amorphous Material Models

Chapter 6

Bulk: Electronic Structure Insights Into Amorphous Al_2O_3[†]

Aluminum oxide Al_2O_3 is one of the most studied materials as applications seek to take advantage of the material's low cost, stability, and low environmental toxicity. These applications range from surface passivisation layers [122, 123], diffusion barriers [124, 125], and dielectric layers [126, 127]. In these applications, Al_2O_3 is often used in its amorphous form due to its good dielectric properties and robust growth chemistry via atomic-later-deposition (ALD) [128, 129]. The amorphous structure arising from the ALD process dictates physical properties such as band gap, defect levels, chemical stability, and catalytic behavior. Therefore, understanding the effect of the short- and medium-range order on ALD am-Al_2O_3 properties is critical for improving device performance.

Previous insights into the structure of am-Al_2O_3 have largely utilized X-ray [130–135], electron [136, 137], and neutron [131, 134, 135, 138] scattering. Such scattering data is then transformed into real-space to provide pair distribution functions (PDF) with information about short- and medium-range order (i.e., across length scales of 1–20 Å). These data can then be used to refine molecular dynamics (MD) or reverse Monte Carlo (RMC) simulations of atomic positions, yielding various structural quantities such as the average coordination number (e.g., $\overline{\mathrm{CN}}_{\mathrm{Al}}$ for

[†]Reprinted with permission from Pugliese A.; Shyam B.; Repa G.M.; Nguyen A.H.; Mehta A.; Webb E.B.; Fredin L.A.; Strandwitz N.C. Atomic layer deposited aluminum oxide thin films probed with X-ray scattering and compared to molecular dynamics and density functional theory models. *ACS Omega* **2022**, 7(45), 41033–41043.

the average coordination number around Al), the percentage of individual coordination numbers for each element (e.g., $^{[4]}$Al, for the percentage of Al coordinated by four oxygen atoms), bond angle distributions, and the presence of certain medium-range structures, such as assemblies of polyhedra [131, 139–141]. Instances of this approach have quantified a predominance of $^{[4]}$Al (57.5%) and $^{[5]}$Al (34.7%) coordination numbers for Al with minority components of $^{[3]}$Al (3.5%) and $^{[6]}$Al (4.3%) [142]. Conversely, ALD alumina–carbon nanotube composites indicated an average coordination number for Al of $\overline{CN}_{Al}$=4.76 [130], while an even a higher $\overline{CN}_{Al}$ was found for cryoelectron-based scattering and PDF analysis [136]. This prior work on electron and X-ray PDFs of ALD alumina exploited the high surface area of carbon nanotubes as a growth substrate, which may result in a different local or long-range structure compared to most ALD thin films due to the high degree of curvature [143]. Similarly, NMR studies of plasma-enhanced ALD (PEALD) aluminum oxide revealed $^{[4]}$Al (54.3%), $^{[5]}$Al (40.6%), $^{[6]}$Al (5.1%).

Considering the high structural variability of differently prepared am-Al_2O_3 samples, an understanding of how synthetic factors lead to observed changes in measured properties has proven difficult for amorphous materials. Furthermore, little is known about the local structure in ALD alumina, and X-ray PDF data on planar ALD alumina has not yet been reported. Without a good experimental understanding of the local atomic structure of ALD alumina, it is difficult to build accurate computational models that might yield a better understanding of the what structural motifs that lead to the measured properties, such as fixed charge [144, 145], of these important films. Additionally, first-principle calculations, such as density functional theory (DFT), that have proven useful in understanding the properties of crystalline materials are hindered by N^3 scaling (N being a measure of system size, i.e., atoms, bands or basis functions, and unit cell volume), and amorphous materials typically need large unit cells (on the order of thousands to tens of thousands of atoms) to accurately match experimental PDFs. Further, imposing any periodicity on an aperiodic system will inherently create artifacts that may only be due to the model and not the material. Thus, first-principles predictions for amorphous materials have been limited to those for which relatively small unit cells (<500

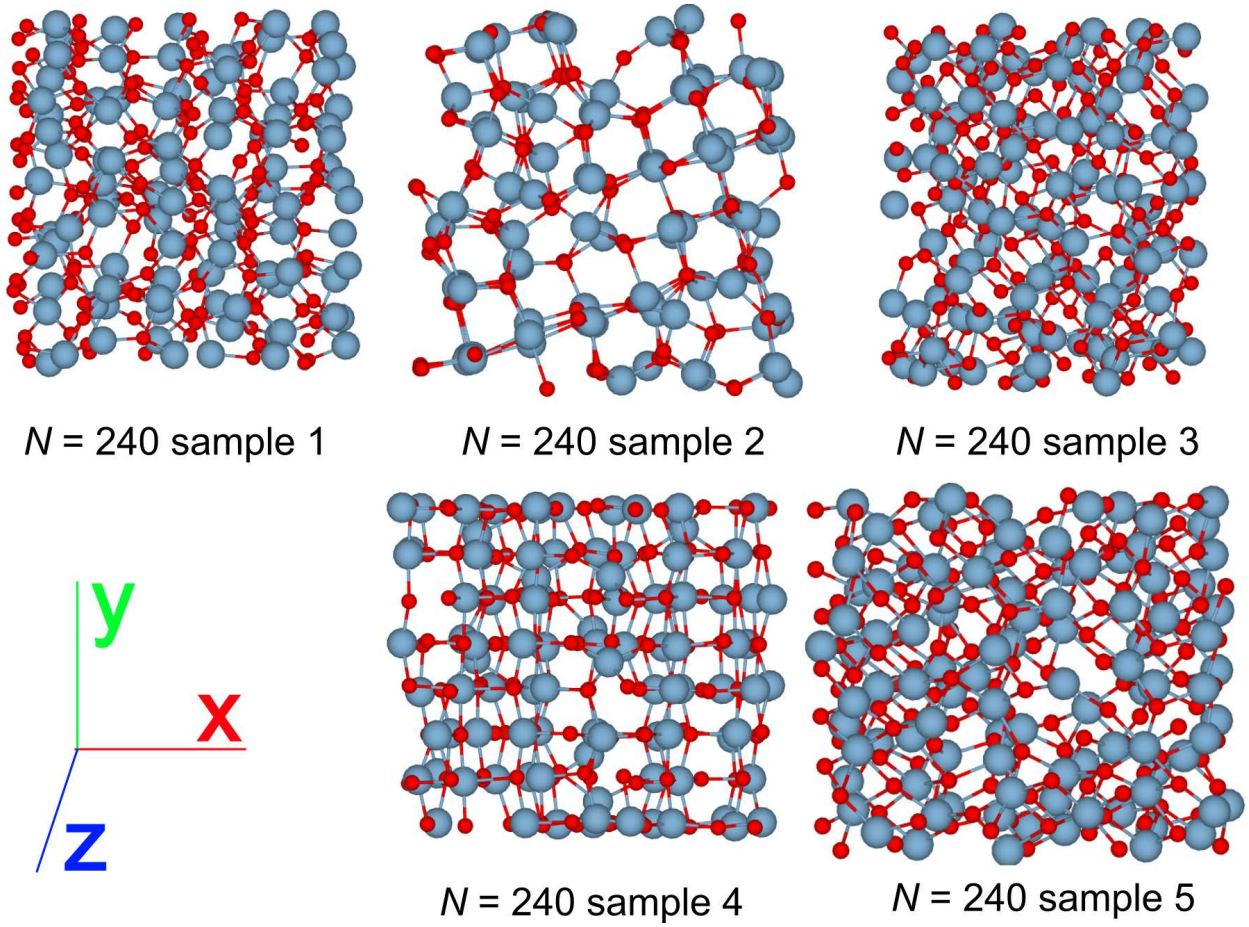

Figure 6.1: N = 240 am-Al_2O_3 unit cells.

atoms) are generated directly by MD [146] or at the local density approximation [147] level of theory.

This work combines grazing incidence synchrotron X-ray scattering, MD simulations, and DFT-based calculations to provide a better understanding of the geometric and electronic structures of amorphous ALD films. In particular, grazing incidence synchrotron X-ray scattering data were compared to MD simulations that modeled short- and medium-range order in amorphous ALD alumina planar thin films in the as-deposited state and after annealing at 450 and 700 °C in air. MD-generated unit cells exhibiting similar the short- and medium-range characteristics of the ALD films were analyzed using DFT, providing evidence of possible structural motifs that lead to the trap states in these films.

6.1 Computational Method

First-principles calculations were carried out using density functional theory (DFT) and the electron projector-augmented wave (PAW) scheme as implemented in the Vienna Ab Initio Simulation Package (VASP) [57, 84]. Each calculation was performed using a 400 eV plane-wave cutoff coupled with the hybrid HSE06 [148] correlation-exchange functional and the following [core]valence configurations for each element: Al = [Ne]3s3p and O = [He]2s2p. Density of states (DoS) calculations for the crystalline α- and θ- and θ_{fit}-Al_2O_3 polymorphs were accomplished using 30 and 10 atom unit cells, respectively, with k-space integrations over an 8 × 8 × 12 Γ-centered k-point grid. As the amorphous unit cells are not definable by k-vectors, we report only the DoS sampled at the Γ-point (i.e., the 1 × 1 × 1 grid). Because of the large lattice dimensions of the N = 240 unit cells, the Γ-point-sampled electronic structure likely captures a large number of the electronic states of each unit cell.

6.1.1 Results and Discussion

6.1.2 X-ray Scattering and Molecular Dynamics[‡]

Grazing incidence X-ray scattering measurements were carried out on aluminum oxide thin films grown using thermal atomic layer deposition. The corresponding pair distribution functions showed structures similar to previously reported PDFs of solid-state amorphous alumina and molten alumina. Structural models based on crystalline alumina polymorphs (PDFgui) and amorphous alumina (molecular dynamics, MD) were examined for structural comparisons to the experimental PDF data. Smaller MD models were optimized and verified against larger models (Fig. 6.1) to allow for quantum chemical electronic structure calculations.

[‡]Methods and detailed results for film growth, film measurements, PDFgui simulations, and molecular dynamics simulations are available at https://doi.org/10.1021/acsomega.2c04402.

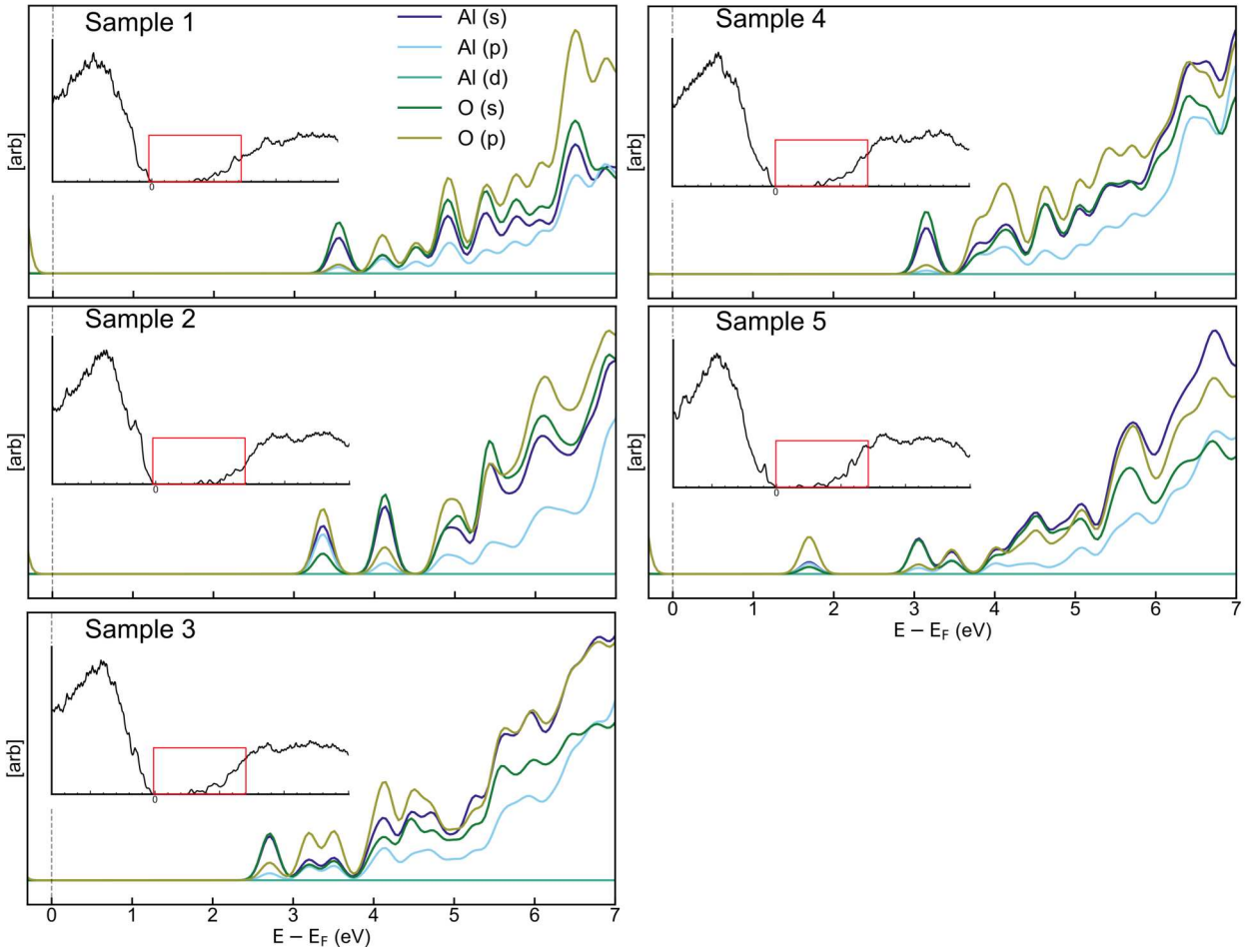

Figure 6.2: Orbital resolved DoS of the band edges of each N=240 sample.

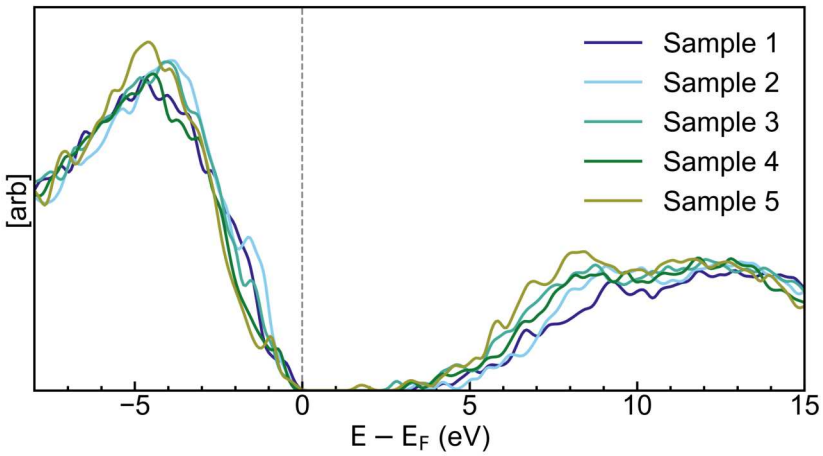

Figure 6.3: Total density of states for each amorphous N=240 Al_2O_3 sample.

6.1.3 DFT Analysis of MD-Derived Amorphous Structure

The N=240 unit cells were used as inputs in DFT calculations to examine the electronic structure of amorphous alumina. These are directly compared to that of crystalline ($\alpha$and θ) Al_2O_3 and the PDFgui-modified θ_{fit} phase. The DoS of the crystalline Al_2O_3 structures confirms that in each crystalline polymorph the valence band (VB) is hybridized oxygen p and aluminum d orbitals while the conduction band (CB) is a mix of p and s character (Fig. 6.2) [146, 147, 149]. The largest band gap (E_G) is calculated for the α-Al_2O_3 polymorph at 7.76 eV. This value was reduced to 6.46 and 7.08 eV for the θ and θ_{fit} polymorphs, respectively. The DoS values show that the increase in E_G from θ to θ_{fit} is due to the red-shifting of a small shoulder peak of mainly p character away from the Fermi energy (E_F) in θ_{fit}. This effect can be attributed shorter Al—O bond lengths and thus better orbital overlap between Al and O atoms, which result in a lower-energy peak in θ_{fit}. Similar differences in band edge positions arising from variations in the local Al–O symmetry were documented previously [150].

The high disorder of am-Al_2O_3 the variation in the five N = 240 unit cells, and the symmetry restriction to Γ-point sampling could make the DFT analysis of the electronic structure of these materials difficult [151–155]. However, the slight variations seen in the $G(r)$ data and bond angle distributions of each N = 240 unit cell does not lead to a large difference in the DoS (Fig. 6.3) or the orbital-resolved projected DoS (Fig. 6.2). However, the atomic disorder creates a

large number of tail states that result in the significant disruption of defined VB and CB edges, in comparison to the crystalline structures, and prevents the conclusive assignment of E_G. To gain further insight into the nature of these tail states, we calculated the inverse participation ratio (IPR) for each amorphous sample, which was defined for the ith Kohn–Sham orbital ψ_i in real space as

$$IPR(\psi_i) = \sum_{i=1}^{N} \frac{|\psi_i|^4}{|\psi_i^2|^2} \tag{6.1}$$

Such analysis has been used extensively to investigate the electronic properties of amorphous materials [153, 154, 156]. The IPRs for the five amorphous samples indicate that the greatest degree of localization occurs for electrons at the top of the VB (Fig. 6.4), as delocalized bands are not found until approximately 2 eV below E_F. Inspection of the charge density of these tail states across all five samples shows that electrons localize in 2p orbitals centered on twofold-coordinated bridging oxygens (Fig. 6.4). These states are unique to the amorphous structure, as the crystalline polymorphs contain only threefold- and fourfold-coordinated oxygens.

Above E_F, low IPR values indicate the formation of extended Bloch states that allow the qualitative estimation of the mobility edge, giving an approximate E_G of 6–7 eV for the amorphous samples. However, in several of the samples studied, localized electron traps occur approximately 2 eV or more below the extended CB edge. These states consist of regions of localized charge density within cavities formed by Al–O ring-like structures in the material (Fig. 6.4). Electron trapping in such sites was previously suggested to be the source of a number of observed properties, particularly negative charging in amorphous Al_2O_3 films [157]. Among the five amorphous samples studied here, the degree of localization, energetics, and structural motifs that contribute such electron traps are highly variable. However, all samples indicate that both twofold-coordinated oxygen and Al–O rings are critical structures that exist in the amorphous material and change the electronic properties.

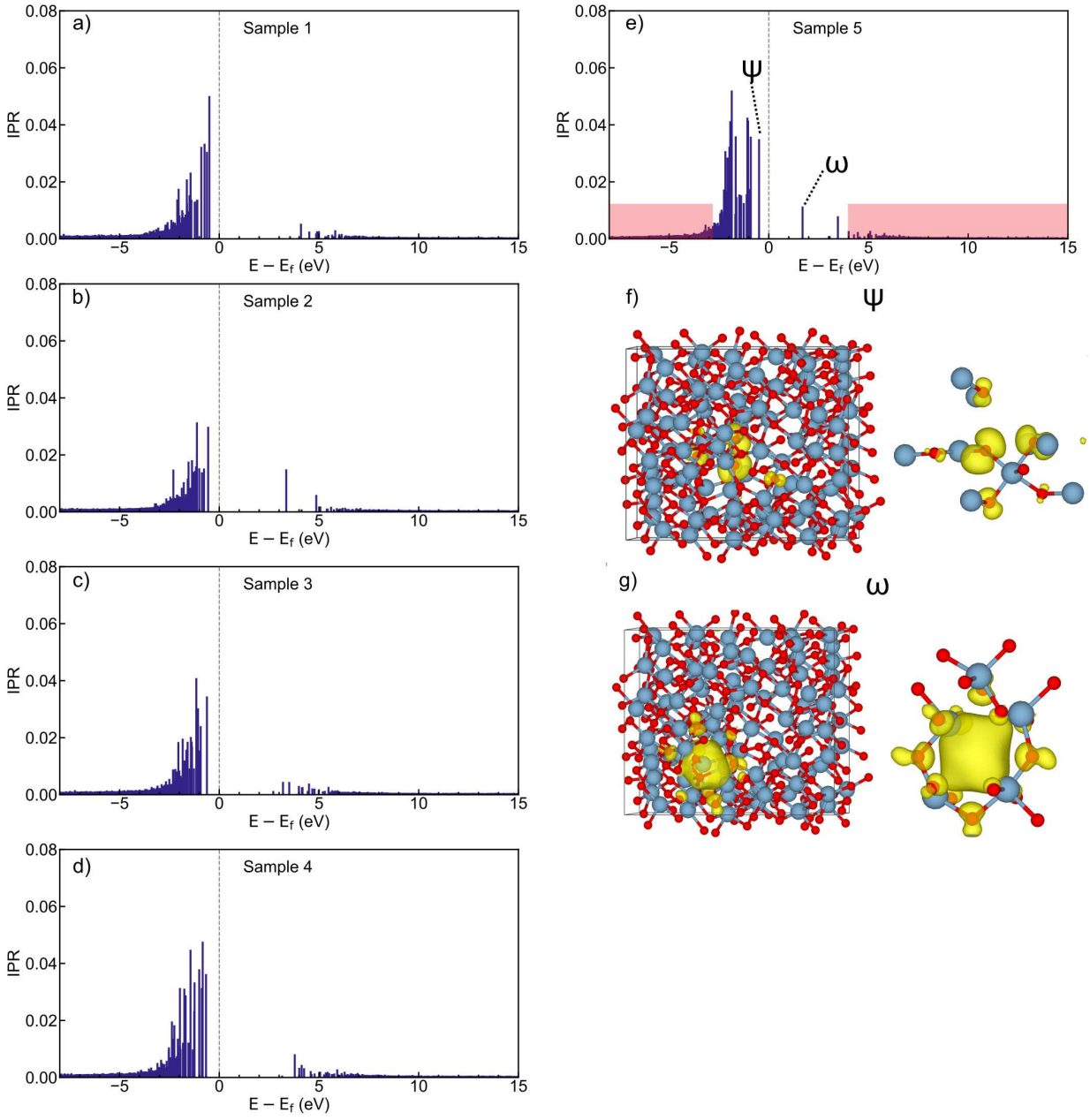

Figure 6.4: Inverse participation ratio for each amorphous sample (a-e) with charge density of localized VB edge (f) and electron trap (g). The locations of the states depicted in (f) and (g) in the electronic structure are denoted in (e) with ψ and ω respectively. The shading in (e) represents the delocalized states beyond the qualitative mobility edge.

6.2 Conclusions

X-ray scattering-derived structural data were acquired for ALD alumina films with different thermal histories. Notably, similar short-range order was found for these samples compared to molten and other amorphous alumina samples. The closest crystalline structural analog was found to be θ-alumina. More realistic structural models were created using MD, and these models matched well with peak positions from the X-ray-based PDF data and prior MD results. Careful downscaling of the MD model size resulted in DFT-tractable models largely consistent with larger models. The calculated electronic structure confirmed that most of the properties of amorphous alumina are similar to those of θ-alumina. However, Al–O alternating ring structures and twofold-coordinated oxygen lead to midgap electron traps and the modification of the valence band edge, respectively.

Chapter 7

Surfaces: Preparing Realistic Amorphous TiO_2 Surfaces[†,‡]

A fundamental goal of materials chemistry is to understand how specific arrangements of atoms in a solid give rise to observed properties. This understanding is particularly challenging for amorphous materials, which are characterized by high degrees of disorder and lack of long-range structure; opposed to crystalline materials that can be defined in terms of a single repeating unit. Despite the difficulties defining their atomistic structure, amorphous materials are ubiquitous and have high technological relevance. For example, structurally amorphous materials can act as the dielectric layers in transistors [126, 127], surface passivation layers [122, 123], and photocatalysts [158, 159].

On the basis of this high technological interest, there have been a number of computational studies that attempt to probe the structural and electronic characteristics of amorphous materials. These studies have afforded insight ranging from the self-trapping of holes and electrons [154, 155, 160] to defect and dopant effects [156, 161–163]. It is difficult to run first principles calculations with the large number of atoms needed to define the amorphous structure, as well as generate atomistic structures that are representative of real materials. To address the latter, the "melt-quench" method [153–155, 160, 161, 164], which involves using classical or *ab initio* dynamics simulations to heat a sample to a liquid phase, and then quenching the melt in order to lock in the amorphous configuration, has emerged as a convenient way to generate amorphous

[†]Portions of this chapter have been published in Repa, G.M.; Fredin, L.A. Predicting electronic structure of realistic amorphous surfaces. *Advanced Theory and Simulations* **2023**, 2300292.

[‡]Electronic supplementary information is available at https://doi.org/10.1002/adts.202300292.

unit cells.

Alternative methods for generating amorphous structures range from Reverse Monte Carlo Simulations to directly match to experimentally obtained X-ray data [165, 166], to amorphous unit cells generated via deep learning approaches [167, 168], to actually modelling the synthetic processes of real amorphous surfaces [169]. These vary in complexity, and each of these methods have their pros and cons. In particular, they require a lot of judgement calls on how to set up the simulations and determine what is a "good" fit to experimental data. Consequently, they have not displaced the melt-quench method.

While insights provided by these atomistic models have provided unparalleled structural insights, a complete picture of their structure-function relationships has remained elusive as most models available are too large for high quality electronic structure methods, even density functional theory (DFT). A particularly challenging area of amorphous theory is understanding the surface structures and interfacial chemistry of these materials [170]. Indeed, the performance of amorphous based devices in catalysis, solar energy generation, electronics is highly dependent on their interfaces [171–173]. To achieve an amorphous surface, oftentimes a melt-quench bulk structure is cleaved via optimization with a large vacuum placed in the direction orthogonal to the surface [161, 174–176]. However, the suitability of this approach for generating amorphous surfaces has recently been called into question [177, 178]. Specifically, this approach necessarily involves a high amount of bond breaking as the periodic boundary condition in the surface direction of the low energy quench is disrupted when creating the interface. This approach may ultimately result in structural artifacts that render the unit cell non-representative of experimental counterparts. A more intuitive approach to generate thermodynamically relevant surface bonding is to cleave in the high energy melt phase so that the surface can be quenched and optimized under non-periodic boundary conditions. This approach allows for a larger amount of surface reconstruction and topology [178, 179]. Critically, the morphology of experimental amorphous surfaces can be modified by different synthetic conditions or synthesis precursors to produce varying degrees of surface roughness [180, 181], and thus a robust com-

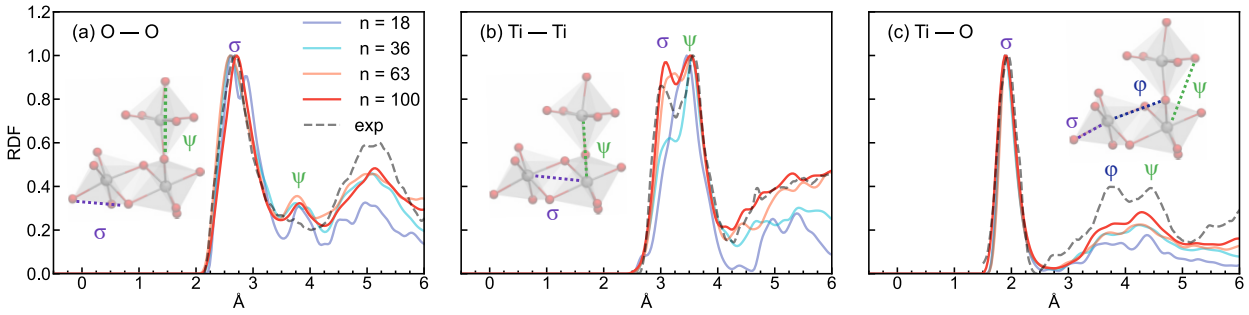

Figure 7.1: Radial distribution functions O–O (a), Ti–Ti (b), and Ti–O (c) bond lengths of various $(TiO_2)_n$ of surface quenched amorphous unit cells compared to the sputtered am-TiO_2 [182]. Important structural motifs from each distribution are shown as insets.

putational model of amorphous materials would need to be able to produce a range of surface morphologies.

Initial implementations of the different cleaving protocols have focused on the differences in the structural morphologies that can be generated. However, the electronic structure of these amorphous surfaces that are critical to the properties, for example identification of catalytic active sites, have been largely overlooked. To address this issue, this chapter presents the first direct comparison between periodic and surface quench derived slab models of titanium dioxide.

Many applications, ranging from the electrodes in photocatalytic reactions, to hydrogen storage and sensors, to batteries, take advantage of TiO_2's low cost, stability, and low environmental toxicity, making it one of the most studied amorphous materials. Indeed, it is oftentimes amorphicity of TiO_2 and its associated effects on electric and mechanical properties that determines device performance. For example, am-TiO_2 nanosheets have shown increased surfaced enhanced Raman scattering [183], the lithium-storage capability of silicon nanoparticles is greatly improved when encapsulated with am-TiO_2 [184], and am-TiO_2 protective coatings on water splitting electrodes have been shown to simultaneously protect against oxidation while facilitating hole conduction [185].

In this work, we explore the parameters that influence the experimental accuracy of an am-TiO_2 surface model. In particular, the electronic structure of periodic vs. surface quenched

am-TiO_2 reveal critical differences in the predicted properties of the two methods. In addition, there are other modeling considerations that have not been standard for amorphous materials, including the number of unit cells needed to achieve adequate sampling of structural space, and the minimum unit cell sizes needed to reproduce experimental data, which have a substantial effect on the understanding that can be learned from computationally derived amorphous interfaces. The results of this study not only provide new insights into this important material, but also demonstrate the urgent need for robust computational approaches for generating realistic amorphous surfaces.

7.1 Computational Methodology

7.1.1 Melt-Quench Procedures

Common methodology for generating amorphous surfaces utilizes the "melt-quench-cleave" approach where the unit cell is cleaved after quenching and may then be subject to geometric optimization. This method has been implemented in the current work using the Matsui-Akaogi potential for TiO_2 [186] in LAMMPS [187]. First, individual Ti and O atoms were randomly packed into a cubic unit cell corresponding a density of approximately 3.9 g/cm^3 using the packmol program [188]. The number of TiO_2 units and box size was varied from $(TiO_2)_{18}$ to $(TiO_2)_{100}$ with lattice parameters ranging from 8 x 8 x 8 Å to 15 x 15 x 15 Å. To study the effects of quench procedure and quench rate, the largest of these unit cells with 100 TiO_2 units was selected. Larger cells would be more ideal for studying amorphous structures, however unit cells with $\gtrsim 300$ atoms are already at the edge of what is computationally affordable for subsequent DFT calculations. Each cell was then equilibrated using fully periodic boundary conditions in an NVT ensemble for 100 ps at 3000 K, which is above the melting temperature of TiO_2 of 2116 K. This was following by further equilibration in an NPT ensemble for an additional 200 ps, where the density was converged to approximately 3.5 g/cm^3. These equilibration times were sufficient to yield converged ensembles (Figs. S1‡ and S2‡). Diffusion analysis showed the

average mobility for each Ti atom is D $\approx 4x10^{9}$ m^2/s, which corresponds to the expected value for the liquid state. The system was then allowed to evolve in the NPT ensemble at 3000 K, with structures selected for cooling every 500 ps. The long sampling time of the melt ensured that unique atom configurations were selected at each point. The structures were then cooled in the NPT ensemble to 300 K at the prescribed cooling rate, following by additional NPT equilibration for 100 ps. A total of 6 different cooling rates were examined ranging from 0.574 K/ps to 100 K/ps.

Periodic Quench: Cleavage of the structures was then accomplished by the insertion of approximately 100 Å of vacuum space above the surface, and neglecting the slab-slab dipole contribution to the total energy. The resultant structures were then subject to preliminary optimization using the Matsui-Akaogi potential until the maximum force on each atom was less than 1.0 x 10^3 kcal x mol / Å. Cells prepared using this method are henceforth referred to as those derived from periodic quenches.

Surface Quench: To prepare the surface quenched structures, the cleavage step above was performed following initial NPT and NVT equilibration of the bulk fully periodic unit cell at 3000 K. The system was then allowed to evolve for an additional 100 ps at 3000 K in the NVT ensemble prior to selecting structures for quenching. Structures were sampled from the NVT ensemble at the same interval as the bulk quenched structures, and cooled at the corresponding rates in the NVT ensemble. As the vacuum space in the cell prevents determination of unit cell lattice parameters, the x- and y-lattice parameters of each quench was adjusted to match the average achieved by the bulk cells of the corresponding quench rate. In most cases, we find that the deviation of the lattice parameter from the high energy melt is less than 0.3 Å. These cells were then equilibrated with the NVT ensemble, and subject to the same preliminary optimization as described above.

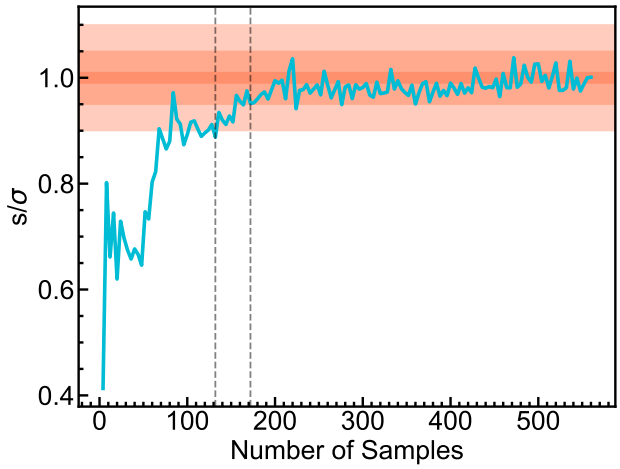

Figure 7.2: Structural variability (s/σ) with increasing sample sizes. The lines at number of samples = 124 and 172 indicate the number of quenches needed to converge s/σ to 90 and 95% respectively. Shading indicates convergence threshold for 90, 95, and 99%, with increasing opacity.

7.1.2 Density Functional Characterization

Following molecular dynamics preparation, full quantum mechanical optimization of the unit cells was performed in the Vienna Ab initio Simulation Program (VASP) [57, 84]. We adopted an energy cutoff of 400 eV to expand the electronic wave function, and valence configurations of the atoms: Ti:[Ne]/3s3p4s3d, O:[He]/2s2p. All calculations were performed with Γ-point sampling using the PBEsol functional [119]. Each structure was relaxed until the energy between successive optimization steps was less than 10^{-3} eV. Optimizations were performed with a 15 Å vacuum between periodic slab images, and neglect of the dipole contribution to the total energy in the direction orthogonal to the slab surface.

7.2 Results and Discussion

7.2.1 Unit cell size

There are well known issues of artificially periodic models representing experimentally aperiodic systems in DFT calculations, which has motivated many previous am-TiO_2 studies to select

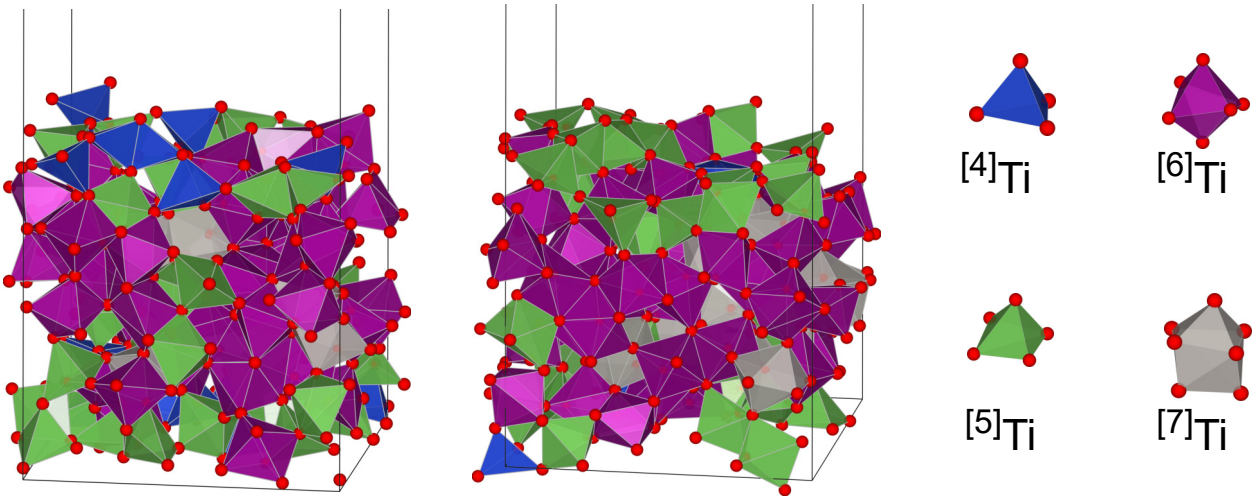

Figure 7.3: Periodic (left) and surface quenched (right) unit cells from quench rate 10 K/ps, with the Ti coordination colored.

larger unit cell sizes than are traditionally used for crystalline materials. Unit cell sizes in previous studies have ranged from $(TiO_2)_{32}$ [160, 189] to $(TiO_2)_{90}$, [154] with $(TiO_2)_{72}$ commonly used [155, 190–192].

In order to maximize the reliability of the representation of am-TiO_2 in the current work, a comparison of different DFT tractable unit cell sizes was performed for the surface quench procedure that is less well explored. Initial, bulk unit cell sizes and cubic cell volumes were: $(TiO_2)_{18}$, V = 8^3 Å; $(TiO_2)_{36}$, V = 10^3 Å; $(TiO_2)_{63}$, V = 12^3 Å; and $(TiO_2)_{100}$, V = 15^3 Å.

In general, all unit cells (Fig. 7.1) are able to reproduce the experimental radial distribution functions (RDFs) for O–O and Ti–O separation distances for sputtered am-TiO_2[182]. Specifically, peaks occur for the innermost coordination spheres at approximately: r_{Ti-O} = 1.9, and r_{O-O} = 2.6. There is some small splitting of the r_{O-O} peak into a doublet for the $(TiO_2)_{18}$ unit cell that is not present in either the larger unit cells or experimental data. In the O–O RDF, the two peaks correspond to the separation between two O atoms that comprise a TiO_6 octahedra edge and a single octahedra respectively (labeled in Fig. 7.1a inset). The intensity of the latter is highly diminished in the experimental data. However, it is prominent in the calculated RDFs of many other am-TiO_2models prepared using the Matsui-Akaogi potential [154, 193].

While O–O and Ti–O interatomic separation distances are reasonably captured by all unit

cell sizes examined here, there is a notable difference in the Ti–Ti interatomic separation distances. In the experimental data, this spectra is characterized by two peaks centered on r_{Ti-Ti} = 3.0 Å and r_{Ti-Ti} = 3.5 Å. These two peaks correspond to the separation between Ti atoms of edge-sharing and corner-sharing octahedra respectively (Fig. 7.1b inset). However, the small $(TiO_2)_{18}$ only shows the latter of these peaks. Furthermore, intensity of the first peak is greatly diminished in the $(TiO_2)_{36}$ unit cell. Indeed, only the $(TiO_2)_{63}$ and $(TiO_2)_{100}$ unit cells are capable of reasonably reproducing the experimental spectra. This suggests that 63 TiO_2 units or at least 12 Å lattice parameters are necessary to capture experimental structures.

7.2.2 Sampling Parameters

Independent amorphous quenches result in slightly different structures. Previous studies on bulk amorphous materials have generally produced sample sizes ranging from one [155, 176] to a few [164] independent quenches. Such small sample sizes may be insufficient to explore enough structural space for universally applicable conclusions. However, it is important to avoid wasteful re-calculation of duplicate structures to limit the computational cost of the electronic structure calculations. To quantify the amount of new structural information returned by each quench sample, the smooth overlap of atomic positions (SOAP) method [194] is adopted to describe 560 different quenches. A brief review of the SOAP methodology and its implementation in the current work is available in the SI‡, however a rigorous mathematical derivation is provided in refs. [194, 195].

The SOAP method provides a distance metric to compute the similarity between two atomic environments that is invariant with respect to rotation or translation. The appeal of such an approach is that all structural features of the unit cell are considered, and a single distance indicates the similarity between different unit cells. To quantify the amount of new structural information that is being returned by each additional quench, this distance was projected into 1-dimension. The sample standard deviation (s) of a given number of replicates was then divided by the population standard deviation (σ) for all 560 quenches for increasingly sample sizes (Fig.

7.2). Using this method, it is found that s/σ is 90 % converged (i.e., s/σ < 1.1) with approximately 124 different samples. By 172 unique quenches, s/σ was converged to approximately 95%. This number provides a reasonable target for amorphous studies aiming to efficiently explore a large region of amorphous phase space using similar sized unit cells. Significant improvements in convergence beyond 95% were not achieved when testing up to 560 independent quenches.

7.2.3 Surface vs Periodic Quench

Quench rate and quench boundary conditions have the largest effect on the surface structure generated in each amorphous surface unit cell. Six different quench rates were examined: 0.574 K/ps, 1 K/ps, 5.745 K/ps, 10 K/ps, 57.447 K/ps, and 100 K/ps. A total of 20 $(TiO_2)_{100}$ unit cells were prepared for each quench rate, with 10 prepared using the surface quench protocol and 10 prepared using the periodic quench protocol.

RDFs for each quench rate and quench protocol show excellent agreement among past experimental and theoretical results for bulk amorphous TiO_2 (Fig. S3), with no large distinctions [154, 182]. Bond lengths and angle distributions (Figs. S4-S6‡) also are very similar for the differently prepared systems. Ti–O bond lengths are represented by a single distribution centered at 1.9 Å. The distribution of angle Ti–O–Ti is largely bimodal with peaks at approximately 97°and 130°. These angles can be attributed to the angles between corner-sharing and edge-sharing TiO_6 polyhedra respectively. Accordingly, two populations of O–Ti–O are formed by axial-equatorial and axial-axial O–Ti–O angles. These results indicate there is no difference between the close-range geometry of individual TiO_6 polyhedra composing amorphous surfaces prepared by different methods.

In real am-TiO_2 samples, experimental measurements have shown that various degrees of surface roughness are possible depending on experimental conditions [196]. This ability to tune surface properties is key for optimizing the performance of amorphous devices. To determine the ability of the proposed computational model to capture these features the Van der Waals surface area and surface ruggedness for each quench rate (Figs. S7‡ and S8‡) were plotted. These

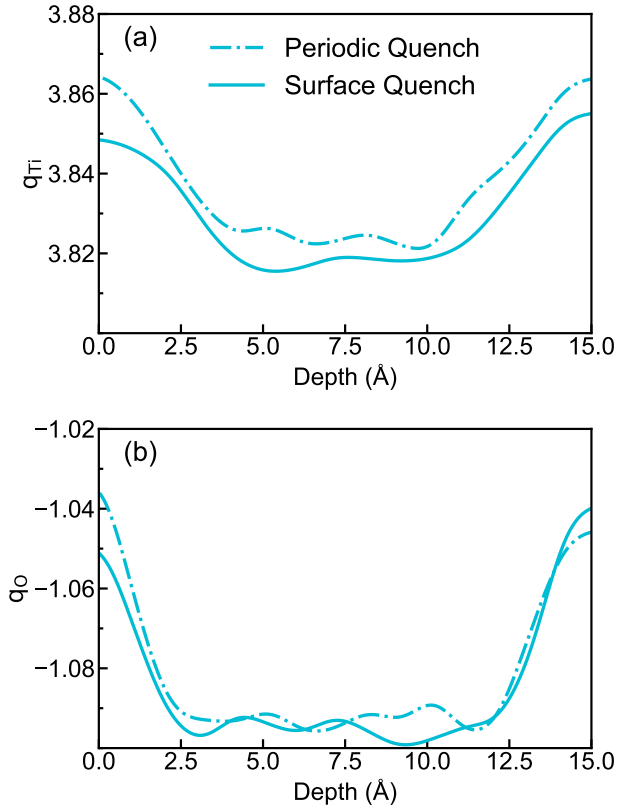

Figure 7.4: Bader charge [93] on Ti (a) and O (b) as function of depth for surface and periodic quenches at 10 K/ps quench rate averaged over 10 structures each.

results show that the surface quenching predicts comparable, but slightly less rough surfaces than the periodic quenching protocol at the two slowest quench rates. However, at increasing quench rates, the roughness of structures prepared from the surface quenching approach is increased, while structures from periodic quenches remain fairly constant. These findings are consistent with those found for melt-quench study of amorphous silica [178], and demonstrate that a combination of surface quenching and quench rate can be used to control the degree of surface roughness. Using surface quenching approaches allows models with increased surface roughness of experimental samples to be generated, which is critical for predicting realistic electronic structure.

Experimentally different surface topologies have a significant effect on the surface chemistry of amorphous materials [126, 180, 181]. Thus, the generated compositions of each different surface topology (Fig. 7.3) are critical to predicting the electronic and catalytic properties. For the 10 K/ps quench rate, the average Ti coordination number ($^{[N]}$Ti) is significantly reduced in periodic quenched cells compared to the surface quenched cells with average N = 5.25 and N = 5.34, respectively. For comparison, the experimental Ti coordination number in approximately 2 nm colloidal TiO_2 particles was found to range from 3.9 to 5.8 [197], while $^{[N]}$Ti for bulk sputtered am-$TiO_2$was found at N = 5.4 [182]. Plotting $^{[N]}$Ti probability as a function of depth from the surface (Fig. S9‡) reveals an increased number of $^{[4]}$Ti on the surface of periodic quenched cells, and almost none present in surface quenched cells. Importantly, at all quench rates the periodically quenched cells have a high number of $^{[4]}$Ti, resulting in drastically different surface structures for the periodic and surface quenches (Fig. 7.3). Specifically, creating the vacuum necessarily involves breaking Ti–O bonds across the periodic boundary, resulting in under coordinated Ti that are unable to fully relax post-cleavage during geometric minimization in the low-energy melt.

The significant differences in the surface topology and structure of amorphous samples prepared by the two different approaches also result in significant differences in their electronic structure. Band gaps for each quench method show that periodically-quenched structures (Figs.

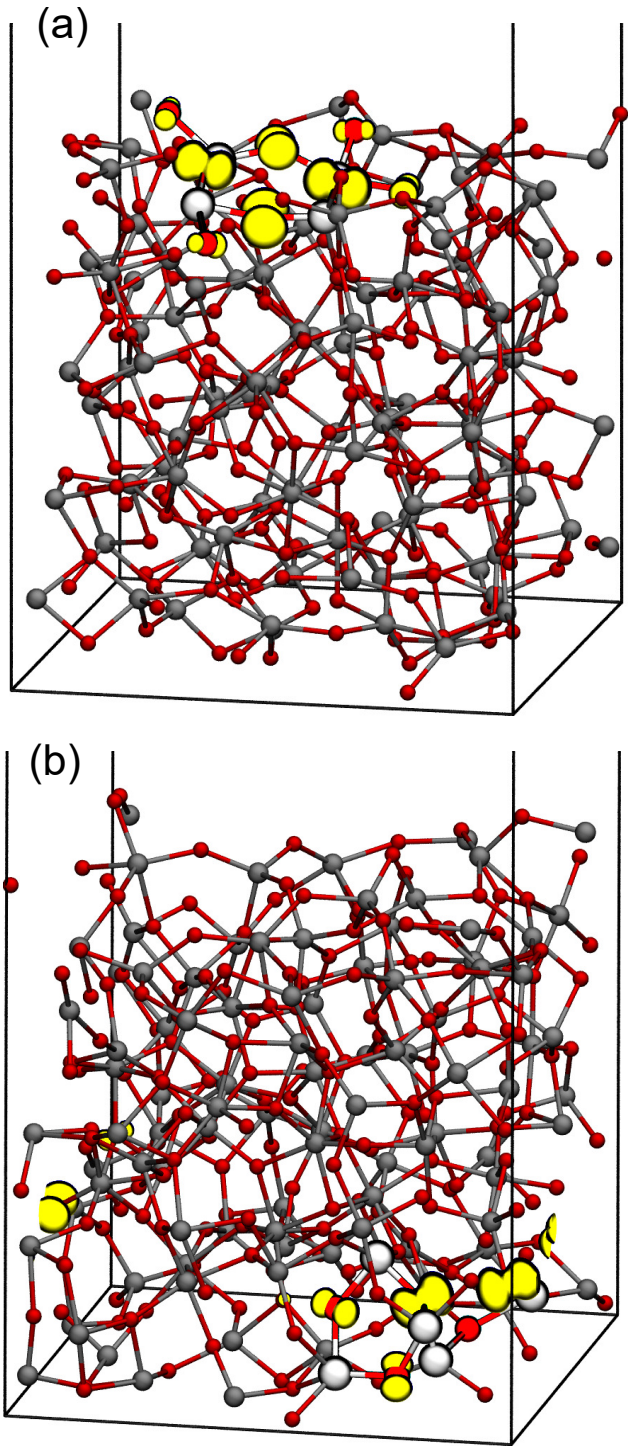

Figure 7.5: Representative orbitals of surface (a) and bulk (b) states from the periodic and surface quenches, respectively.

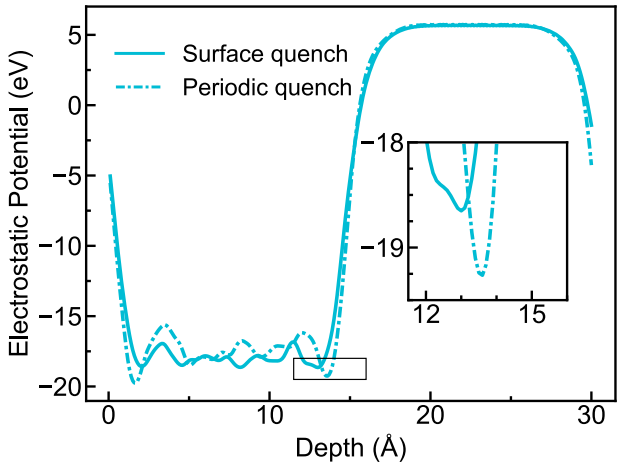

Figure 7.6: Electrostatic potential along the z-direction. Results are averaged over 10 cells for each quench condition prepared at 10 K/ps quenched cell.

S10-S12‡) predict a narrowed band gap of up to approximately 0.18 eV at all quench rates.

Quite notably, surface quenched structures predict more reduced Ti atoms at all distances below the surface than periodically quenched structures (Fig. 7.4). In all cases, electron density is concentrated away from the surface, reaching the bulk value at a depth of approximately 2.5 Å. However, periodic quenched cells predict an average Ti oxidation state that is approximately 0.01 e^- greater at all depths. Average O oxidation is correspondingly reduced for surface quenched cells, indicating more covalent character in these cells. This is indicative of very different chemistries predicted from the two surface preparation protocols.

Visualization of the charge density shows that the valence band of periodic quenched structures is the result of localized surface orbitals (Fig. 7.5(a) and Fig. S13‡). Such orbitals have been found to compose the valence band maximum of approximately 70% (Fig. S13‡) of the quenches studied here, and primarily consist of the oxygen *2p* orbitals near a $^{[5]}$Ti. For surface quenched cells, the character of these orbitals remains the same (i.e., localized clusters on O *2p* orbitals). However, these clusters occur primarily in the subsurface layers on the O (or Ti) directly under a surface Ti (or O), or in bulk states (Fig. 7.5(b) and Fig. S14‡). Such orbitals also comprise approximately 70% of the surface quenched structures studied here. However, in approximately 10% of cells prepared by both methods, the valence band maximum occurs localized around a

$^{[7]}$Ti located in the bulk away from the surface, indicating that bulk $^{[7]}$Ti should not be neglected in understanding the properties of am-TiO_2 surfaces.

The subtle differences in charge distribution between surface and periodic quenched structures would result in vastly different material interpretations if a single one of these models were used to predict the technologically relevant properties of am-TiO_2 surfaces. Indeed, the planar averaged electrostatic potential along the z-axis (Fig. 7.6) shows peaks at the surface for each of the periodically quenched cells here that differ from surface quenched cells by approximately 1 eV. This effect applies to all quench rates studied here (Fig. S15‡) and shifts the predicted ΔG° of electron-transfer processes or adsorption processes by 40 times $k_B T$.

7.3 Conclusion

This study established minimum conditions necessary for achieving experimentally accurate melt-quench derived amorphous surfaces. Specifically, it was found that unit cells smaller than $(TiO_2)_{63}$ with 12 Å lattice parameters were unable to match the experimentally determined Ti–Ti RDFs. Additionally, approximately 172 replicate quenches captures 95% of the amorphous structural motifs. Surface-quenched structures generated with these guidelines provide efficient rules of thumb for future studies attempting to understand other amorphous phase surfaces.

Furthermore, a detailed structural and electronic investigation into the effects of periodic boundary conditions when quenching am-TiO_2 has been presented. The results indicate significant differences in the predicted properties between the two methods, including more oxidized Ti atoms across the entire unit cell in surface quenched cells, alteration of the band edge character and location, and increased electrostatic potential at interfaces of surface quenched cells, resulting in significant differences in the properties predicted of the technologically relevant experimental interfaces. Critically, the structural origin of these effects are not detectable by short-range structural analysis that have been commonly used to assess the quality of an amorphous material model, such as bond length and angle distributions and RDFs. These

results demonstrate the need for increased scrutiny of melt-quench prepared surfaces, and improved structural descriptors for medium- and long-range order, including surface properties like ruggedness and coordination. Additionally, real materials possess a range of defects or dopants that likely alter structural and electronic properties. Such effects can be built into the models proposed here via atomic deletion or substitution in a quenched cell. However, more robust methods for understanding the structural relaxations that occur upon doping will likely coincide with the development of improved force fields that accurately capture the interaction between the dopant and host lattice.

The most realistic interfaces were generated via surface quenching. Interestingly, the different quench rates provide way to generate a range of surface topologies that can be compared to experimental structures. Importantly these models are a promising foundation to enable further study of amorphous surface chemistry, including for applications in molecular adsorption, catalysis, and interfacial electron transfer.

Chapter 8

Nanoparticles: Preparing Computationally Efficient TiO_2 Nanoparticle Models[†,‡]

8.1 Introduction

Nanostructured TiO_2 has received intense investigation as a catalyst or support in a wide variety of photochemical applications, including dye-sensitized solar cells [198, 199], water-splitting [200, 201] and CO_2 reduction [202, 203]. Considering this technological interest, extensive scientific effort has been spent studying the surface properties of nanostructured TiO_2 in order to achieve a fundamental understanding of the mechanisms that drive device function, as well as provide a means to tailor properties as a function of morphology. Consequently, many structurally diverse TiO_2 nanostructures, ranging from decahedral [204–206] to more complicated shapes [207–209], with vastly varying photophysical properties have been reported. Such advancement in targeted synthesis of nanoparticles with desirable properties can greatly improve device efficiency, yet a unifying model that relates nanoparticle structural features to specific electronic properties *a priori* to speed design to implementation time continues to elude researchers.

In pursuit of such ambitions, experimental study is inherently limited by the fact that ob-

[†]Portions of this chapter have been published in Repa, G.M.; Fredin, L.A. Capturing experimental properties in computationally efficient faceted titania nanoparticle models. *International Journal of Quantum Chemistry* **2023**, 123(7), e27062.

[‡]Electronic supplementary information is available at https://doi.org/10.1002/qua.27062.

servations are ensemble averages over a wide range of structural features. Thus, the problem of untangling structure-function relationships is well-suited for computational study, where quantum mechanics can predict the properties of contrived nanoparticles varying along a single structural axis, such as exposed facets or size. However, even considering recent advancements in computational infrastructure, full quantum mechanical calculations of experimentally-sized nanoparticles in the 10-100 nm range [210] is beyond what is practical with DFT. Thus, developing chemically accurate models that simultaneously capture the properties of experimentally-sized particles while residing in a computationally tractable size regime is non-trivial.

The problem is further confounded by difficulties capturing the diverse range of structural features that have been observed in real systems in such models. For example, alternative reconstructions of the anatase surface have been reported at high temperatures and pressures [211]. In particular, the stress-driven ad-molecule reconstruction (ADM) involves TiO_2 ridges formed by four-coordinated Ti and two-coordinated O on the (001) surface [212], and has received much attention recently for potentially increased photocatalytic activity. A modification to this theory, the ad-oxygen model (AOM), has since been put forward which involves adding one oxygen adatom to each 4-coordinated Ti on the ADM ridge [213]. However, the mechanism and energetics of reconstruction on periodic and nanosized systems remains under debate. Indeed, previous successes in computational modelling of TiO_2 nanoparticles have largely focused on idealized periodic surfaces [202, 214], spherical radially symmetric particles [215, 216], or Wulff-shaped particles [217], which in the case of the anatase of TiO_2 is an octahedron composed of eight {101} facets. Although such studies have done much to advance nanostructured TiO_2 technologies [218], the same understanding has yet to be extended to more complex nanostructures. In particular, particles that are characterized by known low index facets, yet not at thermodynamically ideal shapes or ratios, and hereby referred to generally as faceted nanoparticles.

Previous research to probe the structure-property relationship of faceted TiO_2 nanoparticles has largely been focused on modifications to ideal Wulff-shaped particles, either truncating or elongating the octahedra to introduce additional (001) or {010} facets respectively [219–224].

Many studies have utilized small faceted nanoparticles intended to represent larger surfaces for adsorption studies [225–228]. With regard to larger clusters, Lundqvuist et al. [229] documented the electronic properties and adsorption characteristics of variously shaped anatase nanoclusters with up to 68 TiO_2 units. Using LDA, Wang and Lewis [230] were able to study the effect of particle size and dimensions on a series of faceted particles composed of {101} and (001) facets up to 774 atoms. However, due to the computational effort required for these studies, the number of cluster shapes that can be studied are limited, and thus it is difficult to know the extent for which a particular particle model be accurately applied. To gain a better understanding of the effect of particle morpholgy on calculated properties, Gałyńska and Persson [231] successfully mapped the electronic properties of a set of 34 $(TiO_2)_n$ clusters, with sizes of anatase nanoparticles up to 122 TiO_2 units. Most of these studies draw conclusions by comparing particles with different numbers of TiO_2 units, introducing a confounding variable when attempting to attach particular properties to specific molecular geometries.

In this work, we extensively explored chemical and computational parameters by mapping the electronic and geometric properties of several different nanoshapes with identical molecular formulas ranging from 60 to 202 TiO_2 units and quantifying how different model preparations can affect calculated results to produce models that produce experimentally relevant properties. We show that perturbation of the nanoparticle crystal away from the cut crystal structure through pre-optimization with classical molecular dynamics simulations (MD) and vacancies of higher-coordinated Ti atoms can simultaneously lower computational effort, as well as produce a more delocalized electronic structure, which is critical to represent the band structures of larger experimental nanoparticles.

8.1.1 Modeling Faceted Particles

Developing models of faceted nanoparticles, which are characterized by well-defined surfaces not at thermodynamically ideal ratios or shapes, is significantly more complex than for Wulff- or spherically-shaped particles. This is a multi-pronged challenge, because not only is there a

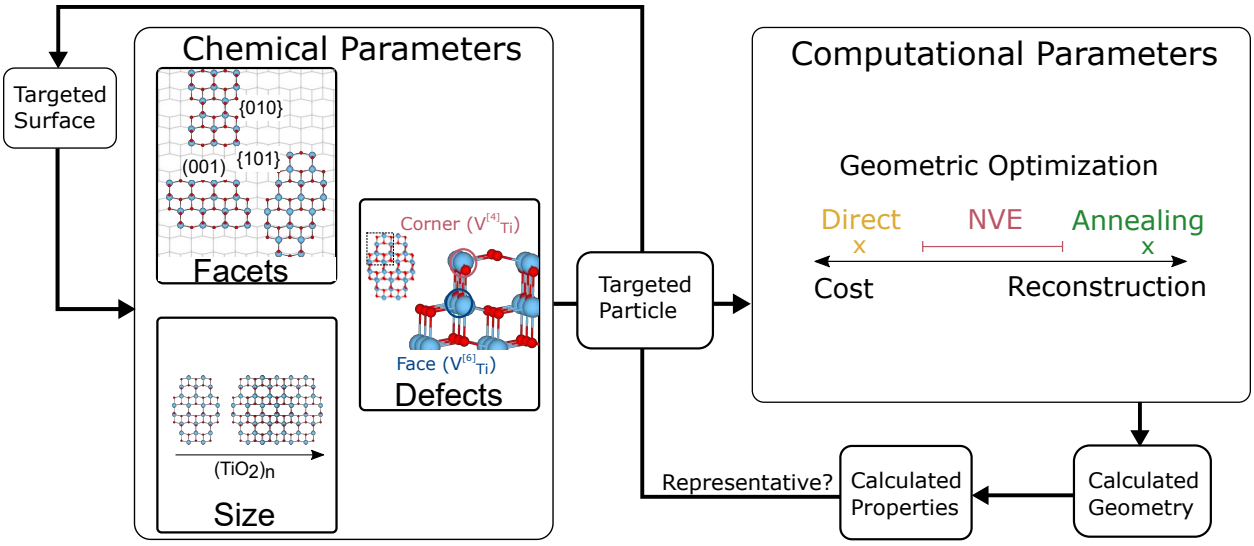

Figure 8.1: Interplay between chemical and computational choices in building faceted nanoparticle models.

much greater range of chemically valid nanoshapes that must be considered, there are also numerous modeling choices that must be made for which there is no experimental guidance. Such decisions may lead to vastly different calculated results. Therefore, careful model development like that presented here is critical to ultimately provide rationale for how to build models for future studies of faceted nanoparticles. In this section, we review the choices that must be made along with the inter-dependence of each of these choices (Fig. 8.1).

In general, nanoparticles are created through a top-down approach, which involves carving a particular nanoparticle from bulk anatase. In the case of Wulff-shaped particles, recent software developments have automated structure generation for any oxide material, and are able to produce particles with controlled stoichiometry simply given a bulk crystal structure and surface energies [232]. For faceted particles, shape is largely driven by desire to study a specific facet. The three most experimentally relevant facets for anatase TiO_2 are the (001), {101}, {010} facets, although higher index surfaces are possible [233]. When creating nanoparticles targeting a particular facet, arbitrary choices regarding the nature of the facet intersections and ratios between facets is inevitable, and thus must be accounted for when considering results between varying particles. The number of atoms feasible for quantum mechanical calculation restrict

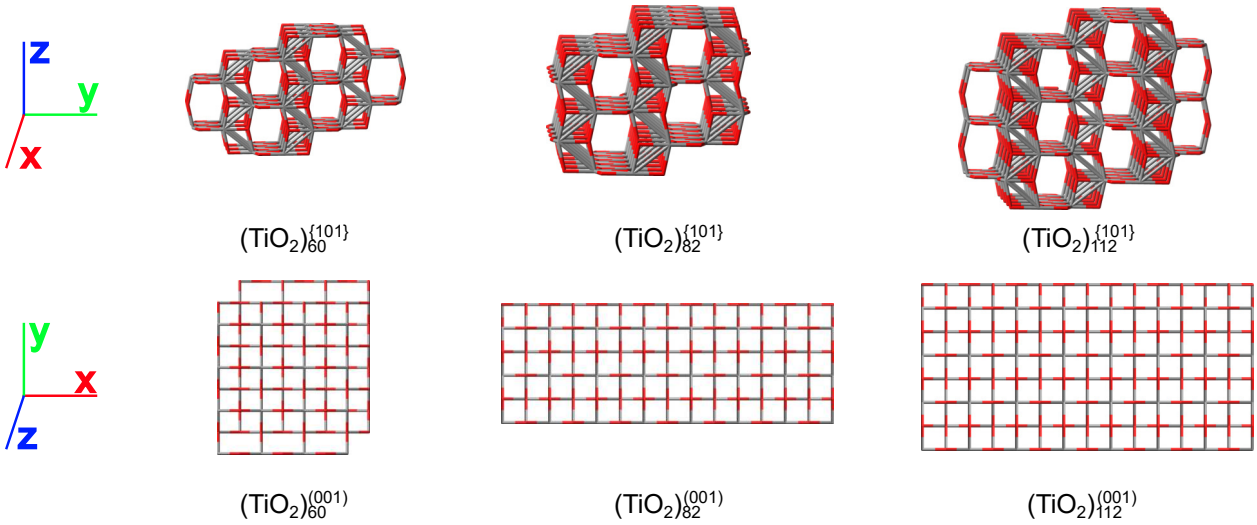

Figure 8.2: Unoptimized $(TiO_2)_n^{\{101\}}$ (top panel) and $(TiO_2)_n^{(001)}$ (bottom panel) nanoparticles.

particle sizes to only a few nm at best, which represent only the smallest nanoparticles measured in experiment. Thus, model development is further tasked with developing models that are simultaneously small enough to be amenable to DFT calculation, while being representative of larger systems.

The relationship between number of atoms comprising a nanoparticle, and emergence of size-dependent properties is not straightforward. Specifically, the shape of equivalently sized nanoparticles can be a major determinant of nanoparticle properties. Real nanoparticles are characterized by both bulk-like crystalline cores and localized surface states. Therefore, budgeting the number of atoms to achieve both core and surface regions is critical for experimentally accurate nanoparticle models. In addition to considering the surface area to volume ratio, consideration must be made for the size of a particle in an individual dimension, and whether asymmetric particles elongated in a single dimension, such as nanorods, are computationally preferable to more symmetric ones. In addition, faceted nanoparticles can be of any point group, whereas Wulff particles are d_{2h} and spherical particles are radially symmetric in all dimensions.

The type and amount of exposed facets produced by carving from the bulk will have a direct impact of stoichiometry of the resultant nanoparticle. In general, all nanoparticles other

than the ideal octahedral Wulff particle will require removal of Ti atoms in order to achieve Ti/O stoichiometry. Consequently, the choice of which Ti atoms to remove, and how to handle the resultant dangling singly coordinated O ($^{[1]}$O) must be considered. Common practice in literature until this point [219, 234, 235] has been to remove the least coordinated Ti atoms in accordance with thermodynamic intuition. We find that this approach may not be desirable for all cases. In particular, the least-coordinated atoms are often at the corners or edges of the nanoparticle. In real systems, these may be the most reactive sites [230], and therefore realistic models of TiO_2 catalysis require accurate descriptions of such sites. Furthermore, removal of Ti atoms from the corner sites tends to result in a higher number of $^{[1]}$O and their close proximity to each other at the corner of the nanoparticle may create numerical issues in early self-consistent field (SCF) interations. Alternatively 5- or 6-coordinated Ti atoms from surface sites could be removed. However, while oxygen vacancies in both bulk [236] and nano-TiO_2 [237] have been extensively studied, there is little information on Ti vacancies due to their generally high formation energy in bulk systems [238]. All of these modeling criteria can be regarded as "chemical choices" of the system, *i.e.,* generation of a molecular geometry possessing desired structural characteristics. Once the chemistry of interest has been determined, the remaining decisions are computational, mainly selecting the appropriate optimization strategy to obtain a low energy structure representative of the surface geometry and electronic structure of larger experimental particles.

Geometric optimization of molecular nanostructures represents one of the biggest challenges to the computational community at present. The potential energy surfaces for such structures are very flat and the large number of atoms makes extensive quantum calculation spanning all possible configurations to find a global minimum impossible. Numerous techniques have been applied to tackle this issue, such as optimization using genetic algorithms or Monte Carlo simulations [239], however such approaches have not proven effective for larger clusters, and rarely result in a crystalline enough structure to be considered a faceted nanoparticle. To remove barriers to energy-lowering structural reconstructions in larger particles simulated annealing

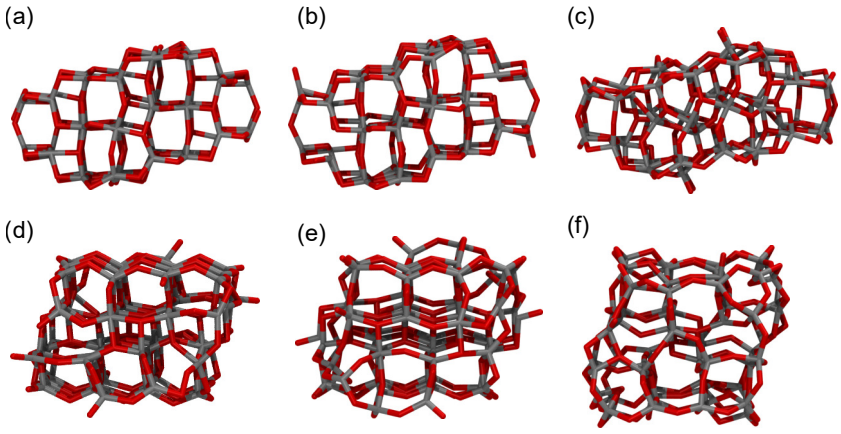

Figure 8.3: $(TiO_2)_{60}^{101}$ and $(TiO_2)_{60}^{001}$ prepared by direct (a and d), $(NVE)_c$ (b and e), and $(NVE)_f$ optimizations (c and f).

has been performed, where the nanoparticle is heated and cooled using dynamics methods. Such methods utilizing MD or tight-binding DFT methods have been ubiquitous in studying spherical nanoparticles [219, 224, 240, 241]. However, the advantages afforded by such an approach are limited for faceted nanoparticles in the size range tractable for electronic structure calculations. In particular, this size regime with faceted surfaces likely represents a meta-stable state. Therefore, as annealing methods would likely produce amorphous TiO_2 at this size, less perturbative methods, like pre-optimization using simple inter-atomic potentials [242], for nanoparticle optimization are needed. However, the complicated choice of optimization method can drastically change calculated properties [243], even if structural deviation is minimal.

For each of these choices, there is little experimental intuition to guide different model decisions. This work aims to develop a general guide for how to access nanoparticles with a large amount of either {101} or (001) facets that can be used to model larger experimental particles. This is done through a systematic evaluation of a set of inter-related nanoparticle models that probe systematic size, facets, defects, and optimization strategies with DFT or MD + DFT. These chemical and computational choices lead to different geometric and electronic effects. In particular, special considerations must be made to access particles with a large amount of (001) surface. Throughout the paper, comparisons are made across identically sized (001) and {101} particles allowing the chemistry of different shaped TiO_2 nanoparticles to be

directly probed for the first time.

8.2 Particle Models

8.2.1 Particle Facets and Size

Faceted TiO_2 nanoparticles were generated by carving various nanoshapes from bulk anatase TiO_2 (Fig. 8.2). Nanostructures with large amounts of either {101} or (001) facet and reasonable stoichiometry were selected. A discussion of particles with a significant amount of {010} facets is presented in Sec. 8.3.2. These facets comprise much of the previous research on TiO_2 nanostructures and are the three most experimentally relevant surfaces [233]. The particles are referred to as either $(TiO_2)_n^{\{101\}}$ or $(TiO_2)_n^{(001)}$ depending on the majority facet and where n = number of TiO_2 units. For both groups, nanoshapes that maximized the amount of the targeted facet were generated, and sets that possessed a partner in the opposite group with an identical number of TiO_2 units are presented here. By selecting nanoparticles with the same number of TiO_2 units but varying shapes, it is possible to isolate facet effects from size effects, while allowing for discernment between general and facet-specific guidelines for modeling different TiO_2 surfaces. All particles were carved to at least the point group C_i, a feature that eases the DFT optimization procedure. To refer to the dimensions of the nanoparticles, the coordinate system where the z-axis is the normal of the facet displaying the largest amount of targeted surface area is adopted.

The most efficient shape maximizing the targeted surface-area to volume ratio is a slab that lacks significant dimension in the z-direction while maximizing x- and y-dimensions. However, the unique chemistry of nanostructures arises as a result of the coexistence of delocalized electrons in core bulk-like regions of the nanoparticle interior with localized states located on the nanoparticle surface, as previously discussed. Indeed, it is well-understood in periodic plane-wave DFT studies of nanoparticle surfaces that substantial representation of the subsurface region is necessary to achieve reliable results [244, 245]. Similar effects can be expected for

the discrete nanoparticle models studied here, *i.e.,* all three dimensions must be significantly large while simultaneously limiting the number of atoms to be computationally tractable. This is systematically tested in the current study to understand whether it is better to spend the atom budget on developing larger surface areas or core bulk regions. Thus for the {101} particles, we selected three different particles with different sizes (60, 82, and 112-TiO_2 units). Comparing the 60- and 82-unit particles represents an increase in primarily the x- and y- directions of the slab with dimensions 11 x 17 x 9 Å and 19 x 13 x 9 Å for $(TiO_2)_{60}^{\{101\}}$ and $(TiO_2)_{82}^{\{101\}}$, respectively. Comparing the 82 and 112 unit particles represents a change primarily in the z-direction with dimension of 15 x 17 x 13 Å for $(TiO_2)_{(112)}^{\{101\}}$. In the language of periodic slab studies, the smallest two of these nanoparticles are 3 layers thick, while the larger particle is 4 layers thick. For the $(TiO_2)_n^{(001)}$ particles, particle size is primarily controlled by varying the x-, and y-dimensions to produce particles with 13 x 15 x 8 Å, 9 x 26 x 8 Å and 13 x 26 x 8 Å dimensions for $(TiO_2)_{60}^{(001)}$, $(TiO_2)_{82}^{(001)}$, $(TiO_2)_{112}^{(001)}$ respectively. Unoptimized geometries of each of the carved particles studied in this section are available in Fig. 8.2. A more thorough discussion on the effect of number of layers for $(TiO_2)_n^{(001)}$ particles is presented in section 8.3.2.

8.2.2 Particle Defects

In the case of the faceted nanoparticles studied here, creation of stoichiometric nanostructures involves deletion of extra Ti atoms from the anatase surface to create Ti vacancies (V_{Ti}). In general, the $(TiO_2)_n^{(001)}$ particles require deletion of more Ti-sites to achieve stoichiometry (Table S1‡). To test the effect of deleted Ti atom location and chemistry on the calculated properties and reconstruction, two different sites on each nanoparticle were selected: 3-coordinated Ti ($^{[3]}$Ti) atoms at the corners of the nanoparticles at the intersection of two {101} and one (001) surfaces (red dots in Figs. S1 and S2), and $^{[6]}$Ti on the {101} surface (blue dots in Figs. S1‡ and S2‡). These two locations were chosen as they represent the least and most disruptive locations for Ti vacancies based on typical thermodynamic intuition, and an intermediate choice would've been to delete the $^{[5]}$Ti from the {101} surface. Each particle was then subjected to a brief NVE

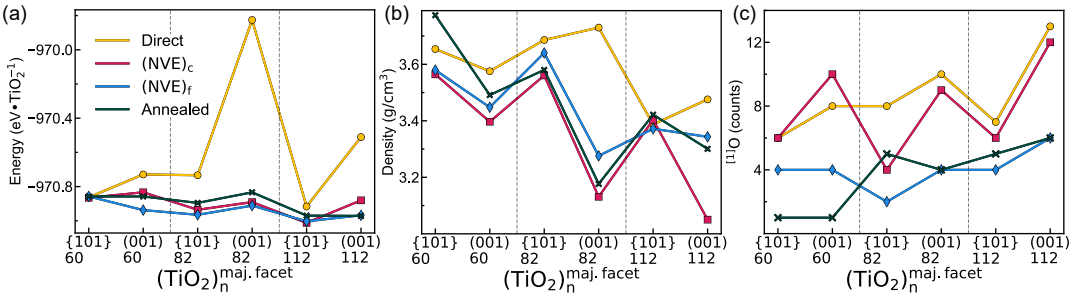

Figure 8.4: Optimization energy (a), density (b) and number of $^{[1]}$O (c) for $(TiO_2)_n^{\{101\}}$ and $(TiO_2)_n^{(001)}$ nanoparticles. The gray lines divide the data points by number of TiO_2 units. The x-axis labels reference the particle shape (maj. facet) and number of TiO_2 units, n. Optimization energies are listed in Table S2‡

(see definition below) MD simulation followed by a DFT optimization. These particles are referred to as $(NVE)_x$ where x = c or f depending on whether the Ti atoms were removed from the corner or the face, respectively.

8.2.3 Computational Approach

To perform a comparison of the various methods that have been used to model nanoparticles before, as well as control how much of the potential energy surface is explored, we adopted several different protocols for nanoparticle optimization. The simplest method here involves directly submitting the cut nanoparticle for DFT optimization. Such an approach explores the least amount of potential energy landscape associated with a particular guess structure, and in general, represents the most computationally expensive of the methods utilized here. In particular, these structures are highly prone to charge sloshing during early SCF cycles, and often require generating an initial guess wavefunction for the DFT optimization using Hartree-Fock. Applying a random displacement to each atom of up to 0.12 Å in any direction can lead to marginal improvement in SCF convergence during early iterations. All DFT calculations were preformed using Gaussian16 [246] with default settings. The B3LYP exchange-correlation functional [247] coupled with the effective-core potential basis set proposed by Boutelier [248], which is of double-zeta quality and provides an 18-core-electron pseudopotential for Ti atoms

was used. This setup has been previously shown to produce acceptable results for faceted TiO_2 nanoparticles [229, 231]. The widely used general functional B3LYP was selected as it can be easily extended for modeling of adsorbates to the nanoparticle without the confounding variable of switching functionals, as opposed to methods that have been more parameterized for nanostructured TiO_2. All direct optimizations were performed using particles with corner V_{Ti} described above.

To explore a larger region of the potential energy surface than that afforded by direct optimization, we tested pre-optimization with MD. A positive side effect of such approaches is that a structure closer to the energetic minimum may be used as the guess geometry for the quantum mechanical optimization, thus possibly reducing the computational cost. Such approaches using MD pre-optimizations to cheapen DFT calculations have been extensively compared and discussed before [242]. However, the primary goal of the pre-optimizations in the current work was not intended to reduce the number of DFT geometry optimization steps by matching the lowest energy structure, but rather to explore degrees of particle surface reorganization beyond that accessible to the direct optimization with DFT. The computational savings seen were primarily due to fewer SCF cycles required to reach convergence in early geometric iterations rather than less DFT optimization steps. As previously discussed, an important trade-off emerges when utilizing such methods to balance energy lowering reconstructions while retaining enough of the morphology of the cut nanoparticle such that the targeted faceted surface is well-represented.

In order to create minimal perturbation in the structure, each particle was briefly run in the micro-canoncial ensemble (NVE) that is characterized by constant energy over each microstate. This should relieve the highly strained regions of the cut nanoparticle without causing too much perturbation to the overall structure. This small pre-optimization was able to remove the numerical instabilities associated with the direct optimiziation, reducing computational cost and allowing us to access a wider number of particles that failed to optimize in DFT. These NVE runs were performed in LAMMPS [187] using the Matsui-Akaogi potential [186] for TiO_2 with a 10 Å cutoff to the coulombic contribution of the potential. Each particle geometry

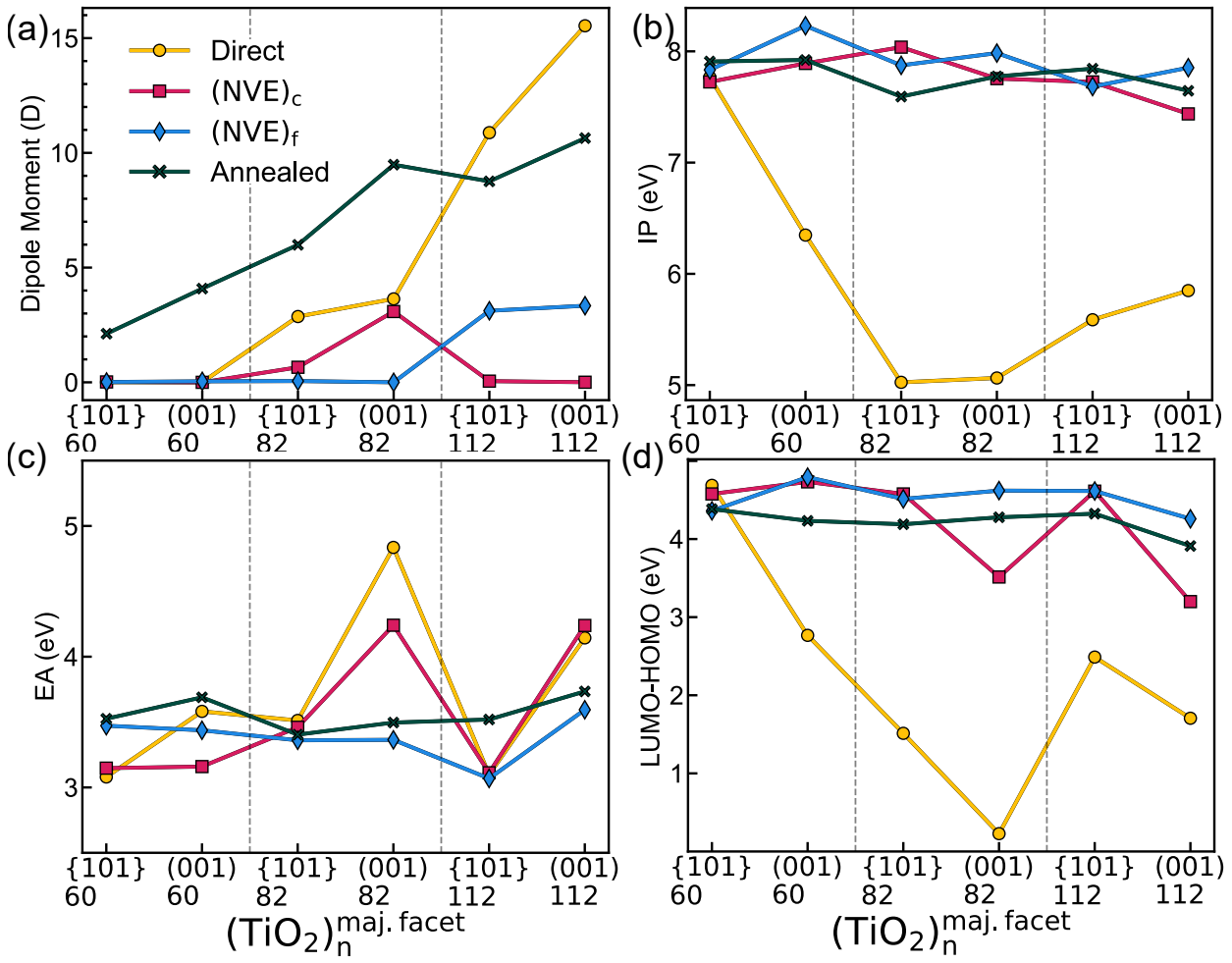

Figure 8.5: Dipole Moment (a), IP (b), EA and LUMO-HOMO (c) for $(TiO_2)_n^{\{101\}}$ and $(TiO_2)_n^{(001)}$ nanoparticles. The gray lines divide the data points by number of TiO_2 units. The x-axis labels reference the particle shape (maj. facet) and number of TiO_2 units, n. These values are listed in Tables S6‡, S7‡, and S8‡ respectively.

was first minimized in a non-periodic shrink-wrapped box until the maximum force on each atom was $1.0x10^{-3}$ kcal/mol-Å. This was then followed by a brief 10 ps NVE run with a 0.1 fs timestep. The resultant structure was then symmeterized to the point group of the original cut particle (C_i) using GaussView [249], and then freely optimized using the DFT method described above. However, unlike the cut particles, symmetry was applied to the initial guess and enforced during early geometry optimization cycles. In later optimization steps, particles were permitted to break symmetry.

The most aggressive approach to nanoparticle preparation that should allow exploration of the entire nanoparticle potential energy surface is through simulated annealing. Such methods have largely been applied to generate amorphous phases from bulk crystalline solids [151, 154]. To serve as a baseline for complete amorphicity, and thus the direct opposite of the ideal faceted particles, we additionally heated each of the cut nanoparticles. Annealed particles were prepared using the same MD potential and timestep as the NVE runs, and started from the NVE output. Each structure was heated from 800 K to 2000 K in a NVT ensemble over 5 ps. The system was then allowed to evolve for 100 ps at 2000 K, followed by cooling over 10 ps to 300 K. The resultant structure was then submitted for full DFT optimization as previously described. We subjected each of the nanoparticles in the (001) and {101} groups to all of these optimization protocols to quantify the balance between ease of optimization and retaining models of the desired surface. We refer to the nanoparticles resulting from each of these preparations as either directly optimized, $(NVE)_{c/f}$, or annealed in order of increasing aggressiveness.

8.3 Results & Discussion

8.3.1 (001) vs. (101) Nanotitania Models

Geometric Effects

Optimized geometries for $(TiO_2)_{60}^{\{101\}}$ and $(TiO_2)_{60}^{(001)}$ nanoparticles are available in Fig. 8.3 (optimized geometries for all $(TiO_2)_n^{\{101\}}$ and $(TiO_2)_n^{(001)}$ particles studied here are available

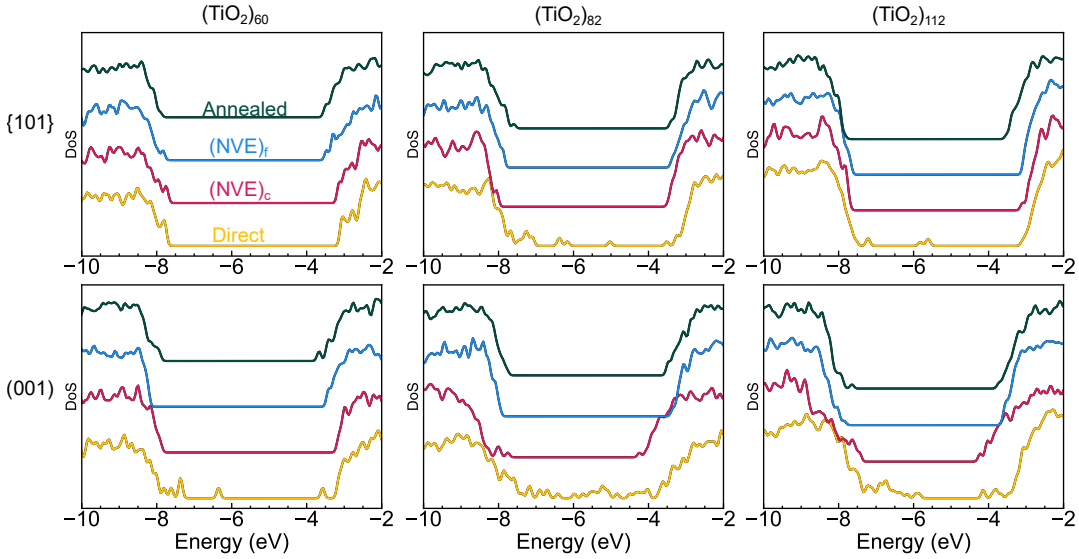

Figure 8.6: DoS for each $(TiO_2)_n^{\{101\}}$ and $(TiO_2)_n^{(001)}$ particle studied here.

in Figs. S1‡ and S2‡ respectively). Qualitatively, it is apparent that there is more disorder for each increasingly aggressive particle preparation. This fact is most exaggerated for the $(TiO_2)_n^{(001)}$ particles, likely due to the greater instability of the (001) facet [221], unstable corner and edge structures, and highly asymmetric dimensions of these particles. Indeed, many of the $(NVE)_f$ $(TiO_2)_n^{(001)}$ particles bear little resemblance to their starting geometries. Conversely, reconstruction in the $(TiO_2)_n^{\{101\}}$ is less dramatic, with reorganization of the majority of the non-annealed particles being limited to the region surrounding V_{Ti}. Even such qualitative analysis reveals that different computational considerations are necessary depending on the majority exposed facet and shape.

In general, direct optimization of the nanoparticles results in a higher energy structure opposed to those that have been treated with any MD method (energy per TiO_2 unit: Fig. 8.4a and Table S2‡). Among the directly optimized particles, there is significant energetic differences between same-sized $(TiO_2)_n^{\{101\}}$ and $(TiO_2)_n^{(001)}$ of 8.0 eV, 74.4 eV, and 45.5 eV for 60-, 82-, and 112-unit particles respectively. The $(NVE)_c$ particles retain this trend with energetic separation between the respectively sized $(TiO_2)_n^{\{101\}}$ and $(TiO_2)_n^{(001)}$ 1.9, 3.7, and 14.8 eV. Both $(NVE)_f$ and annealed particles are less sporadic in the calculated energies. In general, increasing energetic

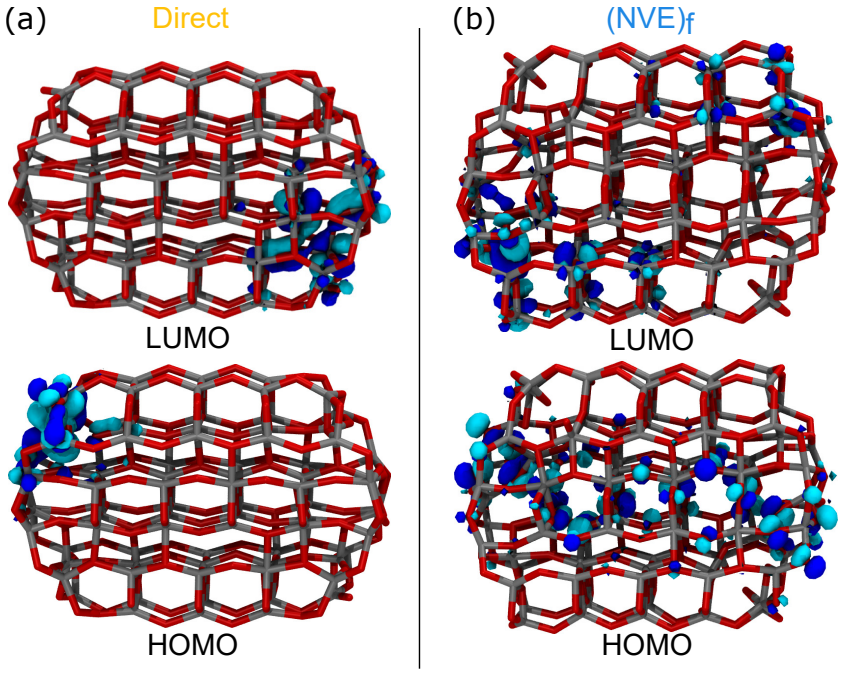

Figure 8.7: Frontier orbitals for directly optimized (a) and $(NVE)_f$ (b) $(TiO_2)_{82}^{\{101\}}$

separation for same-sized (001) and {101} particles could be the result of increasingly developed core bulk regions in the former. The exceptionally high separation between $(TiO_2)_{82}^{\{101\}}$ and $(TiO_2)_{82}^{(001)}$ structures could possibly be attributed to the dipole moment of such an asymmetrical particle or due to the low spatial separation between corner $^{[1]}O$. The consequences of these is a high degree of internal strain. Therefore the directly optimized $(TiO_2)_{82}^{(001)}$ is likely not a physical structure. This analysis, combined with lack of significant structural differences between the directly optimized and $(NVE)_c$ particles suggests that preparing particles with $(NVE)_c$ may be the ideal way to achieve models that lack the high-energy corner and edge structures while retaining largely ideal facets and no homogenization of properties.

It is notable that the most energetically favorable particles studied here are the $(NVE)_f$ particles, rather than the annealed or $(NVE)_c$ particles. Previous experimental [250] and theoretical [219] investigations have suggested approximately 2 nm as a lower limit for favorability of formation of a crystalline core in a model, which is approximately twice the size of the largest particles studied here. A possible reason for this discrepancy is the the shape of the annealed particles studied here, which possess similar dimensions of their crystalline counterparts. Most

previous studies have focused on spherically cut annealed particles, which possess a much lower proportion of destabilizing surface atoms than those in the current study. A quantification of the sphericity [251] of each nanoparticle is available in Fig. S3‡. An additional source for this discrepancy could be related to the cooling rate utilized in the MD simulations. It is well-known that cooling rate will have a direct effect on the calculated geometry [240], however a systematic comparison of different cooling rates is beyond the scope of this work. Additional analysis of the density of each nanoparticle, calculated from Van der Waals surface of the nanoparticle (with r_{Ti}=1.76 Å and r_O=0.48 Å) confirms each of the nanoparticles studied here is far from bulk-like (Fig. 8.4b) with calculated densities far below the bulk anatase value of 3.90 g/cm^3. Such density lowering has been observed in amorphous particles of approximately 2 nm to have density of lowering to 3.70 g/cm^3 [250], indicating that all of these particles do not have significant core regions.

Inspection of reconstruction around the Ti vacancies of the particles reveals a number of dangling $^{[1]}$O. These regions may be critical to the electronic properties of the nanoparticle, providing favorable locations for charge localization. Furthermore, lack of reorganization in this region may lead to the increased energy of directly optimized particles. Therefore, the number of $^{[1]}$O in each optimized particle is quantified (Fig. 8.4c). In the unoptimized structure, each corner V_{Ti} creates two $^{[1]}$O, while each face vacancy only results in one. The corner vacant particles (*i.e.,* directly optimized and $(NVE)_c$) possess a higher number of $^{[1]}$O. Differences in the structure around V_{Ti} between these two groups can be attributed to the fact that $^{[1]}$O in the directly optimized particles simply move to occupy the Ti vacancy location, forming a very sharp approximately 46° O–Ti–O bond angle. In the $(NVE)_c$ particles, this under-coordinated oxygen moves towards the neighboring Ti atom. The previous oxygen occupying this position is moved down to coordinate with the next-nearest neighbor Ti atom (Fig. S4‡). The appearance of the approximately 46° O–Ti–O bond angle is the only systematic difference apparent in any of the bond length or angle distributions (Figs. S5-7‡ and Tables S3-5‡). The higher values of $^{[1]}$O in $(TiO_2)_n^{(001)}$ particles compared to $(TiO_2)_n^{\{101\}}$ particles of respective size is likely simply a result

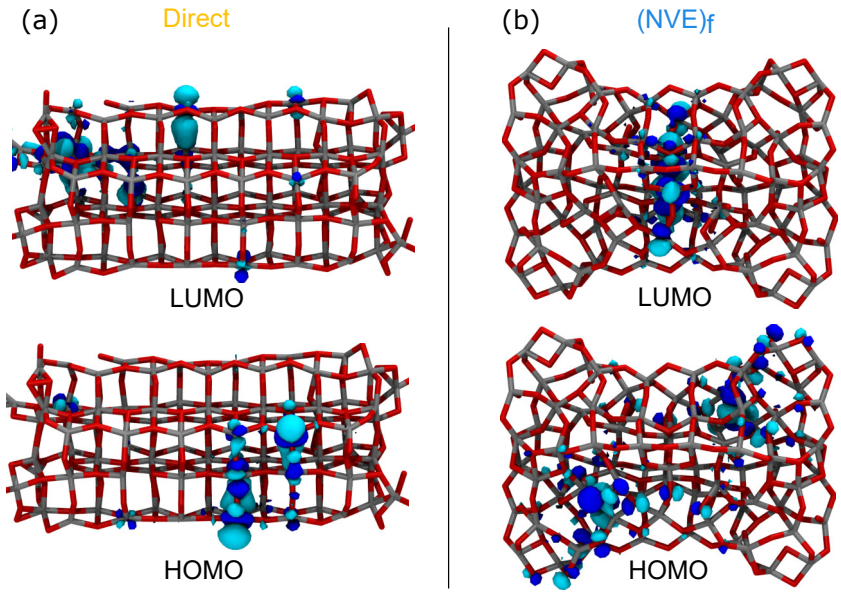

Figure 8.8: Frontier orbitals for directly optimized (a) and $(NVE)_f$ (b) $(TiO_2)_{82}^{(001)}$

of removing more Ti atoms to maintain stoichiometry, which is an additional source of increased reorganization. Coordination statistics for Ti atoms (Fig. S8‡) show that the majority of species to be $^{[5]}$Ti. This indicates that surface Ti atoms are the dominant species, and even the bulkiest $(TiO_2)_{112}^{(001)}$ particle studied here is insufficient to develop a core bulk-like region geometrically. It is notable that with each increasingly aggressive preparation scheme, the average Ti atom coordination number is decreased, resulting in 5.0, 4.9, 4.8, 4.8 for direct, $(NVE)_c$, $(NVE)_f$ and annealed particles, respectively. Such trends after annealing procedures have been reported previously [219], suggesting that creation of more surface $^{[4]}$Ti through annealing may be a viable way to increase the reactivity of a nanoparticle.

Electronic Effects

Among all electronic properties, the dipole moment can potentially give insight into the subtle geometric differences between the different particle preparations. In terms of practical applications, it is directly relevant for properties such as nanoparticle aggregation [252, 253], and has long been considered an indicator of the nature of a nanocrystal model [235]. Fig. 8.5a shows that generally both $(NVE)_{c/f}$ prepared particles do not possess a substantial dipole moment,

with small exceptions occurring for the 82- and 112-unit particles. This dipole contrasts with the annealed and directly optimized particles which both possess an increasingly large dipole moment with particle size. We attribute the higher dipole moment in the former as an effect of electron traps that may form in the amorphous material [154]. The large dipole moment in the directly optimized particles is more anomalous as structural deviation from the $(NVE)_c$ particles is minimal. Generally, this can be interpreted as an indication of the formation of localized orbitals around highly unstable surface structures. Indeed, if such is the case then the $(NVE)_c$ preparation is producing a more bulk-like particle than that of the directly optimized. Further characterization of the electronic structure is carried out in the context of Koopmans' Theorem, which allows extraction from DFT parameters that can be directly measured by experiment. Specifically, the ionization potential (IP) and electron affinity (EA) are defined as:

$$IP = -E_{HOMO}, EA = -E_{LUMO}$$

Although due to the well-known "band-gap" problem of DFT, quantitative agreement between the values calculated here and past experimental results should be interpreted with caution. The directly optimized particles predict a wide range of IPs varying over approximately 3 eV, reaching a minimum with the $(TiO_2)_{82}^{(001)}$ (Table S6‡). The $(NVE)_{c/f}$ and annealed particles do not show this same variation, and produce much better agreement with IP calculated in previous DFT studies [231, 234]. There is similar variation among the different preparation methods in the plot of EA. However, unlike in the IP values, $(NVE)_c$ prepared particles do a better job at reproducing the trend calculated for the directly optimized particles. Specifically, there is a large difference between the directly optimized $(TiO_2)_n^{\{101\}}$ and $(TiO_2)_n^{(001)}$ particles of 0.5, 1.3, 1.0 eV for n = 60, 82, and 112 units, respectively. The $(NVE)_c$ prepared particles predict separation of 0.8 and 1.1 eV for $(TiO_2)_{82}^{\{101\}}$ with $(TiO_2)_{82}^{(001)}$ and $(TiO_2)_{112}^{\{101\}}$ with $(TiO_2)_{112}^{(001)}$, respectively (Table S7‡).

These patterns in IP and EA naturally manifest in the LUMO-HOMO gaps, which perhaps

provide the best insight into different electronic characteristics among the different preparations. This value is quite erratic for the directly optimized particles, reaching near metallicity for the $(TiO_2)_{82}^{(001)}$ particle (Table S8). Previous DFT calculations have predicted similar results for comparably shaped nanostructures, such as the nanoribbons studied by Lino et al. [254] However, this is a critical sign that direct optimization of nanoparticles in a computationally tractable size range is insufficient for preparing nanoparticle models representative of larger structures. Across the $(NVE)_c$ prepared particles, $(TiO_2)_n^{\{101\}}$ particles in general predict a smaller LUMO-HOMO gap than respectively sized $(TiO_2)_n^{(001)}$ particles. The facet-dependence of LUMO-HOMO gap is mostly removed for the $(NVE)_f$ and annealed particles, however the latter continues to predict an approximately 0.4 eV larger LUMO-HOMO gap.

For further insight into nature of the band edges, the Inverse Participation Ratio (IPR) is calculated for each orbital. This metric has been commonly employed to investigate amorphous materials in planewave DFT calculations [154], and can be regarded as a measure of the localization of a particular molecular orbital. We adapt the IPR to the suit the atom-centered basis set employed in the current study for the i^{th} molecular orbital ψ_i as:

$$IPR(\psi_i) = \frac{\phi_j^4}{(\psi_i^2)^2}$$

Where ϕ_j is the sum of absolute values of the basis set coefficients contributed by the j^{th} atom and ψ_i is calculated by the sum of the absolulte values of all the basis set coefficents of the particle molecular orbital. Therefore, a higher value in the IPR plot indicates a greater degree of density localization, with a value of one meaning that the entire Kohn-Sham orbital is contributed by the basis set of a single atom. Such an analysis allows quantitative identification of the nature of frontier orbital and intra-bandgap defect states.

The results from the IPR analysis (Fig. S9‡) reflect the erratic nature of the orbital energy trends (Fig. 8.5). The large decrease in the ionization potential for the directly optimized particles is caused by a number of highly localized defect states in the band gap. States of

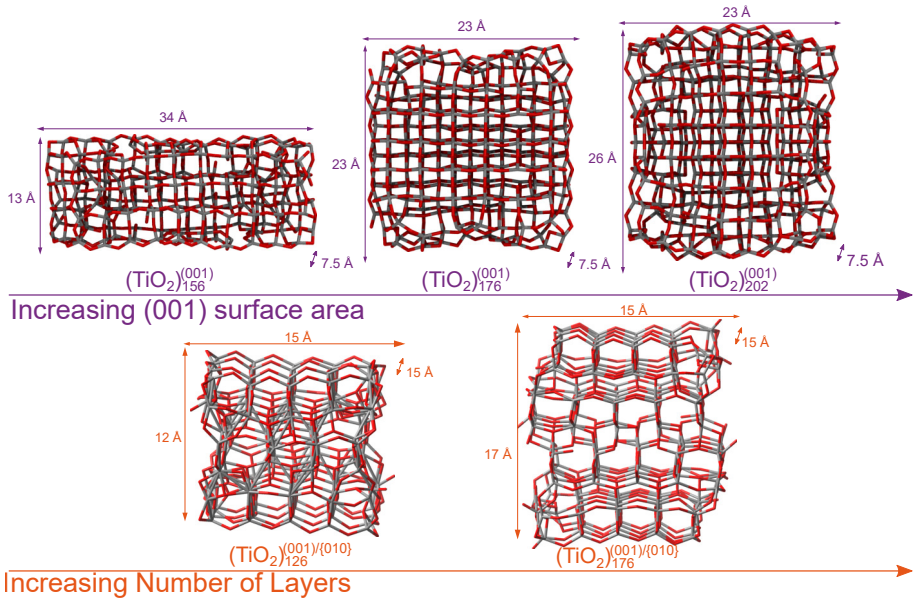

Figure 8.9: Larger $(TiO_2)_n^{(001)}$ and $(TiO_2)_n^{(001)/\{010\}}$ optimized particles. The former are characterized by an increase in the exposed (001) surface area, while the latter are characterized by increased bulk regions.

this nature comprise HOMO and LUMO for the large 82- and 112-unit particles, indicating that removal of such states cannot be accomplished simply by increasing particle size. These states lead to significant disruption of the defined valence and conduction bands, clearly evidenced in the density of states profile (DoS) (Fig. 8.6). In general, both $(NVE)_c$ and $(NVE)_f$ preparations help in some degree to remove these intra-bandgap defect states. However, particles with the $(NVE)_c$ preparation still show some propensity for formation of localized states on the edge of the valence band, particularly notable in the $(TiO_2)_{82}^{(001)}$ and $(TiO_2)_{112}^{(001)}$ particles. The more disordered structures created by annealing and $(NVE)_f$ preparation result in more delocalized bulk-like electronic structures.

Frontier molecular orbitals (all particles and optimization methods are available in SI‡, Figs. S17-39‡) confirm the IPR analysis of the nature of intra-band and band edge states. Interestingly, when the direct optimization procedure predicts a significantly delocalized electronic structure, the $(NVE)_{c/f}$ preparations do little to change the locations of the frontier orbitals. Rather, the location of frontier orbitals appear to depend largely on facet intersections cut into the original structure. However, in the cases where direct optimization predicts numerous intra-band gap

defect states, $(NVE)_{c/f}$ can drastically change the nature of the frontier orbitals. For example, the density in the directly optimized $(TiO_2)_{82}^{\{101\}}$ (Fig. 8.7a) is largely focused on the edges of the nanoparticle at the {101}|{101} facet intersection. These intra-band gap defect states are largely composed of highly localized Ti *d* orbitals on the nanoparticle surface. The $(NVE)_f$ $(TiO_2)_{82}^{\{101\}}$ (Fig. 8.7b) conversely shows much more delocalization of the frontier orbitals, with large regions of density of the edges of the nanoparticle. Thus, the extensive reconstruction induced by $(NVE)_f$ preparation is successful at removing many of these defect states allowing some of the density to shift to the core of the nanoparticle. A similar effect is observed in the directly optimized and $(NVE)_f$ $(TiO_2)_{82}^{(001)}$ particle (Fig. 8.8a and b). Although the shape achieved in Fig. 8.8b is remarkably similar to "dog-bone" shaped structures that have been previously observed experimentally [208], there is a significant amount of reconstruction required to achieve a substantially delocalized electronic structure in this particle. In such cases, the geometric changes likely render the surfaces unrepresentative of the target facet. Therefore, the next section discusses alternative nanoparticle morphologies with large regions of (001) facet in order to study particles that possess a substantially delocalized electronic structure without high degrees of surface reorganization.

8.3.2 Mitigating reconstruction for (001) particles

There are two ways to alter the amount of reconstruction of the (001) surface by modification of the morphology of the particle (Fig. 8.9). The first involves increasing the number of "subsurface" layers in the z-dimension. This is similar to the approach used in planewave calculations of TiO_2 surfaces where one of the relevant structural parameters is the thickness of the slab. In doing so, additional facets are introduced to the nanoparticle, but the area spanned by the (001) surface is unchanged. We created two of these particles with 126- and 176-TiO_2 units and dimensions of 15 x 15 x 12 Å and 15 x 15 x 17 Å with 6 and 8 layers, respectively. These particles are named $(TiO_2)_n^{(001)/\{010\}}$ to emphasize the creation of an additional facet. An alternative approach is to maintain the slab thickness in the z-direction, and increase the

area of the (001) surface in x- and y-dimensions, as was done with the $(TiO_2)_{60}^{(001)}$, $(TiO_2)_{82}^{(001)}$, and $(TiO_2)_{112}^{(001)}$ particles. Additional particles with sizes 13 x 34 x 8 Å, 23 x 23 x 8 Å, 26 x 23 x 8 Å and 156-, 176-, and 202-TiO_2 units, respectively, were created. Both methods result in a significant increase in the number of atoms. Comparing both methods will allow the most efficient way to model (001) majority particles with least computational expense to be determined. All particles were prepared with the $(NVE)_f$ protocol, with the exception of $(TiO_2)_{176}^{(001)}$ which possess corner vacancies as opposed to face vacancies. Due to the large sizes of the nanoparticles considered in this section and thus large separation of V_{Ti}, the corner vacancies have a reduced effect on the properties.

To quantify the amount of geometric reconstruction of the (001) facet, the Ti–O–Ti bond angles were measured, as these are the primary reconstruction seen on the (001) surface, as opposed to distortion of individual Ti–O octahedra, which would be detectable in the Ti–O bond lengths or O–Ti–O bond angles. The ideal (001) anatase surface would possess a single O–Ti–O bond angle peak at approximately 156°. For the $(TiO_2)_n^{(001)}$ particles, this bond angle distribution is fairly constant (purple lines in Fig. 8.10a) as particle size increases. However, none of the particles capture a single peak. For the $(TiO_2)_n^{(001)/\{010\}}$ (orange lines in Fig. 8.9a) particles, the 176-unit particle shows two very sharp peaks at approximately 125° and 140°. The significant decrease in the Ti–O–Ti angle in all samples compared to the ideal crystal value is due to arching of the bridging O upwards on the surfaces. The sharpness of the peaks in the $(TiO_2)_n^{(001)/\{010\}}$ particles compared to the $(TiO_2)_n^{(001)}$ particles that indicates that increasing the number of subsurface layers is a more efficient way of reducing (001) surface reconstruction and preparing particles with large regions of this facet.

The (001) anatase facet is known to reconstruct under high temperature and pressure conditions. The ADM and AOM are proposed models for understanding this behavior, however their appearance under other conditions remains to be documented. In the current simulations, we do not observe either of these reconstructions of the (001) facet. A recurring edge reconstruction which resembles the peroxo bridging oxygens of the AOM reconstruction is present in almost

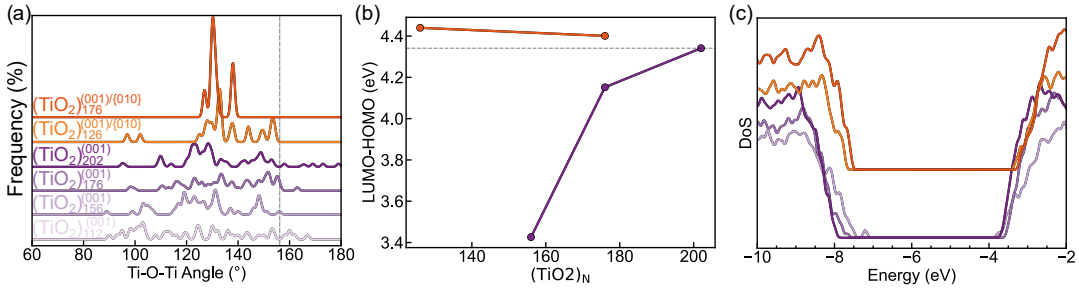

Figure 8.10: Ti–O–Ti bond angles of the (001) surface (a), LUMO-HOMO gap (b) and DoS (c) for larger $(TiO_2)_n^{(001)}$ and $(TiO_2)_n^{(001)/\{010\}}$ particles. These values, along with the energy per atom, are listed in Table S9‡.

all of the (001) structures studied here. Specifically, $^{[1]}$O near V_{Ti} face vacancies bridge two titanium atoms (Fig. S10‡). However, the calculated bond lengths for this reconstruction significantly deviate from those calculated in the AOM model. Motifs similar to that observed in the current work have been previously reported as a common occurrence in disordered TiO_2 [154]. Nonetheless, the conditions under which similar reconstructions occur in nanoscale systems requires further investigation. The LUMO-HOMO gap for the two $(TiO_2)_n^{(001)/\{010\}}$ particles is fairly consistent at 4.4 eV (Fig. 8.10b). There is a reduction in the LUMO-HOMO gap for the $(TiO_2)_n^{(001)}$ particles that gradually converged to the $(TiO_2)_n^{(001)/\{010\}}$ value, calculated at 3.4 eV, 4.2 eV and 4.3 eV for $(TiO_2)_{156}^{(001)}$, $(TiO_2)_{176}^{(001)}$, $(TiO_2)_{202}^{(001)}$, respectively. The DoS (Fig. 8.10c) shows that this reduction of band gap is related to bleeding of the valence band edge in the$(TiO_2)_{156}^{(001)}$ and $(TiO_2)_{176}^{(001)}$, which eventually disappears as the band gap approaches its limit. There is also significant red-shifting of the valence band edge in the $(TiO_2)_n^{(001)}$ particles. The IPR analysis does not predict significant differences in the nature of the orbitals comprising the band edges (Fig. S11‡). However, for $(TiO_2)_{126}^{(001)/\{010\}}$, HOMO is located on the {010} surface O *2p* orbitals, while LUMO is delocalized in the subsurface layer below the (001) facet (Fig. S12‡). Conversely, the HOMO for the $(TiO_2)_{176}^{(001)/\{010\}}$ particle is located in the nanoparticle core and the LUMO is a defect state that occurs on the (001)/{010} intersection (Fig. S13‡). Conversely for the slabs, HOMOs localize along the edges or corners on the surface layer for each of the particles studied here, while LUMOs localize in a similar area, but in the subsurface layer of the

nanocrystal (Figs. S14-16). Thus, generating particles with core bulk-like regions as opposed to large surface areas is more efficient for generating a more delocalized electronic structure.

8.4 Conclusion

Overall, this research demonstrates the care that must be taken when designing oxide nanoparticle models. By performing full quantum chemical optimization and characterization on a range of structurally inter-related nanoparticles, this research provides rationale behind selecting various design choices, including particle shape, size, defects, and optimization procedure, for particle models. These design principles are only generalizable due to the removal of confounding variables like chemical formula and shape. This chapter represents the first direct study of size and shape on TiO_2 nanoparticle properties. Taken altogether, the results of the energetic, geometric, and electronic analysis indicate that the $(NVE)_f$ preparations balance maintaining the geometric characteristics of experimental faceted particles, while removing high energy surface reconstructions that result in difficult optimization, and thus providing a reasonable electronic structure and more thermodynamically favorable particle.

Specifically, for the $(TiO_2)_n^{\{101\}}$ particles, direct optimization with DFT leads to highly strained surfaces that are responsible for the large number of defect states found in the DoS and IPR analysis, making them unrepresentative of experimentally sized systems. Pre-optimization that allows traversal of more of the potential energy surface than DFT optimization alone is needed to push a cut structure away from a strained local minima to a more useful structure. Interestingly, the $(NVE)_f$ preparation produces more bulk-like and energetically favorable particles than $(NVE)_c$ in the $(TiO_2)_n^{\{101\}}$ particles without approaching amorphous behavior, in contrast to current practice in model design to remove the least coordinated Ti atoms first. However, for $(NVE)_f$ particles properties like the LUMO-HOMO gap begin to show convergence for differently shaped nanoparticles, indicating that this preparation removes property-defining structural features. There appears to be little effect on the size and surface-bulk ratio when comparing among

$(TiO_2)_{60}^{\{101\}}$,$(TiO_2)_{82}^{\{101\}}$,$(TiO_2)_{112}^{\{101\}}$, which suggests that larger {101}-majority nanoparticles may not be necessary to produce results that can be safely extrapolated to experimentally-sized particles.

The same modeling criteria is not entirely extendable to the $(TiO_2)_n^{(001)}$ set of particles. Indeed, direct optimizations of such particles are more highly prone to unphysical disruption of the electronic properties, as clearly demonstrated with the $(TiO_2)_{82}^{(001)}$ particle. The $(NVE)_c$ optimization is moderately successful at mitigating such bleeding of defined band edges, however they continue to be a misrepresentation of expected orbitals for larger nanoparticles with large (001) regions. The more aggressive $(NVE)_f$ procedure that was most successful in mitigating the formation of these states in the $(TiO_2)_n^{\{101\}}$ particles is also problematic as it leads to so much reconstruction in these particles that they are longer geometrically representative the targeted surface. This reconstruction also renders the particles unsuitable to model experimentally-sized nanoparticles. We showed that the most efficient way to mitigate these types of reconstruction is by generating particles with core bulk-like regions, as opposed to increasing the surface area of the particle. Specifically, a 202-unit (001) majority particle was required to approach by the $(TiO_2)_{126}^{(001)/\{010\}}$ particle.

Bibliography

[1] M. Riordan and L. Hoddeson, IEEE Spectr. **34**, 46 (1997).

[2] G. L. Pearson and J. Bardeen, Phys. Rev. **75**, 865 (1949).

[3] C. Freysoldt, B. Grabowski, T. Hickel, J. Neugebauer, G. Kresse, A. Janotti, and C. G. Van De Walle, Rev. Mod. Phys. **86**, 253 (2014).

[4] P. Hohenberg and W. Kohn, Phys. Rev. **136**, B864 (1964).

[5] W. Kohn and L. J. Sham, Phys. Rev. **140**, A1133 (1965).

[6] A. D. Becke, J. Phys. Chem. **140** (2014).

[7] J. Heyd, G. E. Scuseria, and M. Ernzerhof, J. Chem. Phys. **118**, 8207 (2003).

[8] G. M. Repa and L. A. Fredin, Phys. Chem. Chem. Phys. **23**, 23486 (2021).

[9] I. Mosquera-Lois, S. R. Kavanagh, A. Walsh, and D. O. Scanlon, Npj Comput. Mater. **9**, 25 (2023).

[10] M. Arrigoni and G. K. H. Madsen, Npj Comput. Mater. **7**, 71 (2021).

[11] M. Spera, A. Scarfato, Á. Pásztor, E. Giannini, D. R. Bowler, and C. Renner, Phys. Rev. Lett. **125**, 267603 (2020).

[12] J. Wyrick, X. Wang, P. Namboodiri, R. V. Kashid, F. Fei, J. Fox, and R. Silver, ACS Nano **16**, 19114 (2022).

[13] N. Herrera-Reinoza, A. C. Dos Santos, L. H. De Lima, R. Landers, and A. De Siervo, Chem. Mater. **33**, 2871 (2021).

[14] Z. Kou, A. Hashemi, M. J. Puska, A. V. Krasheninnikov, and H.-P. Komsa, Npj Comput. Mater. **6**, 59 (2020).

[15] G. M. Repa and L. A. Fredin, Appl. Phys. Lett. **121**, 022401 (2022).

[16] K. Komędera, J. Gatlik, A. Błachowski, J. Żukrowski, T. J. Sato, D. Legut, and U. D. Wdowik, Phys. Rev. B **103**, 024526 (2021).

[17] Y. Liu, R. Lan, C. Dong, K. Wang, X. Fu, H. Liu, Y. Qian, and J. Wang, J. Phys. Chem. C **125**, 4704 (2021).

[18] E. Guziewicz, O. Volnianska, I. Demchenko, P. Zeller, M. Amati, and L. Gregoratti, Phys. Rev. Appl. **18**, 044021 (2022).

[19] M. S. Wrighton, A. B. Ellis, P. T. Wolczanski, D. L. Morse, H. B. Abrahamson, and D. S. Ginley, J. Am. Chem. Soc. **98**, 2774 (1976).

[20] K. Domen, S. Naito, M. Soma, T. Onishi, and K. Tamaru, J. Chem. Soc. Chem. Commun., 543 (1980).

[21] D. I. Bilc, C. G. Floare, L. P. Zârbo, S. Garabagiu, S. Lemal, and P. Ghosez, J. Phys. Chem. C **120**, 25678 (2016).

[22] P. Noël, F. Trier, L. M. Vicente Arche, J. Bréhin, D. C. Vaz, V. Garcia, S. Fusil, A. Barthélémy, L. Vila, M. Bibes, and J. P. Attané, Nature **580**, 483 (2020).

[23] C. Baeumer, C. Schmitz, A. H. Ramadan, H. Du, K. Skaja, V. Feyer, P. Muller, B. Arndt, C. L. Jia, J. Mayer, R. A. De Souza, C. Michael Schneider, R. Waser, and R. Dittmann, Nat. Commun. **6**, 6:8610 (2015).

[24] A. V. Kovalevsky, M. H. Aguirre, S. Populoh, S. G. Patrício, N. M. Ferreira, S. M. Mikhalev, D. P. Fagg, A. Weidenkaff, and J. R. Frade, J. Mater. Chem. A **5**, 3909 (2017).

[25] C. Ricca, I. Timrov, M. Cococcioni, N. Marzari, and U. Aschauer, arXiv **2**, 23313 (2020).

[26] A. Marthinsen, T. Grande, and S. M. Selbach, J. Phys. Chem. C **124**, 12922 (2020).

[27] X. L. Dong, K. H. Zhang, and M. X. Xu, Front. Phys. **13**, 1 (2018).

[28] P. Sikam, P. Moontragoon, C. Sararat, A. Karaphun, E. Swatsitang, S. Pinitsoontorn, and P. Thongbai, Appl. Surf. Sci. **446**, 92 (2018).

[29] T. Shen, C. Hu, H. L. Dai, W. L. Yang, H. C. Liu, C. L. Tan, and X. L. Wei, Optik **127**, 3055 (2016).

[30] O. E. Kvyatkovskii, Phys. Solid State **54**, 1397 (2012).

[31] L. Zhang, B. Liu, H. Zhuang, P. R. Kent, V. R. Cooper, P. Ganesh, and H. Xu, Comput. Mater. Sci. **118**, 309 (2016).

[32] D. Kan, T. Terashima, R. Kanda, A. Masuno, K. Tanaka, S. Chu, H. Kan, A. Ishizumi, Y. Kanemitsu, Y. Shimakawa, and M. Takano, Nat. Mater. **4**, 816 (2005).

[33] M. Choi, F. Oba, Y. Kumagai, and I. Tanaka, Adv. Mater. **25**, 86 (2013).

[34] J. P. Buban, H. Iddir, and S. Öğüt, Phys. Rev. B - Condens. Matter Mater. Phys. **69**, 3 (2004).

[35] A. Janotti, J. B. Varley, M. Choi, and C. G. Van De Walle, Phys. Rev. B - Condens. Matter Mater. Phys. **90**, 1 (2014).

[36] C. Mitra, C. Lin, J. Robertson, and A. A. Demkov, Phys. Rev. B - Condens. Matter Mater. Phys. **86**, 1 (2012).

[37] R. Evarestov, E. Kotomin, and Yu. F. Zhukovskii, Int. J. Quantum Chem. J. **106**, 2173 (2005).

[38] S. Y. Chung, D. Y. Yoon, and S. J. L. Kang, Acta Mater. **50**, 3361 (2002).

[39] U. N. Gries, M. Kessel, F. V. Hensling, R. Dittmann, M. Martin, and R. A. De Souza, Phys. Rev. Mater. **4**, 41 (2020).

[40] J. N. Baker, P. C. Bowes, J. S. Harris, and D. L. Irving, J. Appl. Phys. **124**, 122903 (2018).

[41] R. A. Mackie, S. Singh, J. Laverock, S. B. Dugdale, and D. J. Keeble, Phys. Rev. B - Condens. Matter Mater. Phys. **79**, 1 (2009).

[42] D. J. Keeble, S. Wicklein, R. Dittmann, L. Ravelli, R. A. MacKie, and W. Egger, Phys. Rev. Lett. **105**, 3 (2010).

[43] R. A. Maier, T. A. Pomorski, P. M. Lenahan, and C. A. Randall, J. Appl. Phys. **118**, 164102 (2015).

[44] R. A. Maier and C. A. Randall, J. Am. Ceram. Soc. **99**, edited by J. Stevenson, 3350 (2016).

[45] R. A. Maier, A. C. Johnston-Peck, and M. P. Donohue, Adv. Funct. Mater. **26**, 8325 (2016).

[46] I. Fongkaew, J. T-Thienprasert, and S. Limpijumnong, Ceram. Int. **43**, S381 (2017).

[47] H. Mansoor, W. L. Harrigan, K. A. Lehuta, and K. R. Kittilstved, Front. Chem. **7**, 1 (2019).

[48] R. A. Maier, E. Cockayne, M. Donohue, G. Cibin, and I. Levin, Chem. Mater. **32**, 4651 (2020).

[49] P. Giannozzi, S. Baroni, N. Bonini, M. Calandra, R. Car, C. Cavazzoni, D. Ceresoli, G. L. Chiarotti, M. Cococcioni, I. Dabo, A. Dal Corso, S. De Gironcoli, S. Fabris, G. Fratesi, R. Gebauer, U. Gerstmann, C. Gougoussis, A. Kokalj, M. Lazzeri, L. Martin-Samos, N. Marzari, F. Mauri, R. Mazzarello, S. Paolini, A. Pasquarello, L. Paulatto, C. Sbraccia, S. Scandolo, G. Sclauzero, A. P. Seitsonen, A. Smogunov, P. Umari, and R. M. Wentzcovitch, J. Phys. Condens. Matter **21**, 395502 (2009).

[50] P. Giannozzi, O. Baseggio, P. Bonfà, D. Brunato, R. Car, I. Carnimeo, C. Cavazzoni, S. De Gironcoli, P. Delugas, F. Ferrari Ruffino, A. Ferretti, N. Marzari, I. Timrov, A. Urru, and S. Baroni, J. Chem. Phys. **152**, 154105 (2020).

[51] A. D. Becke, Phys. Rev. A **38**, 3098 (1988).

[52] C. Lee, Y. Weitao, and R. Parr, Phys. Rev. B **37**, 785 (1988).

[53] S. Piskunov, E. Heifets, R. Eglitis, and B. G, Compuational Mater. Sci. **29**, 165 (2004).

[54] E. Holmström, P. Spijker, and A. S. Foster, Proc. R. Soc. Math. Phys. Eng. Sci. **472**, 20160293 (2016).

[55] G. Kresse and J. Hafner, Phys. Rev. B **47**, 558 (1993).

[56] G. Kresse and J. Furthmüller, Comput. Mater. Sci. **6**, 15 (1996).

[57] G. Kresse and J. Furthmüller, Comput. Mater. Sci. **6**, 15 (1996).

[58] A. V. Krukau, O. A. Vydrov, A. F. Izmaylov, and G. E. Scuseria, J. Chem. Phys. **125**, 224106 (2006).

[59] W. P, Acta Crystallogr. B **53**, 32 (1997).

[60] W. Jauch and A. Palmer, Phys. Rev. B - Condens. Matter Mater. Phys. **60**, 2961 (1999).

[61] B. I, J. Phys. Conf. Ser. **833**, 012001 (2017).

[62] H. Sakai, J. Fujioka, T. Fukuda, D. Okuyama, D. Hashizume, F. Kagawa, H. Nakao, Y. Murakami, T. Arima, A. Q. Baron, Y. Taguchi, and Y. Tokura, Phys. Rev. Lett. **107**, 1 (2011).

[63] V. V. Laguta, I. V. Kondakova, I. P. Bykov, M. D. Glinchuk, A. Tkach, P. M. Vilarinho, and L. Jastrabik, Phys. Rev. B - Condens. Matter Mater. Phys. **76**, 2 (2007).

[64] N. E. Brese and M. O'Keeffe, Acta Crystallogr. Sect. B **47**, 192 (1991).

[65] K. Van Benthem, C. Elsässer, and R. H. French, J. Appl. Phys. **90**, 6156 (2001).

[66] D. Choudhury, S. Mukherjee, P. Mandal, A. Sundaresan, U. V. Waghmare, S. Bhattacharjee, R. Mathieu, P. Lazor, O. Eriksson, B. Sanyal, P. Nordblad, A. Sharma, S. V. Bhat, O. Karis, and D. D. Sarma, Phys. Rev. B **84**, 125124 (2011).

[67] M. N. Kamalasanan, N. Deepak Kumar, and S. Chandra, J. Appl. Phys. **74**, 679 (1993).

[68] V. Goldschmidt, *Geochemistry* (Oxford University Press, Oxford, 1954).

[69] K. Ahadi, L. Galletti, Y. Li, S. Salmani-Rezaie, W. Wu, and S. Stemmer, Sci. Adv. **5**, 0120 (2019).

[70] J. J. Brown, Z. Ke, W. Geng, and A. J. Page, J. Phys. Chem. **122**, 14590 (2018).

[71] I. Fongkaew, J. T-Thienprasert, and S. Limpijumnong, Ceram. Int. **43**, The 10th Asian Meeting on Electroceramics (AMEC-10), S381 (2017).

[72] R. I. Eglitis and D. Vanderbilt, Phys. Rev. B **77**, 195408 (2008).

[73] R. I. Eglitis, J. Purans, A. I. Popov, and R. Jia, Symmetry **13**, 10.3390/sym13101920 (2021).

[74] C. Diao, H. Li, Y. Yang, H. Hao, Z. Yao, and H. Liu, Ceram. Int. **45**, 11784 (2019).

[75] M. Verma, B. Geisler, and R. Pentcheva, Phys. Rev. B **100**, 165126 (2019).

[76] I. Levin, V. Krayzman, J. C. Woicik, A. Tkach, and P. M. Vilarinho, Appl. Phys. Lett. **96**, 052904 (2010).

[77] D. V. Azamat, A. G. Badalyan, P. G. Baranov, V. A. Trepakov, M. Hrabovsky, L. Jastrabik, and A. Dejneka, J. Appl. Phys. **124**, 124101 (2018).

[78] M. Valant, T. Kolodiazhnyi, I. Arčon, F. Aguesse, A.-K. Axelsson, and N. M. Alford, Adv. Funct. Mater. **22**, 2114 (2012).

[79] D. Daraselia, D. Japaridze, Z. Jibuti, A. Shengelaya, and K. A. Müller, J. Appl. Phys. **121**, 145104 (2017).

[80] K. Szász, X. T. Trinh, N. T. Son, E. Janzén, and A. Gali, J. Appl. Phys. **115**, 073705 (2014).

[81] R. Kuate Defo, E. Kaxiras, and S. L. Richardson, Phys. Rev. B **104**, 075158 (2021).

[82] M. W. Swift, H. Peelaers, S. Mu, J. J. L. Morton, and C. G. Van de Walle, Npj Comput. Mater. **6**, 181 (2020).

[83] S. Shehada, M. dos Santos Dias, F. S. M. Guimarães, M. Abusaa, and S. Lounis, Npj Comput. Mater. **7**, 87 (2021).

[84] P. E. Blöchl, Phys. Rev. B **50**, 17953 (1994).

[85] J. P. Perdew, K. Burke, and M. Ernzerhof, Phys. Rev. Lett. **77**, 3865 (1996).

[86] R. I. Eglitis, J. Purans, and R. Jia, Crystals **11** (2021).

[87] O. V. Yazyev, I. Tavernelli, L. Helm, and U. Röthlisberger, Phys. Rev. B **71**, 115110 (2005).

[88] K. Szász, T. Hornos, M. Marsman, and A. Gali, Phys. Rev. B **88**, 075202 (2013).

[89] K. A. Müller, Phys. Rev. Lett. **2**, 341 (1959).

[90] C. Azzoni, M. Mozzati, A. Paleari, V. Massarotti, M. Bini, and D. Capsoni, Solid State Commun. **114**, 617 (2000).

[91] A. Zorko, M. Pregelj, H. Luetkens, A.-K. Axelsson, and M. Valant, Phys. Rev. B **89**, 094418 (2014).

[92] R. A. Serway, W. Berlinger, K. A. Müller, and R. W. Collins, Phys. Rev. B **16**, 4761 (1977).

[93] W. Tang, E. Sanville, and G. Henkelman, J. Phys.: Condens. Matter **21**, 084204 (2009).

[94] A. V. Krukau, G. E. Scuseria, J. P. Perdew, and A. Savin, J. Chem. Phys. **129**, 124103 (2008).

[95] V. Ivády, I. A. Abrikosov, E. Janzén, and A. Gali, Phys. Rev. B **87**, 205201 (2013).

[96] S. Lany, H. Raebiger, and A. Zunger, Phys. Rev. B **77**, 241201 (2008).

[97] P. Tan, M. Liu, Z. Shao, and M. Ni, Adv. Energy Mater. **7**, 1602674 (2017).

[98] M. A. K. Y. Shah, S. Rauf, B. Zhu, N. Mushtaq, M. Yousaf, P. D. Lund, C. Xia, and M. I. Asghar, ACS Appl. Energy Mater. **4**, 365 (2021).

[99] M. A. Haque, S. Kee, D. R. Villalva, W.-L. Ong, and D. Baran, Adv. Sci. **7**, 1903389 (2020).

[100] Y. Xu, Y. Liang, Q. He, R. Xu, D. Chen, X. Xu, and H. Hu, Bull. Mater. Sci. **46**, 6 (2022).

[101] C. Hou, W. Huang, W. Zhao, D. Zhang, Y. Yin, and X. Li, ACS Appl. Mater. Interfaces **9**, 20484 (2017).

[102] R. Pazik, G. A. Seisenbaeva, R. J. Wiglusz, L. Kepinski, and V. G. Kessler, Inorg. Chem. **50**, 2966 (2011).

[103] Y.-Y. Pai, A. Tylan-Tyler, P. Irvin, and J. Levy, Rep. Prog. Phys. **81**, 036503 (2018).

[104] R. Li, C. Zhang, J. Liu, J. Zhou, and L. Xu, Mater. Res. Express **6**, 102006 (2019).

[105] R. A. De Souza, Adv. Funct. Mater. **25**, 6326 (2015).

[106] M. Dawber and J. F. Scott, Appl. Phys. Lett. **76**, 1060 (2000).

[107] W. Liu and C. A. Randall, J. Am. Ceram. Soc. **91**, 3251 (2008).

[108] L. Walters and R. Grace, J. Phys. Chem. Solids **28**, 245 (1967).

[109] A. Muller and K. H. Hardtl, Appl. Phys. Solids Surf. **49**, 75 (1989).

[110] R. A. De Souza, V. Metlenko, D. Park, and T. E. Weirich, Phys. Rev. B **85**, 174109 (2012).

[111] J. Carrasco, F. Illas, N. Lopez, E. A. Kotomin, Y. F. Zhukovskii, R. A. Evarestov, Y. A. Mastrikov, S. Piskunov, and J. Maier, Phys. Rev. B **73**, 064106 (2006).

[112] M. Schie, R. Waser, and R. A. De Souza, J. Phys. Chem. C **118**, 15185 (2014).

[113] C. R. A. Catlow, Z. X. Guo, M. Miskufova, S. A. Shevlin, A. G. H. Smith, A. A. Sokol, A. Walsh, D. J. Wilson, and S. M. Woodley, Philos. Trans. R. Soc. Math. Phys. Eng. Sci. **368**, 3379 (2010).

[114] R. Waser, J. Am. Ceram. Soc. **74**, 1934 (1991).

[115] R. Merkle and J. Maier, Angew. Chem. Int. Ed. **47**, 3874 (2008).

[116] K. Müller, J. Phys. **42**, 551 (1981).

[117] R. Merkle and J. Maier, Phys. Chem. Chem. Phys. ***5***, 2297 (2003).

[118] D. Ascienzo, O. Kurt, S. Greenbaum, T. J. M. Bayer, M. Russell, J. Wang, C. A. Randall, and Y. Ren, J. Am. Ceram. Soc. **102**, 4353 (2019).

[119] J. P. Perdew, A. Ruzsinszky, G. I. Csonka, O. A. Vydrov, G. E. Scuseria, L. A. Constantin, X. Zhou, and K. Burke, Phys. Rev. Lett. **100**, 136406 (2008).

[120] A. Paladino, L. Rubin, and J. Waugh, J. Phys. Chem. Solids **26**, 391 (1965).

[121] Z. Zhou, D. Chu, and C. Cazorla, Sci. Rep. **11**, 11499 (2021).

[122] B. Hoex, S. B. S. Heil, E. Langereis, M. C. M. van de Sanden, and W. M. M. Kessels, Appl. Phys. Lett. **89**, 042112 (2006).

[123] R. Hezel and K. Jaeger, J. Electrochem. Soc. **136**, 518 (1989).

[124] P. F. Carcia, R. S. McLean, M. H. Reilly, M. D. Groner, and S. M. George, Appl. Phys. Lett. **89**, 10.1063/1.2221912 (2006).

[125] M. D. Groner, F. H. Fabreguette, J. W. Elam, and S. M. George, Chem. Mater. **16**, 639 (2004).

[126] R. S. Johnson, G. Lucovsky, and I. Baumvol, J. Vac. Sci. Technol. Vac. Surf. Films **19**, 1353 (2001).

[127] E. P. Gusev, M. Copel, E. Cartier, I. J. R. Baumvol, C. Krug, and M. A. Gribelyuk, Appl. Phys. Lett. **76**, 176 (2000).

[128] R. L. Puurunen, J. Appl. Phys. **97**, 10.1063/1.1940727 (2005).

[129] S. M. George, Chem. Rev. **110**, 111 (2010).

[130] M. J. Young, N. M. Bedford, A. Yanguas-Gil, S. Letourneau, M. Coile, D. J. Mandia, B. Aoun, A. S. Cavanagh, S. M. George, and J. W. Elam, ACS Appl. Mater. Interfaces **12**, 22804 (2020).

[131] C. Shi, O. L. G. Alderman, D. Berman, J. Du, J. Neuefeind, A. Tamalonis, J. K. R. Weber, J. You, and C. J. Benmore, Front. Mater. **6**, 10.3389/fmats.2019.00038 (2019).

[132] R. Manaila, A. Dévényi, and E. Candet, Thin Solid Films **116**, 289 (1984).

[133] S. Ansell, S. Krishnan, J. R. Weber, J. J. Felten, P. C. Nordine, M. A. Beno, D. L. Price, and M.-L. Saboungi, Phys. Rev. Lett. **78**, 464 (1997).

[134] P. Lamparter and R. Kniep, Phys. B Condens. Matter **234**, 405 (1997).

[135] L. B. Skinner, A. C. Barnes, P. S. Salmon, L. Hennet, H. E. Fischer, C. J. Benmore, S. Kohara, J. K. R. Weber, A. Bytchkov, M. C. Wilding, J. B. Parise, T. O. Farmer, I. Pozdnyakova, S. K. Tumber, and K. Ohara, Phys. Rev. B **87**, 10.1103/PhysRevB.87.024201 (2013).

[136] A. M. Jasim, X. He, Y. Xing, T. A. White, and M. J. Young, ACS Omega **6**, 8986 (2021).

[137] L. Zeng, D. T. Tran, C.-W. Tai, G. Svensson, and E. Olsson, Sci. Rep. **6**, 10.1038/srep29679 (2016).

[138] C. Landron, L. Hennet, T. Jenkins, G. Greaves, J. Coutures, and A. Soper, Phys. Rev. Lett. **86**, 4839 (2001).

[139] V.-V. Le, V.-H. Nguyen, V.-H. Nguyen, and K.-H. Pham, Comput. Mater. Sci. **79**, 110 (2013).

[140] V. V. Hoang, Phys. Rev. B **70**, 10.1103/PhysRevB.70.134204 (2004).

[141] G. Gutiérrez, A. B. Belonoshko, R. Ahuja, and B. Johansson, Phys. Rev. E **61**, 2723 (2000).

[142] L. B. Skinner, C. J. Benmore, J. K. R. Weber, J. Du, J. Neuefeind, S. K. Tumber, and J. B. Parise, Phys. Rev. Lett. **112**, 10.1103/PhysRevLett.112.157801 (2014).

[143] S. M. Prokes, M. B. Katz, and M. E. Twigg, Apl Mater. **2**, 10.1063/1.4868300 (2014).

[144] B. Hoex, J. J. H. Gielis, M. C. M. van Sanden, and W. M. M. Kessels, J. Appl. Phys. **104**, 10.1063/1.3021091 (2008).

[145] J. Aboaf, D. Kerr, and E. Bassous, J. Electrochem. Soc. **120**, 1103 (1973).

[146] O. A. Dicks and A. L. Shluger, J. Phys.-Condens. Matter **29**, 10.1088/1361-648X/aa7767 (2017).

[147] S. Davis and G. Gutierrez, J. Phys.-Condens. Matter **23**, 10.1088/0953-8984/23/49/495401 (2011).

[148] J. Heyd, G. E. Scuseria, and M. Ernzerhof, J. Chem. Phys. **124**, 219906 (2006).

[149] F. P. Sabino, R. Besse, L. N. Oliveira, S.-H. Wei, and J. L. F. Da Silva, Phys. Rev. B **92**, 10.1103/PhysRevB.92.205308 (2015).

[150] E. O. Filatova and A. S. Konashuk, J. Phys. Chem. C **119**, 20755 (2015).

[151] K. K. Ghuman and C. V. Singh, J. Phys.: Condens. Matter **25**, 475501 (2013).

[152] V. S. S. Duarte, A. M. Rodrigues, T. S. de Andrade-Filho, D. d. N. Souza, E. R. P. de Novais, A. d. L. F. Novais, and G. C. A. de Oliveira, Struct. Chem. **32**, 1589 (2021).

[153] C. A. Triana, C. M. Araujo, R. Ahuja, G. A. Niklasson, and T. Edvinsson, Sci. Rep. **7**, 2044 (2017).

[154] D. Mora-Fonz, M. Kaviani, and A. L. Shluger, Phys. Rev. B **102**, 054205 (2020).

[155] H. H. Pham and L.-W. Wang, Phys. Chem. Chem. Phys. **17**, 541 (2015).

[156] K. N. Subedi, K. Prasai, M. N. Kozicki, and D. A. Drabold, Phys. Rev. Mater. **3**, 065605 (2019).

[157] O. A. Dicks, J. Cottom, A. L. Shluger, and V. V. Afanas'ev, Nanotechnology **30**, 10.1088/1361-6528/ab0450 (2019).

[158] K. A. Stoerzinger, L. J. Enman, E. A. Cochran, J. T. Diulus, R. T. Frederick, K. Artyushkova, E. J. Crumlin, G. S. Herman, and S. W. Boettcher, J. Phys. Chem. C **123**, 27048 (2019).

[159] D. Vernekar, M. Dayyan, S. Ratha, C. V. Rode, M. Haider, T. S. Khan, and D. Jagadeesan, ACS Catal. **11**, 10754 (2021).

[160] K. K. Ghuman and C. V. Singh, J. Phys. Chem. C **120**, 27910 (2016).

[161] J. Zhong, Z. Xu, J. Lu, and Y. Y. Li, J. Phys. Chem. C **127**, 7268 (2023).

[162] N. A. Deskins, J. Du, and P. Rao, Phys. Chem. Chem. Phys. **19**, 18671 (2017).

[163] K. K. Ghuman, Sci. Technol. Adv. Mater. **19**, 44 (2018).

[164] A. Pugliese, B. Shyam, G. M. Repa, A. H. Nguyen, A. Mehta, E. B. Webb Iii, L. A. Fredin, and N. C. Strandwitz, ACS Omega **7**, 41033 (2022).

[165] P. Biswas, R. Atta-Fynn, and D. A. Drabold, Phys. Rev. B **69**, 195207 (2004).

[166] F. Zhang, P. J. Chupas, S. L. A. Lui, J. C. Hanson, W. A. Caliebe, P. L. Lee, and S.-W. Chan, Chem. Mater. **19**, 3118 (2007).

[167] M. F. Calegari Andrade and A. Selloni, Phys. Rev. Mater. **4**, 113803 (2020).

[168] J. Zhang, P. Hu, and H. Wang, The J. Phys. Chem. C **124**, 10483 (2020).

[169] D. Sibanda, S. T. Oyinbo, and T.-C. Jen, Nanotechnol. Rev. **11**, 1332 (2022).

[170] B. R. Goldsmith, B. Peters, J. K. Johnson, B. C. Gates, and S. L. Scott, ACS Catal. **7**, 7543 (2017).

[171] Y. Ai, L. Liu, C. Zhang, L. Qi, M. He, Z. Liang, H.-b. Sun, G. Luo, and Q. Liang, ACS Appl. Mater. Interfaces **10**, 32180 (2018).

[172] Z. Li, C. Mao, Q. Pei, P. N. Duchesne, T. He, M. Xia, J. Wang, L. Wang, R. Song, A. A. Jelle, D. M. Meira, Q. Ge, K. K. Ghuman, L. He, X. Zhang, and G. A. Ozin, Nat. Commun. **13**, 7205 (2022).

[173] H. Annath, J. C. Manayil, J. Thompson, A. C. Marr, and R. Raja, Appl. Catal. Gen. **627**, 118376 (2021).

[174] C. S. Ewing, S. Bhavsar, G. Veser, J. J. McCarthy, and J. K. Johnson, Langmuir **30**, 5133 (2014).

[175] J. J. Gutiérrez Moreno, K. Pan, Y. Wang, and W. Li, Langmuir **36**, 5680 (2020).

[176] K. Kaur and C. V. Singh, Energy Procedia **29**, 291 (2012).

[177] J. D. Cyran, M. A. Donovan, D. Vollmer, F. Siro Brigiano, S. Pezzotti, D. R. Galimberti, M.-P. Gaigeot, M. Bonn, and E. H. G. Backus, Proc. Natl. Acad. Sci. **116**, 1520 (2019).

[178] P. N. Wimalasiri, N. P. Nguyen, H. S. Senanayake, B. B. Laird, and W. H. Thompson, J. Phys. Chem. C **125**, 23418 (2021).

[179] V. L. Deringer, M. A. Caro, R. Jana, A. Aarva, S. R. Elliott, T. Laurila, G. Csányi, and L. Pastewka, Chem. Mater. **30**, 7438 (2018).

[180] B. Astinchap and K. G. Laelabadi, J. Phys. Chem. Solids **129**, 217 (2019).

[181] A. Sobczyk-Guzenda, B. Pietrzyk, H. Szymanowski, M. Gazicki-Lipman, and W. Jakubowski, Ceram. Int. **39**, 2787 (2013).

[182] V. Petkov, G. Holzhüter, U. Tröge, T. Gerber, and B. Himmel, J. Non-Cryst. Solids **231**, 17 (1998).

[183] X. Wang, W. Shi, S. Wang, H. Zhao, J. Lin, Z. Yang, M. Chen, and L. Guo, J. Am. Chem. Soc. **141**, 5856 (2019).

[184] J. Yang, Y. Wang, W. Li, L. Wang, Y. Fan, W. Jiang, W. Luo, Y. Wang, B. Kong, C. Selomulya, H. K. Liu, S. X. Dou, and D. Zhao, Adv. Mater. **29**, 1700523 (2017).

[185] S. Hu, M. R. Shaner, J. A. Beardslee, M. Lichterman, B. S. Brunschwig, and N. S. Lewis, Science **344**, 1005 (2014).

[186] M. Matsui and M. Akaogi, Mol. Simul. **6**, 239 (1991).

[187] A. P. Thompson, H. M. Aktulga, R. Berger, D. S. Bolintineanu, W. M. Brown, P. S. Crozier, P. J. in 't Veld, A. Kohlmeyer, S. G. Moore, T. D. Nguyen, R. Shan, M. J. Stevens, J. Tranchida, C. Trott, and S. J. Plimpton, Comput. Phys. Commun. **271**, 108171 (2022).

[188] L. Martínez, R. Andrade, E. G. Birgin, and J. M. Martínez, J. Comput. Chem. **30**, 2157 (2009).

[189] H. Yildirim, J. Greeley, and S. K. R. S. Sankaranarayanan, The J. Phys. Chem. C **115**, 15661 (2011).

[190] J. Mavračić, F. C. Mocanu, V. L. Deringer, G. Csányi, and S. R. Elliott, J. Phys. Chem. Lett. **9**, 2985 (2018).

[191] M. Landmann, T. Köhler, S. Köppen, E. Rauls, T. Frauenheim, and W. G. Schmidt, Phys. Rev. B **86**, 064201 (2012).

[192] T. Köhler, M. Turowski, H. Ehlers, M. Landmann, D. Ristau, and T. Frauenheim, J. Phys. Appl. Phys. **46**, 325302 (2013).

[193] V. V. Hoang, H. Zung, and N. H. Trong, Eur. Phys. J. D **44**, 515 (2007).

[194] S. De, A. P. Bartók, G. Csányi, and M. Ceriotti, Phys. Chem. Chem. Phys. **18**, 13754 (2016).

[195] L. Himanen, M. O. Jäger, E. V. Morooka, F. Federici Canova, Y. S. Ranawat, D. Z. Gao, P. Rinke, and A. S. Foster, Comput. Phys. Commun. **247**, 106949 (2020).

[196] L. Skowronski, K. Zdunek, K. Nowakowska-Langier, R. Chodun, M. Trzcinski, M. Kobierski, M. Kustra, A. Wachowiak, W. Wachowiak, T. Hiller, A. Grabowski, L. Kurpaska, and M. Naparty, Surf. Coat. Technol. **282**, 16 (2015).

[197] L. X. Chen, T. Rajh, W. Jäger, J. Nedeljkovic, and M. C. Thurnauer, J. Synchrotron Radiat. **6**, 445 (1999).

[198] R. P. Sabatini, W. T. Eckenhoff, A. Orchard, K. R. Liwosz, M. R. Detty, D. F. Watson, D. W. McCamant, and R. Eisenberg, J. Am. Chem. Soc. **136**, 7740 (2014).

[199] E. Jakubikova and D. N. Bowman, Acc. Chem. Res. **48**, 1441 (2015).

[200] Q. Kang, J. Cao, Y. Zhang, L. Liu, H. Xu, and J. Ye, J. Mater. Chem. A **1**, 5766 (2013).

[201] M. Ismael, Sol. Energy **211**, 522 (2020).

[202] L. Mino, G. Spoto, and A. M. Ferrari, J. Phys. Chem. C **118**, 25016 (2014).

[203] S. N. Habisreutinger, L. Schmidt-Mende, and J. K. Stolarczyk, Angew. Chem. Int. Ed. **52**, 7372 (2013).

[204] P.-Q. Wang, Y. Bai, J.-Y. Liu, Z. Fan, and Y.-Q. Hu, Catal. Commun. **29**, 185 (2012).

[205] H. G. Yang, C. H. Sun, S. Z. Qiao, J. Zou, G. Liu, S. C. Smith, H. M. Cheng, and G. Q. Lu, Nature **453**, 638 (2008).

[206] Y. Alivov and Z. Y. Fan, J. Phys. Chem. C **113**, 12954 (2009).

[207] N. M. Dimitrijevic, Z. V. Saponjic, B. M. Rabatic, O. G. Poluektov, and T. Rajh, J. Phys. Chem. C **111**, 14597 (2007).

[208] C.-T. Dinh, T.-D. Nguyen, F. Kleitz, and T.-O. Do, ACS Nano **3**, 3737 (2009).

[209] C. Chen, G. A. Sewvandi, T. Kusunose, Y. Tanaka, S. Nakanishi, and Q. Feng, CrystEngComm **16**, 8885 (2014).

[210] T. R. Gordon, M. Cargnello, T. Paik, F. Mangolini, R. T. Weber, P. Fornasiero, and C. B. Murray, J. Am. Chem. Soc. **134**, 6751 (2012).

[211] W. Yuan, Y. Wang, H. Li, H. Wu, Z. Zhang, A. Selloni, and C. Sun, Nano Lett. **16**, 132 (2016).

[212] M. Lazzeri and A. Selloni, Phys. Rev. Lett. **87**, 266105 (2001).

[213] H. Sun, W. Lu, and J. Zhao, J. Phys. Chem. C **122**, 14528 (2018).

[214] T. Würger, W. Heckel, K. Sellschopp, S. Müller, A. Stierle, Y. Wang, H. Noei, and G. Feldbauer, J. Phys. Chem. C **122**, 19481 (2018).

[215] K. Shirai, G. Fazio, T. Sugimoto, D. Selli, L. Ferraro, K. Watanabe, M. Haruta, B. Ohtani, H. Kurata, C. Di Valentin, and Y. Matsumoto, J. Am. Chem. Soc. **140**, 1415 (2018).

[216] F. A. Soria and C. Di Valentin, Nanoscale **13**, 4151 (2021).

[217] K. C. Ko, S. T. Bromley, J. Y. Lee, and F. Illas, J. Phys. Chem. Lett. **8**, 5593 (2017).

[218] A. V. Vorontsov, H. Valdés, P. G. Smirniotis, and Y. Paz, Surfaces **3**, 72 (2020).

[219] Á. Morales-García, A. Macià Escatllar, F. Illas, and S. T. Bromley, Nanoscale **11**, 9032 (2019).

[220] O. Lamiel-Garcia, K. C. Ko, J. Y. Lee, S. T. Bromley, and F. Illas, J. Chem. Theory Comput. **13**, 1785 (2017).

[221] A. S. Barnard and L. A. Curtiss, Nano Lett. **5**, 1261 (2005).

[222] D. R. Hummer, J. D. Kubicki, P. R. C. Kent, J. E. Post, and P. J. Heaney, J. Phys. Chem. C **113**, 4240 (2009).

[223] F. Nunzi, L. Storchi, M. Manca, R. Giannuzzi, G. Gigli, and F. De Angelis, ACS Appl. Mater. Interfaces **6**, 2471 (2014).

[224] A. V. Vorontsov and P. G. Smirniotis, J. Photochem. Photobiol **363**, 51 (2018).

[225] V. S. Naumov, A. S. Loginova, A. A. Avdoshin, S. K. Ignatov, A. V. Mayorov, B. Aradi, and T. Frauenheim, Int. J. Quantum Chem. **121**, 10.1002/qua.26427 (2021).

[226] J.-i. Fujisawa, S. Kato, and M. Hanaya, Chem. Phys. Lett. **788**, 139274 (2022).

[227] S.-H. Liu, H. Fu, Y.-M. Cheng, K.-L. Wu, S.-T. Ho, Y. Chi, and P.-T. Chou, J. Phys. Chem. C **116**, 16338 (2012).

[228] K. L. Syres, A. G. Thomas, W. R. Flavell, B. F. Spencer, F. Bondino, M. Malvestuto, A. Preobrajenski, and M. Grätzel, J. Phys. Chem. C **116**, 23515 (2012).

[229] M. J. Lundqvist, M. Nilsing, P. Persson, and S. Lunell, Int. J. Quantum Chem. **106**, 3214 (2006).

[230] H. Wang and J. P. Lewis, Phys. Status Solidi B **248**, 2037 (2011).

[231] M. Gałyńska and P. Persson, Int. J. Quantum Chem. **113**, 2611 (2013).

[232] D. González, B. Camino, J. Heras-Domingo, A. Rimola, L. Rodríguez-Santiago, X. Solans-Monfort, and M. Sodupe, J. Phys Chem. C **124**, 1227 (2020).

[233] F. De Angelis, C. Di Valentin, S. Fantacci, A. Vittadini, and A. Selloni, Chem. Rev. **114**, 9708 (2014).

[234] G. Fazio, L. Ferrighi, and C. Di Valentin, J. Phys. Chem. C **119**, 20735 (2015).

[235] P. Persson, J. C. M. Gebhardt, and S. Lunell, J. Phys. Chem. B **107**, 3336 (2003).

[236] Y. A. Çetin, B. Martorell, F. Serratosa, N. Aguilera-Porta, and M. Calatayud, J. Phys.: Condens. Matter **34**, 314004 (2022).

[237] Á. Morales-García, O. Lamiel-García, R. Valero, and F. Illas, J. Phys. Chem. C **122**, 2413 (2018).

[238] J. He, R. Behera, M. Finnis, X. Li, E. Dickey, S. Phillpot, and S. Sinnott, Acta Mater. ***55***, 4325 (2007).

[239] A. S. Barnard, Rep. Prog. Phys. **73**, 086502 (2010).

[240] D. Selli, G. Fazio, and C. Di Valentin, J. Chem. Phys. **147**, 164701 (2017).

[241] A. V. Vorontsov, Kinet. Catal. **58**, 688 (2017).

[242] A. Macià Escatllar, Á. Morales-García, F. Illas, and S. T. Bromley, J. Chem. Phys. **150**, 214305 (2019).

[243] C. Vandervelden, A. Jystad, B. Peters, and M. Caricato, Ind. Eng. Chem. Res. **60**, 12834 (2021).

[244] J. C. Boettger, Phys. Rev. B **49**, 16798 (1994).

[245] V. Fiorentini and M. Methfessel, J. Phys.: Condens. Matter **8** (1996).

[246] M. J. Frisch, G. W. Trucks, H. B. Schlegel, G. E. Scuseria, M. A. Robb, J. R. Cheeseman, G. Scalmani, V. Barone, G. A. Petersson, H. Nakatsuji, X. Li, M. Caricato, A. V. Marenich, J. Bloino, B. G. Janesko, R. Gomperts, B. Mennucci, H. P. Hratchian, J. V. Ortiz, A. F. Izmaylov, J. L. Sonnenberg, D. Williams-Young, F. Ding, F. Lipparini, F. Egidi, J. Goings, B. Peng, A. Petrone, T. Henderson, D. Ranasinghe, V. G. Zakrzewski, J. Gao, N. Rega, G. Zheng, W. Liang, M. Hada, M. Ehara, K. Toyota, R. Fukuda, J. Hasegawa, M. Ishida, T. Nakajima, Y. Honda, O. Kitao, H. Nakai, T. Vreven, K. Throssell, J. A. Montgomery Jr., J. E. Peralta, F. Ogliaro, M. J. Bearpark, J. J. Heyd, E. N. Brothers, K. N. Kudin, V. N. Staroverov, T. A. Keith, R. Kobayashi, J. Normand, K. Raghavachari, A. P. Rendell, J. C. Burant, S. S. Iyengar, J. Tomasi, M. Cossi, J. M. Millam, M. Klene, C. Adamo, R. Cammi, J. W. Ochterski, R. L. Martin, K. Morokuma, O. Farkas, J. B. Foresman, and D. J. Fox, *Gaussian~16 Revision C.01*, Gaussian Inc. Wallingford CT, 2016.

[247] A. D. Becke, J. Chem. Phys. **98**, 5648 (1993).

[248] Y. Bouteiller, C. Mijoule, M. Nizam, J. Barthelat, J. Daudey, M. Pelissier, and B. Silvi, Mol. Phys. **65**, 295 (1988).

[249] R. Dennington, T. A. Keith, and J. M. Millam, *Gaussview Version 6*, Semichem Inc. Shawnee Mission KS, 2019.

[250] H. Zhang, B. Chen, J. F. Banfield, and G. A. Waychunas, Phys. Rev. B **78**, 214106 (2008).

[251] H. Wadell, J. Geol. **43**, 250 (1935).

[252] I. Gonzalo-Juan, A. J. Krejci, M. A. Rodriguez, Y. Zhou, K. A. Fichthorn, and J. H. Dickerson, Appl. Phys. Lett. **105**, 113108 (2014).

[253] W. Yan, S. Li, Y. Zhang, Q. Yao, and S. D. Tse, J. Phys. Chem. C **114**, 10755 (2010).

[254] A. A. Lino, H. Chacham, and M. S. C. Mazzoni, J. Phys. Chem. C **115**, 18047 (2011).

Gil M. Repa

Computational Chemist | Ph.D. Candidate

gil-repa | gir218 | ORCID | gilrepa@outlook.com

Research Highlights

A Deeper Understanding of Material Properties Through Computational Model Development August 2019 – Current

Graduate Research Asst., Department of Chemistry, Lehigh University, Advisor: Lisa A. Fredin

- Discovered unreported defect geometries in model semiconductors to rationalize previously unexplainable measurements.
- Resolved the origin of contested spectroscopic signatures by using a new model for defect atomic spin properties.
- Advanced design criteria to systematically alter ionic conductivity of battery materials through doping and provided the first long-range quantum-mechanical insight into atomic diffusion.
- Improved protocols for optimizing large oxide nanoparticle models that are among the largest objects to have ever been described with quantum mechanics.
- Proposed novel methods to generate more realistic surface models to enable a more accurate description of catalytic atmospheric carbon dioxide reduction.
- Developed software to enable calculation of advanced physical properties ranging from spin-orbit coupling to nanoparticle shape.
- Presented research results at one regional and two national conferences.
- Authored nine peer-reviewed publications, including five lead author and one perspective article.

Structure-based Drug Design for Cancer August 2017 – May 2019

Undergraduate Research Asst., Department of Physics, OK State Univ., Advisor: Donghua H. Zhou

- Performed computer-aided drug design to improve the efficiency of small molecule cancer growth inhibitors while adhering to biological design principles.

Protein Mutations for Enhanced Catalysis August 2015 – May 2017

Undergraduate Research Asst., Department of Physiological Sciences, OK State Univ., Advisor: Carey N. Pope

- Designed a novel biochemical assay and associated data analysis to assess enzyme activity degrading neurotoxins.

Representative Scientific Expertise

Physical:	Quantum Mechanics, Functional Materials, Semiconductors, Catalysts, Batteries, Nanoparticles
Biological:	Molecular Biology, Protein Dynamics, Bioinformatics, Metabolism, Drug Design, Assay Development
Computational:	AI/ML, High Performance Computing, Architecture, Python, Fortran, C, SQL, Java, Bash, LaTeX, Git

Education

Ph.D. in chemistry	Lehigh University	*Dissertation defense on April 16, 2024*
B.S. in biochemistry	Oklahoma State University	2019

Bar Admission

United States Patent and Trademark Office (pending) — *Passed registration exam on February 28, 2024*

Awards

Roy R. Hornor Fellowship	Lehigh University	2022 – 2023
Dean's Research Fellowship	Lehigh University	January – May 2023
University Fellowship	Lehigh University	2019 – 2020
Wentz Research Grant	Oklahoma State University	2018 – 2019
Dependency Scholarship	ConocoPhillips	2015 – 2016
Freshman Research Scholarship	Oklahoma State University	2015 – 2016

Outreach, Events, & Training

Materials Chemistry & Data Science Hackathon NSF January 2023

- Team-based high-throughput epitaxial matching.

Mentored 2 undergraduates	Lehigh University	2020 – 2023
– Supervised weekly update meetings.		
Big Data & Machine Learning Workshop	NSF XSEDE	February 2022
– Attended 3 days on Spark, Tensorflow.		
Quantum Chemistry Workshop Teaching Asst.	Lehigh University	June 2022 & June 2023
– Assisted in workshop and developing materials.		
Parallel Programming Boot Camp	NSF XSEDE	June 2021
– Attended 4 days on OpenMP, MPI, OpenACC.		
General Chemistry Lab Teaching Asst.	Lehigh University	August – December 2021
– Supervised approximately 40 Students.		
Graduate Student Senate Representative	Lehigh University	2021 – 2022

Publications

Knepp Z.J.; Repa G.M.; Fredin L.A. Literature review to be submitted to *Chemical Physics Reviews.*

Khayata D.; Repa G.M.; Fredin L.A. Adsorption and disproportionation of carbon monoxide on faceted-gold surfaces and edges. Submitted to *Surface Science.*

Repa G.M.; Knepp Z.J.; Fredin L.A. A-site doping to alter oxygen mobility in $SrTiO_3$. Submitted to *ACS Omega.*

9. Repa G.M.; Fredin L.A. Lessons learned from catalysis to qubits: general strategies to build accessible and accurate first-principles models of point defects. *Journal of Physical Chemistry C.* **2023**, 127(45), 21930–21939.
   – *Perspective Article.*

8. Kompanijec V.; Repa G.M.; Fredin L.A.; Swierk J. Controlling product selectivity in oxidative desulfurization using an electrodeposited iron oxide film. *Dalton Transactions* **2023**, 52(28), 9646–9654.

7. Repa G.M.; Fredin L.A. Predicting electronic structure of realistic amorphous surfaces. *Advanced Theory and Simulations* **2023**, 2300292.
   – *Illustrated front cover (2370024).*

6. Martin S.M.; Repa G.M.; Hamburger R.; Pointer C.; Ward K.; Pham T.N.; Martin M.; Rosenthal J.; Fredin L.A.; Young E. Elucidation of complex triplet excited state dynamics in Pd(II) biladiene tetrapyrroles. *Physical Chemistry Chemical Physics* **2023**, 25, 2179–2189.

5. Repa, G.M.; Fredin, L.A. Capturing experimental properties in computationally efficient faceted titania nanoparticle models. *International Journal of Quantum Chemistry* **2023**, 123(7), e27062.

4. Pugliese A.; Shyam B.; Repa G.M.; Nguyen A.H.; Mehta A.; Webb E.B.; Fredin L.A.; Strandwitz N.C. Atomic layer deposited aluminum oxide thin films probed with X-ray scattering and compared to molecular dynamics and density functional theory models. *ACS Omega* **2022**, 7(45), 41033–41043.

3. Repa, G.M.; Fredin, L.A. Mn environment in doped $SrTiO_3$ revealed by first-principles calculation of hyperfine splittings. *Applied Physics Letters* **2022**, 121(2), 022401.
   – *Featured as Editor's Pick.*

2. Repa, G.M.; Fredin, L.A. Parameter space exploration reveals interesting Mn-doped $SrTiO_3$ structures. *Physical Chemistry Chemical Physics* **2021**, 23, 23486–23500.
   – *Illustrated inside front cover (23394).*

1. Martin, S.M.; Oldacre, A.N.; Pointer, C.A.; Huang, T.; Repa, G.M.; Fredin, L.A.; Young, E.R. Proton-controlled non-exponential photoluminescence in a pyridylamidine-substituted Re(I) complex, *Dalton Transactions* **2021**. 50, 7265–7276.

Selected Posters & Presentations

4. Repa, G.M.; Fredin, L.A. Defect dynamics, aggregation, and characterization in disordered semiconductors. **2023**. *ACS Fall National Meeting.* San Francisco, CA.

3. Repa, G.M.; Yochum, R.; Fredin, L.A. Computational modeling of photodriven processes at oxide interfaces. **2023**. *Photochemistry Gordon Research Conference.* Bates College, Lewiston, ME.

2. Repa, G.M.; Fredin, L.A. Developing models for oxide materials. *ACS Mid-Atlantic Regional Meeting* **2022**, The College of New Jersey, Ewing, NJ.

1. Repa G.M.; Bhandari D.; Mashayekhi M.; Zhou D. Structure-based drug design for cancer. *Three-minute thesis competition* **2018**, Oklahoma State University, Stillwater, OK.
   – *2nd place of approx. 40 competitors.*